Theory of image formation in non-linear optical microscopy

Jarno Nicolaas van der Kolk

Thesis submitted to the
Faculty of Graduate and Postdoctoral Studies
In partial fulfillment of the requirements
For the Ph.D. degree in Physics

Ottawa-Carleton Institute of Physics
Department of Physics
Faculty of Science
University of Ottawa
Ottawa, Canada

Summary

Nonlinear optical microscopy is a collection of very powerful imaging techniques. Linear optical microscopes probe the refractive index and absorption, which both stem from the first-order linear electric susceptibility. Especially in biological tissue, the variation in the refractive index is often small and the tissue is, in many cases, transparant. Nonlinear optical microscopes on the other hand probe the nonlinear higher-order susceptibilities, which can be chemically sensitive, leading to the capability to achieve label-free imaging.

Nonlinear optical microscopes have been in development for more than thirty years and they are based on numerous nonlinear optical processes. The ones I will concentrate on in this thesis are second harmonic generation (SHG), coherent anti-Stokes Raman scattering (CARS), and stimulated Raman Scattering (SRS). The first technique is commonly used to image collagen as those molecules have a particularly large second-order nonlinear susceptibility due to their chiral structure. CARS and SRS on the other hand are often used because they resonantly target vibrational resonances in molecules, giving rise to the aforementioned label-free imaging.

Deep understanding of the nonlinear imaging process is crucial to the interpretation of the images these techniques produce. Computational tools are exceptionally suited for this task as they allow studying the electromagnetic field anywhere in the sample as well as the far-field, and one can change any of the material properties to study their effect. One such tool is finite-difference time-domain (FDTD) that our group developed for nonlinear optical microscopy simulations. It is a direct discretization of Maxwell's equation. While computationally costly, it does allow any arbitrary shaped sample to be simulated. The sample can have frequency dependent refractive indexes, and also nonlinear media with third-order nonlinearities such as Kerr media and Raman-active media, but also second-order nonlinearities for SHG. The code is designed in such a way that it can run on thousands of CPUs on a wide variety of compute cluster which allows our group to obtain nanoscale resolution.

Another computational tool I use is the free-space Green's function solution to the Helmholtz equation, which can be used to calculate the Hertz vector in the frequency domain, both in the near- and far-field, based on the induced nonlinear polarization. The electric field is then calculated from this Hertz vector. This technique is much faster

then FDTD and also allows for arbitrary shapes of the nonlinear electric susceptibility in the sample. However, it assumes a homogeneous refractive index throughout the entire spatial domain and requires complete knowledge of the input beam or beams that induce the nonlinear polarization.

In this thesis, I use these tools to study the image formation process of various nonlinear optical processes mentioned earlier. For example, I study the effect of an inhomogeneous refractive index on the images produced by these microscopes. In literature the index of refraction is almost always assumed to be homogeneous, because, as mentioned before, the inhomogeneity of the refractive index is often small. However, I show that these small differences in the index of refraction can have a significant effect on the measured far-field intensity signal. For example, in SRS and CARS images, the measured signal can increase by an order of magnitude depending on the index mismatch and structure of the sample. Additionally, significant shifts in perceived position occur. Even nonresonant nonlinear signals can be evoked purely through a mismatch in linear refractive index.

Computational modelling can also help reveal additional detail. As SHG is a coherent process, subwavelength information can be inferred through the phase information. Our experimental collaborators built an interferometric SHG (I-SHG) microscope for exactly that purpose. We used this to image collagen fibrils, which are all aligned in a parallel fashion. However, because collagen fibrils have a chiral molecular structure, they can point either "up" or "down". Using my Green's function simulations of the SHG imaging process of collagen fibrils, I was able to predict the standard deviation in the measured phase and link it to the orientation of collagen fibrils in the focal spot of the probing laser beam, even though the diameters are far below the minimum resolvable capabilities of the microscope. We found that the "upwards" fibrils make up 46 % to 53 % of the sample.

Even with a normal SHG microscope that does not measures phase, additional subresolution information is obtainable. With our collaborators we measured the ratio of the forward SHG intensity signal to that in the backward direction and with my simulations, we are able to link this to the fibril diameters in collagen tissue. Thus we inferred that the fibril diameter increases as a function of tissue depth.

Furthermore, a computational technique called ptychography is able to retrieve phase information without an interferometric reference beam. Additionally, it increases resolution to the theoretical limit, independent of the laser focal spot size, and corrects for

distortions in the input beam as well. I have developed this technique for use with nonlinear optical microscopy and was able to show it is a viable alternative to I-SHG by imaging simulated rat tail tendon at the diffraction limit while retrieving the orientation of the fibrils through the phase of the SHG signal. I also implemented the algorithm for CARS, where the phase information can be used to greatly increase the signal-to-noise ratio by reducing the nonresonant background radiation that results from competing nonlinear optical processes. I showed an example of this by imaging a simulated fibroblast cell where the CARS process was tuned to the lipid droplets inside of the cell. I am currently in talk with experimentalists to apply this theoretical technique to experiments as that would further demonstrate the impact of my work.

Finally, keeping in theme with the collagen fibrils, I show that the ratio of the forward SHG signal to the backward signal, the F/B ratio, is affected by a mismatch in the refractive index for fibrils larger than 100 nm. This measure is an indicator of fibril diameter and thus important for making qualitative predictions. Single fibrils are generally too small to be significantly affected by near-field effects, but the bigger fibrils can be. Fibrils in rat tail tendon have a distribution of fibrils diameters and the large fibrils occur infrequent. However, I found that the large fibrils are largely responsible for the forward as well as backward signal, thus refractive index mismatches still affect the F/B ratio significantly despite their infrequency. The F/B ratio for a collection of fibrils placed in a $n = 1.47$ medium was found to be $31.8 \pm 0.7\,\%$ higher than for those in a $n = 1.33$ medium. Our experimental colleagues have done preliminary measurements on mouse tail tendon where they found an increase of $40 \pm 20\,\%$, in line with the value of $28.1 \pm 0.6\,\%$ that I found for simulations with mouse tail tendon.

In conclusion, the theoretical tools I have used in my thesis have provided me with the ability to study nonlinear optical image formation processes with a level of detail that would be near-impossible to do experimentally. I have used this ability to show how refractive index mismatches, such as those found in biological tissue, can significantly distort the far-field intensity signals. I have shown this for SRS and CARS where the far-field intensity signal appeared an order-of-magnitude larger compared to the same sample without a refractive index mismatch with the background medium. Additionally, shifts in the perceived position of the object under investigation were observed and I showed the presence of a nonresonant background signal in AM-SRS. Likewise I showed that in the SHG imaging of collagen fibrils significant changes in the F/B ratio can occur. All of these effects have important implications as these types of images as biomedical

researches rely on the correct interpretation of nonlinear optical microscopy images for both research and diagnostics.

Apart from showing the effect of a refractive index mismatch, I have also shown that computation modelling can be used to infer subwavelength features in SHG imaging experiments of collagen fibril such as fibril orientation and fibril diameter. These methods have the potential to aid medical researchers as changes in the structure of collagen are often an early indicator of diseases such as osteoarthritis.

Finally, I showed that the ptychography algorithm I developed for nonlinear optical microscopy is able to retrieve phase information of the nonlinear electric susceptibility in SHG and CARS imaging while also enhancing the resolution and correcting for distortions in the input beams. I can also use much larger laser spot sizes than in conventional experiments without compromising the obtained resolution, thus fewer measurements are required. The technique is not limited to SHG and CARS either; it will work for other nonlinear optical processes as well. Experimental verification of nonlinear ptychography will be done soon. This technique has to potential to significantly improve current imaging techniques since access to the phase information allows one to observe additional information about the sample as we showed with the I-SHG microscope.

Statement of Originality

I hereby certify that the work of the present thesis, to the best of my knowledge, is original and my own.

The code used for FDTD simulations was mainly written by Konstantin Popov (a former postdoctoral fellow in our group). It has however been extended by me to include specific features. Also the programs and scripts needed for the post-processing and analysis have been created by me. Konstantin Popov also created the initial Green's function code that was used for simulation the image formation process of collagen fibrils using SHG imaging. I have since expanded that code to a fully vectorial model that regards the nonlinear electric susceptibility as a tensor, thus allowing any polarization of the input beam and rotation of the collagen fibrils.

For the work in ptychography, the code has been completely written by myself using only the FFTW3 library to perform the necessary Fourier transforms.

Finally, the program for the Mie solutions was written by Julien Roy and Charalambos Kioulos, where the latter worked under my supervision to extend it for use with second harmonic generation and far-field expansion using the Green's function. Charalambos Kioulos created these extensions under my supervision. I wrote the programs to test the validity of his programs and created a more efficient version.

List of Publications

Acknowledgements

Obtaining a Ph.D. is a significant undertaking that I would not have been able to do without the support of many others. First and foremost of course my supervisor Prof. Lora Ramunno who has been a pillar of support during the years by putting me on the right track for my research as well as allowing me to follow my own ideas. Similarly, our now-former Post-Doc, Konstantin Popov, was instrumental in getting me up to speed in the early years. He is the creator of the FDTD code I have used extensively during my Ph.D. and he also took the time to explain the intricate details of it. Coming from a Master's in Condensed Matter Physics, both he and Lora helped me get a hold of the new (for me) and interesting field of nonlinear optical microscopy.

In the same vein, I would like to thank our current Post-Docs, Scott Newman and Antonino Calà Lesina, who were always available to answer my questions about simulations and anything else. I particularly enjoyed bursting into their office and just hanging out for a bit. Other group members I often interacted with included Gabriel Dupras who has a real gift for delving into the FDTD code and finding and fixing bugs as well as expanding its functionality. Specifically the unit testing he implemented will probably save our group many headaches in the future. Also Charalambos Kioulos has been a great help in my research on SHG microscopy of collagen fibrils.

Outside our group, there are also many people that contributed to my progress towards a Ph.D., such as the group of Prof. François Légaré at the INRS in Montreal. In particular, the Post-Doc Stéphane Bancelin has been a pleasure to work together with and as led to my two co-authored papers. Finally Prof. Albert Stolow from the NRC in Ottawa has — especially in the beginning of my Ph.D. program — taught me a great deal about the experimental side of nonlinear optical microscopy and also planted the seed of ptychography in my mind.

Furthermore, I want to acknowledge the Compute Canada Consortium for allowing me access to the vast computational resources available across Canada, which allowed me to run a great deal of my rather large simulations on clusters belonging to SHARCNET, HPCVL, Calcul Quebec, and SciNet. At the latter, a particularly powerful cluster, SOSCIP's BlueGene/Q, was available. It is the fastest supercomputer available in Canada and as of November 2016 it ranked 196th world-wide.

Of course, I would also like to thank the thesis committee composed of Profs. Jeff Lundeen, Jacob Krich, Costel Flueraru, and Daniel Côté for taking the time to read my thesis and attend my oral defence.

Finally, I would like to thank my family in the Netherlands who were perhaps not always too happy that I moved all the way to Canada, but they have been very supportive of my endeavour. And last, but certainly not least, I would like to thank my wife, Emily Campling, for putting up with me working much of the time and also for the careful proofreading of my conference abstracts, funding applications, and published work.

Table of contents

List of Figures

1

Introduction

Light interacting with matter has been an area of investigation since the time of the ancient Greeks when Euclid mathematically investigated light in his work *Optics* around 600 BC. It already contained the observation that light changes direction when it passes from one medium to the next, which is the basis of how lenses work. However, it was not until the invention of microscopes in the 1600s when optics gave scientists the ability to study otherwise invisible biological processes. A few of the earliest discoveries were the depiction of cells by Robert Hooke in his book *Micrographia* [3]. The microscopes by Antony van Leewenhoeck allowed for a major leap in magnification and were capable of seeing microorganisms, or animalcules as he called them, in 1677 [4]. Since then, the need to image biological samples in greater detail has led to countless microscopic techniques to observe the smallest features possible, sometimes down to the atomic level.

Today, microscopes are in use in many fields of science, and biology remains one of its major users. Numerous techniques have been developed to improve the optical microscopes. Improvements in lens making allows for higher magnifications without aberrations, thus increasing the maximum obtainable resolution. The classical microscope is known as a bright-field microscope where white light is passed through a sample and the light is collected by an eye piece or camera behind it. This type of microscope

measures attenuation as different parts of the sample absorb different frequencies of light and also measures different indexes of refraction as light is bent. However this does not work well when the sample is transparent, as is often the case with biological samples. One solution is to sacrifice the sample and chemically treat it such that different tissues show different colours in a process called staining. However, this is obviously not always desired.

One technique for overcoming the need for staining is dark-field microscopy, which was pioneered by Joseph Jackson Lister in 1830, where the central portion of the beam is blocked such that light only reaches the sample at large angles [5]. The illumination from the beam itself therefore does not reach the objective, only the scattered light does. This greatly enhances contrast, and is a technique that is still in use today after close to two hundred years. In my opinion, dark-field microscopy would certainly have earned Lister a Nobel Prize if those had existed back then.

Another example of linear optical microscopes are phase-contrast microscopes for which Fritz Zernike was awarded the 1953 Nobel prize [6]. While dark-field microscopy improved contrast significantly, transparent samples were still hard to image. To overcome that, phase-contrast microscopes translate phase differences into amplitude differences by making use of destructive interference effects between light passing through the sample followed by a wave-plate, and light passing around it. If the phase of the light going through the sample and then the wave plate is delayed by in total half of a wavelength, it will interfere destructively with the light that is not delayed. Small deviations in the phase delay caused by the sample show up against a dark background. This significantly increases the contrast.

What this very brief history of microscopes shows is not only the quest for higher resolution, but also higher contrast. That is, the ability to tell materials apart. While dark-field and phase-contrast microscopes certainly have helped to image almost transparent biological tissues, sometimes materials are just too similar. Thus materials need staining to give them colours, which allows tissues to be analyzed through histology [7]. Ideally, one would like to be able to image just a specific molecular species of interest.

A major breakthrough in this area was fluorescence microscopy. By either using the natural fluorescent properties of the target molecule or by attaching fluorescent labels to the molecule of interest, one can track their movement through biological material. Resolutions lower than the diffraction limit can be reached by using stimulated emission depletion (STED) microscopy for which the Nobel Prize in Chemistry was awarded to

Eric Betzig, William Moerner and Stefan Hell in 2014. In STED, a specially crafted beam profile depletes the fluorescence surrounding the target, but not the target itself. Immediately after, the actual imaging beam is used and resolutions of 35 nm can be achieved [8]. This invention allows studying of living organisms in-vivo at ultrahigh resolution. Thus biological processes can be studied in real-time.

The requirement for labelling can in some cases disturb the very biological process one is trying to observe [9, 10]. On top of that, it is of course impossible to track molecules as they are being produced by the biological process because a fluorescent label needs to be attached unless the molecules autofluoresce. Also, the depleting beam in STED deposits a large amount of energy in the sample which may damage it. Thus improved label-free technologies were required, which is where nonlinear optical microscopes come in.

1.1 Nonlinear optical microscopy

With the introduction of nonlinear optical microscopes, it became possible to observe contrast where before there was none without the use of labels or staining. The origin of nonlinear optical effects can be understood from Maxwell's equations. When he introduced those now-famous equations, interaction between light and matter became much better understood. Several of the equations had been around before of course, but Maxwell's addition of the displacement current density to Ampere's Law took account of the way dielectric materials become polarized due to electromagnetic radiation and how that in turn affects the radiation of the material. For most illumination, the relation between the induced polarization and the incoming electromagnetic field is linear. However, as the light source becomes stronger, nonlinear effects start to occur, which makes it possible for the material to emit at a different frequency than the incoming light. This is why most nonlinear optical processes were demonstrated experimentally shortly after the invention of the laser in the sixties since the high coherent field-strengths required became available.

In a nonlinear optical microscope, the input laser beam is typically tightly focused to create a small focal volume inside of the sample. In this manner one obtains the high electric fields necessary for the nonlinear optical process to generate detectable levels of radiation. For this reason, the preferred setup for nonlinear optical microscopes is a scanning microscope where either the input beam or the sample is moved while a photomultiplier tube records the nonlinear signal intensity for each position of the laser focal

spot in the sample. After a scan has been completed, an image is created [11].

Having a tightly focused laser beam also brings another major benefit, which is the ability to do 3D imaging. The spot size of a tightly focused laser beam is not only small in the lateral direction, but also in the longitudinal direction. The nonlinear optical process thus only occurs in a small volume of space and the resulting far-field signal can be assigned to a 3D pixel (or voxel). Typically the laser focal spot has the shape of an ellipsoid that is stretched in the direction of the beam propagation, but by making use of a confocal beam setup, the longitudinal resolution can be increased further, making 3D imaging practical. This is done by the clever placement of an aperture just before the detector to block out any light not coming from the centre of the focal point [12].

One of the earliest examples of nonlinear optical processes is the demonstration of second harmonic generation (SHG) in 1961, showing frequency doubling experimentally [13, 14]. Two decades later, this effect was used to create one of the first nonlinear microscopes for imaging biological tissues [15]. Being able to measure higher-order nonlinear susceptibilities can provide additional insight in the samples being imaged. Freund et al. showed SHG can create contrast in samples where the index of refraction is practically homogeneous and transparent [15]. Linear microscopes are not able to show any contrast in such a case unless the tissues are stained by chemicals.

Since then, nonlinear optical microscopes have been developed using other nonlinear optical effects such as third harmonic generation (THG) [16], coherent anti-Stokes Raman scattering (CARS) [17], stimulated Raman scattering (SRS) [18], two-photon fluorescence [19] and others.

Depending on the circumstances and material, these techniques each have their advantages and disadvantages. A particularly spectacular example of nonlinear microscopes providing contrast occurs when using coherent anti-Stokes Raman scattering (CARS) and stimulated Raman scattering (SRS). These nonlinear optical processes are chemically sensitive which means that they can image specific molecular species without the need to attach labels or staining while ignoring any other molecules because instead of labels, these processes use the vibrational modes of the molecules of interest in the sample. This amazing property enables researchers to study biological processes by following the target molecules as they move through the tissue. Through experimental work, these microscopes have improved significantly to allow moderately high resolutions as well as video-rate imaging speeds and improved contrast over linear microscopes. CARS and SRS videos thus allows for the observing of biological processes as they happen. Simi-

larly, SHG microscopes have been an essential tool for imaging collagen in tissue since their inception. It can however also be used for imaging microtubules and muscle myosin which also have large second-order nonlinear susceptibilities [20]. Additionally, specific dyes can be used in combination with SHG to avoid photodamage as SHG is a parametric process and thus does not deposit energy into the sample [21].

These powerful tools have become important components of today's diagnostic and research tools in the biological science as they can create images that provide a wealth of information about the studied samples. Understanding the nonlinear optical image formation process in great detail is therefore of importance for correctly interpreting images. For example, since most nonlinear optical microscopes are scanning laser microscopes, does getting a high intensity from a certain laser focal point really mean that there is a higher density of target molecules there? Or does the measured position of an object truly coincide with the actual position? Questions such as these can be answered by using a theoretical approach as I show in this thesis. Going further, one might also ask: can this theoretical approach improve existing nonlinear optical microscopes? To that, I find the answer is: yes. Resolution can be improved, and even phase information from the nonlinear electric susceptibility can be retrieved using just intensity measurements.

To understand nonlinear microscopy, we have to understand the underlying mechanisms. Generally when a material is subjected to an electromagnetic field, a polarization will be induced. For example, the electronic response to an electromagnetic wave perturbs the electron clouds of the electrons around the atoms. The electrons will oscillate with the incoming electric field. In doing so, they will create their own electromagnetic field which in turn modifies the incoming electromagnetic wave. This mechanism is responsible for materials having a refractive index as the field of the displaced electrons affects the incoming electromagnetic wave. For most light in our everyday experience the electric field has a low amplitude, in which case the displacement of the electrons is linearly dependent on the strength of the incoming field, $\vec{E}$. That is, the polarization varies as

$$\vec{P} = \epsilon_0 \chi^{(1)} \vec{E}, \tag{1}$$

where $\chi^{(1)}$ is the linear electric susceptibility, which as the name implies signifies how susceptible the material is to electric fields, and ϵ_0 is the permittivity in vacuum. However, if the electric fields become particularly large, the electrons' response is no longer

linear. When this happens, the polarization can be written as a Taylor expansion as [14]

$$\vec{P} = \epsilon_0 \chi^{(1)} \vec{E} + \epsilon_0 \chi^{(2)} \vec{E}\vec{E} + \epsilon_0 \chi^{(3)} \vec{E}\vec{E}\vec{E} + \dots \quad , \tag{2}$$

where the $\chi^{(n)}$ is the n-th order electric susceptibility tensor of rank $n+1$.

Armstrong et al. derived this expression for the second-order and third-order term in 1962 based on their theoretical studies of the underlying quantum mechanics [22]. Having the above macroscopic equation greatly simplifies working with Maxwell's equations for modelling the nonlinear optical response.

The higher-order terms can have components that oscillate at frequencies that are the same as the input beam, *e.g.* the Kerr effect, but those frequencies can also different from the incoming electric field, which leads to radiation at a frequency other than the incoming beam. This includes higher frequencies, something that is impossible with linear microscopes. The incoming and outgoing frequencies follow strict rules that can be understood as nonlinear optical processes involving multiple photons. For example, second harmonic generation results in a signal that is oscillating at twice the incoming frequency, *i.e.* two photons combine to a single photon with double the input frequency.

Many nonlinear optical microscopy techniques exists, each with their strengths and weaknesses depending on the material and experimental environment. Examples include sum frequency generation, which is useful for surface spectroscopy in the infrared regime [23]; third harmonic generation, which can be used to image otherwise transparent objects [16]; and multi-photon absorption, which is useful for deep-tissue penetration with infrared beams while still measuring visible light [24]. In this thesis I will concentrate only on second harmonic generation (SHG), coherent anti-Stokes Raman scattering (CARS), and stimulated Raman scattering (SRS). Still, many of my findings likely hold for other modalities as well. Field enhancements due to scatterer size and shape will occur in other techniques for example, as will the nonlinear ptychography algorithm that I will present later.

1.2 Second Harmonic Generation

As mentioned before, one of the first nonlinear microscopes for imaging biological samples used SHG for imaging [15]. It is relatively straightforward nowadays to construct a SHG microscope [11] and they are uniquely suited for imaging specific types of tissues; not just collagen, but other noncentrosymmetric samples as well. Microscopes for SHG imaging can be used to diagnose diseases such as breast cancer [25] and skin cancer using in-vivo

biopsy on humans [26]. Histology diagnoses that rely on fibrosis scoring can be done more reliably with SHG and does not require staining [27]. For imaging cornea which for obvious reasons is normally transparent, it is also exceptionally suited as cornea has a chiral molecular structure [28–30].

Theoretical work on nonlinear optics started with SHG. The importance of taking into account the coherent nature of SHG was shown early on by Bersohn et al. in 1966 to explain experimental data where the measured signal of carbon tetrachloride was much lower than expected [31]. They did this by using quantum mechanics to calculate the scattering probabilities as a function of angle using the full second-order nonlinear susceptibility tensor for both the coherent and incoherent case. Another effect of the coherent nature they found was that the orientation of molecules plays a large role.

Freund et al. showed that the radiation pattern of a spatial distribution of molecules is affected by the coherent nature of SHG [15]. They did a theoretical study on collagen fibrils which were modelled as cylinders and found that in the forward direction the intensity scales as cylinder diameter to the fourth power as one would expect, but in the backward direction the internal interference between the scatterers in the cylinder could lead to complete destructive interference in the backward direction depending on the diameter of the cylinder.

Later work by Mertz et al. also showed that the spatial distribution of the scatterers drastically affects both the emitted signal intensity as well as the radiation pattern of the SHG radiation in the far-field [32]. By introducing sample inhomogeneities with specific spatial frequencies and illuminating with a tightly focused laser beam they calculate the far-field effects using a fully vectorial model of a distribution of scatterers. Schanne-Klein's group showed the importance of the effect that optical components such as excitation and collection numerical apertures and detection direction can have on polarization SHG imaging [33] and also the effect of anisotropic thick tissue [34]. Specifically for polarization-resolved SHG microscopy, Brasselet's group investigated ways of determining the precision of measurements by modelling the image formation process on cylindrical structures [35, 36].

Most of the applied examples of SHG in the first paragraph involves imaging collagen. Objects containing collagen fibrils are often imaged using SHG because they naturally have a large second-order nonlinear susceptibility. There are two main reasons for this. The first reason is that collagen molecules, due to their chirality, have no inversion symmetry [37]. Second, SHG is a coherent technique, which means that constructive and

destructive interference can occur depending on the phase matching conditions. From the theoretical work I discussed it is known that these conditions depend on the shape of the beam as well as on how the scatterers are distributed in the sample and these dictate the shape of the radiation pattern in the far-field. Collagen molecules tend to self-assemble in fibrils in a parallel fashion over tens of microns [37,38]. Since they are all aligned in the same direction, this leads to constructive interference in the forward direction which further boosts the nonlinear response of collagen fibrils. If the illuminating beam is a focused laser beam and the fibrils are larger than the Rayleigh length, then the effect of the Gouy phase shift will result in destructive interference. However, the fibrils have diameters of at most 400 nm which for most focused beams is much smaller then the Rayleigh length, thus this effect can be ignored for fibrils.

Collagen fibrils can be found in a wide array of biological tissues such as bones, tendons, arteries, cornea and many others. They form the basis for more complex hierarchies such as collagen fibres which in turn can comprise tendons and bone [37,38]. The fibrils are responsible for most of the mechanical properties, such as elasticity and compressibility [39]. Examples include making skin tear resistant [40] or initiating and orienting bone growth [41,42]. There is also evidence that the structural environment they create can affect the fate of stem cells [43]. Their many different functions and large presence in tissue alone makes collagen fibrils an important subject of research. Indeed, collagen fibril diameter in cornea is closely related to ageing in general [44].

As these fibrils are present in so many biological tissues and are clearly important for the functioning of said tissue, having tools available for studying them is important. These tools are available and have been developed over the past decades. Most of these improvements have been in the experimental field, but here too, the power of the theoretical approach allows me to go further. I will use the coherent properties of SHG to obtain information about collagen tissues on the nanoscale, which is below the maximum optical resolution of the SHG microscope. Using numerical modelling I can get not only information about the size, but also orientation of these fibrils. Numerical modelling also allows me to study the effect of refractive index mismatch between the fibrils and the medium surrounding them, which is something that is often ignored in experiments and theory and which I find has a large effect in certain types of tissues.

SHG is a nonresonant nonlinear optical process. The diagram of the process is shown in figure 1. Two photons from the pump beam excite the molecule to a virtual level from which it immediately decays, emitting a photon with double the frequency. Note that

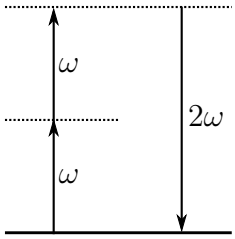

Figure 1: The second harmonic generation process. The solid lines are resonant vibrational modes and dotted lines are virtual levels. Two photons combine into one photon with double the frequency.

this is different from two-photon absorption (TPA) where the top level is not virtual; TPA is a resonant process. This shows that the label-free imaging does not come from tuning to a resonance, but from the molecular structure and constructive interference. In formula form the induced nonlinear polarization is described as

$$\vec{P}_{\text{SHG}}(2\omega) = \epsilon_0 \chi^{(2)}(2\omega = \omega + \omega)\vec{E}(\omega)\vec{E}(\omega), \tag{3}$$

where $\chi^{(2)}$ is the second-order nonlinear electric susceptibility, a tensor of rank three. The notation for the argument of $\chi^{(2)}$ is a symbolic notation that signifies that the strength of $\chi^{(2)}$ not only depends on the output frequency, but also on each of the input frequencies. Here, $2\omega = \omega + \omega$ indicates that two photons at frequency ω result in the emission of one photon at 2ω. The second-order nonlinear susceptibility is what is typically imaged in SHG images as it describes how the materials react to an incoming electric field. It is linearly related to the scatterer density, therefore the far-field electric intensity signal that is generated by the nonlinear process should scale quadratically. However, I show in this thesis that this is not always true due to the interference effects that take place, which is our first hint that images from nonlinear optical microscopes are not always what they seem.

In the beginning of this section, I claimed that collagen generates a high SHG signal because it does not have inversion symmetry. This is because an important property of even-order susceptibilities is that they are zero for centrosymmetric materials, that is materials that have inversion symmetry. This symmetry means that inverting the coordinates through the transformation $\vec{r} \to -\vec{r}$ leaves the molecular structure unchanged [14]. Inversion symmetry can be expressed in formula form as $\chi^{(2)}(-\vec{r}) = \chi^{(2)}(\vec{r})$. Since $\vec{P}$ and $\vec{E}$ are vectors, inverting the coordinates makes them point in the "opposite" direction. Thus we have $-P = \epsilon_0 \chi^{(2)}(-E)^2 = \epsilon_0 \chi^{(2)} E^2$. Direct comparison with equation (3) implies that $P = -P$, therefore $P = 0$ and thus also $\chi^{(2)}$. Only breaking of this

symmetry allows $\chi^{(2)}$ to be nonzero, and this does not need to occur at the crystal level, but also happens at interfaces as was already discovered theoretically in 1962 [45].

A large number of materials have this centrosymmetric property, which means they cannot be imaged using SHG. However, that also means that those centrosymmetric materials will not show up in SHG images, which allows for label-free imaging of non-centrosymmetric materials.

1.3 Vibrational spectroscopic imaging

Another important nonlinear optical imaging technique is vibrational spectroscopic imaging. The vibrational spectrum of a molecule is unique and can be used to identify it, much like how optical spectroscopy can identify the elements in a given sample. This vibrational spectrum is known as the Raman spectrum [46], for which Raman received the 1930 Nobel Prize in Physics [47]. Fundamentally, it is a way to map the chemical bonds of the molecules. The resonant vibrational frequency for a given chemical bond depends not only on the type of vibration, such as rotational or longitudinal, but also on the elements on either side of the bond. As these vibrations involve the movement of atomic nuclei, they are much slower than the electronic modes associated with optical frequencies. Rather these vibrational modes mostly occur in the infrared regime. For biological tissues the range of frequencies is known as the fingerprint region, which ranges roughly from $500\,\mathrm{cm}^{-1}$ to $3500\,\mathrm{cm}^{-1}$ [48]. The Raman spectrum is typically recorded by recording the emission of Stokes or anti-Stokes photons, which are photons that have a slightly lower or higher energy than the incoming photon. This small energy shift is due the beating of the optical frequency with the motion of the atom nucleus *i.e.* the vibrational modes. Unfortunately, Raman spectroscopy is an inefficient process, where typically only 10^{-8} of the incident intensity is converted into a Raman signal. It is therefore a slow process and requires either a large incoming electric field strength, which can damage the sample, or a long exposure time, which excludes imaging fast processes. The advent of the laser in the sixties enabled the high electric field strength, at which point Raman spectroscopy drastically rose in popularity for samples able to withstand those field strengths. Only at these very high field strength do acquisition times reach the microseconds domain [47].

To increase the efficiency of Raman spectroscopy, a new technique called Coherent Anti-Stokes Raman Scattering (CARS) was introduced, which is a third-order nonlinear process that is sensitive to the vibrational states of molecules. It was first shown exper-

imentally also in the sixties [49], but due to the difficult experimental set-up where the two laser beams needed to be crossed, it did not gain steam until the eighties when a simplified set-up was introduced using colinear laser beams [50]. Since then CARS has been used extensively and it allows for video-rate scanning [51]. Then in 2007, the first microscopes based on stimulated Raman scattering (SRS) were developed [52] and is thus still a relatively new technique, even though the SRS effect was already known in the sixties [53]. Like CARS, SRS allows for label-free imaging by tuning the two lasers such that their difference corresponds to a peak in the vibrational spectrum of the molecule of interest. This can be done with video-rate imaging to track biological processes in real-time [54, 55].

CARS is a technique that is used for both medical research as as well as for diagnostics. For example, CARS has been used in testing Hepatitis C medication [56]. Other noteworthy examples are the imaging of nerve cells in vivo [57], or the studying of myelin degradation by following the calcium [58], or as a diagnostic tool for brain tumors and lesions [59], or arterial cells [60], or to examine emulsions for applications in the food industry [61]. SRS on the other hand has been useful for biomedical applications such as tracking drugs as they move through tissue [62, 63], detecting tumours [64], and the tracking of newly synthesized proteins as they are being produced [65].

Theoretical work on CARS by Cheng et al. shows that the spatial distribution of the scatterers due to the coherent nonlinear optical process determines the far-field radiation pattern [66]. The spatial distributions they considered are objects such as cylinders and disks of various sizes in the order of wavelengths. Using a vectorial Green's function approach they calculate the far-field CARS signal from the objects illuminated by a Gaussian beam. Similar to SHG, this shows once again how important the coherent nature of the nonlinear optical process is.

A thorough overview of both SRS and CARS can be found in the chapter by Potma and Mukamel in [17] where both techniques are treated both classically as well as quantum-mechanically. They show how Raman scattering originates from the vibrations of the chemical bonds in molecules and how one can drive the Raman mode to increase its efficiency through stimulated emission. Additionally, they show how this is encapsulated by the frequency-dependent third-order nonlinear susceptibility, which is what one measures when using SRS or CARS microscopes. In *Nonlinear Optics* by Boyd [14], the SRS process is derived both from an atomic level considerations as well as classically motivated in the way of interpreting electron-nucleus interaction as a simple

string which provides an intuitive picture. More in-depth descriptions of the quantum mechanics underpinning both SRS and CARS can be found in the work of Penzkofer et al. [67]. For SRS, the quantum mechanical description of a three-level atom model can be employed to describe how the Stokes gain signal increases as a function of both time and space [68].

To be able to correctly interpret images made by SRS and CARS microscopes, the image formation process must be clearly understood. Earlier it was shown by our group that the Gouy phase shift can affect the measured position of polystyrene beads with sizes comparable to the wavelength of the input beams when using CARS microscopes [69]. The Gouy phase shift imparts a phase on the Raman-active object depending on its position relative to the laser focal point. Because there is a phase difference between the resonant CARS signal and the nonresonant background medium, destructive and constructive interference can occur that depends on the position of the object. The interference becomes more significant the smaller the beads are. This changes the far-field signal in such a way that the perceived position no longer coincides with the actual position of the object, which has been experimentally confirmed. It has also been shown recently by us that an inhomogeneous nonresonant background medium can affect the CARS and SRS far-field intensity signal [70]. This nonresonant background radiation occurs in CARS because of competing nonlinear optical processes that emit at the same anti-Stokes frequency as the resonant CARS process. SRS does not suffer from competing nonlinear optical processes because it measures at one of the input beams directly. However, even though one of the main advantages of SRS is that there is supposedly no background as there is with CARS, Popov et al. showed that this is not necessarily the case for amplitude-modulated SRS.

All of the experimental and theoretical work above ignore any effects of an inhomogeneous refractive index. This seems like a valid assumption because the samples are all biological tissues and thus the inhomogeneity of the refractive index is typically small, hence the need for nonlinear optical microscopes to obtain contrast in the first place. Because of this, there have been few attempts to investigate the effects of refractive index mismatches [71–73]. However, as the size of the objects in samples becomes comparable to the wavelength of the input beams, these small effects can start to play a big role. They can cause artifacts in the recorded images which are used by medical researchers but also as diagnostic tools. Detailed investigation of the image formation process under these circumstances is thus of significant importance, which is what I investigate in this

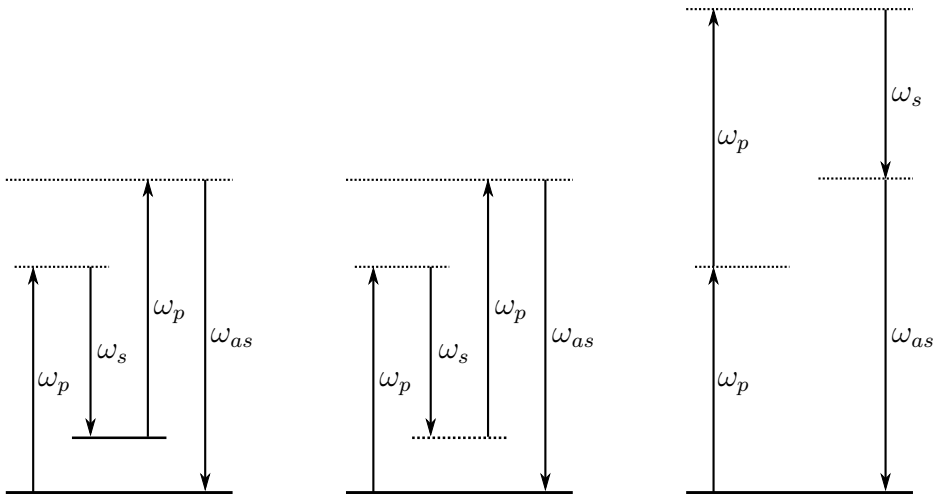

Figure 2: All of the anti-Stokes processes that contribute to the signal. The solid lines are resonant vibrational modes and dotted lines are virtual levels. Only the first process depends on the resonance. The other two form the nonresonant background.

thesis.

Both SRS and CARS require two input beams called the pump beam and the Stokes beam. The left diagram in figure 2 shows the CARS process where two pump photons and one Stokes photon result in the production of an anti-Stokes photon [17, 74]. For SRS the diagram is shown in figure 3. Here a pump photon is absorbed, and a Stokes photon is emitted through simulated emission. Thus the pump beam loses intensity while the Stokes beam gains. Unlike a CARS microscope where the signal at the anti-Stokes frequency is measured, a SRS microscope works by measuring either the loss of the pump or the gain of the Stokes beam [17]. In both diagrams the solid line shows a vibrational energy level for a molecule. By adjusting the difference in the frequency of the pump and Stokes beam to match the energy level of the vibrational mode, it is possible to become resonant with of a molecule of interest. This feature makes it possible to use CARS and SRS microscopy to image only those molecules and ignore the rest.

One effect that distorts the recorded image in CARS microscopy the existence of competing processes which also generate signal at the anti-Stokes frequency. These nonresonant processes are depicted in the right two diagrams in figure 2 and lead to a nonresonant background signal. Due to the fact that the nonresonant process is far off-resonance, its susceptibility is weak compared to the CARS on-resonance susceptibility. However, it will take place throughout the entire sample, whereas CARS is limited to only specific molecular species. For very small Raman-active objects, this allows the

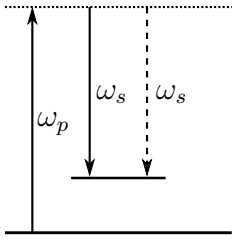

Figure 3: The stimulated Raman scattering process. The solid lines are resonant vibrational modes and dotted lines are virtual levels. The dashed arrow stands for stimulated emission.

nonresonant background to be of the same order or even drown out the CARS signal, resulting in a low signal-to-noise ratio. This is not a factor in SRS. In fact, one of the main advantages is the absence of a nonresonant background because there are no competing nonlinear optical processes. However, the loss or gain in the pump and Stokes beam is generally so small that one needs to employ amplitude or frequency modulation of the Stokes or pump beam respectively, making the experimental set-up more complicated than that of CARS.

It should be noted that the CARS spectrum is not the same as the Raman spectrum because the nonresonant background tends to distort it and Raman lines interfere. Typically the way to get around this is by using a retrieval algorithm, such as a Kramer–Kronig transformation which is able to retrieve the imaginary part when the CARS spectrum is known at every frequency [75]. Of course, the CARS spectrum is only known at a limited range of frequencies, so the true Raman spectrum is never fully retrieved and can in fact become distorted [76, 77]. SRS on the other hand records the true Raman spectrum [78, 79].

For further insight in the image formation process for CARS, we need to look at the induced polarization at the anti-Stokes frequency, which can be written as

$$P_{\mathrm{NL}}(\omega_{\mathrm{aS}}) = 3\epsilon_0\chi^{(3)}(\omega_{\mathrm{aS}} = 2\omega_p - \omega_S)E(\omega_p)^2E(\omega_s)^\star. \tag{4}$$

The factor three comes from the possible permutations of the frequencies ($\omega_p + \omega_p - \omega_s$, $\omega_p - \omega_s + \omega_p$, and $-\omega_s + \omega_p + \omega_p$). The nonlinear susceptibility can be split in a resonant and nonresonant part as $\chi^{(3)} = \chi^{(3)}_{\mathrm{R}} + \chi^{(3)}_{\mathrm{NR}}$. Various schemes have been developed to overcome the contribution from the nonresonant background. Methods such as interferometric CARS are able to retrieve the real and imaginary part through heterodyne detection and can then use the fact that $\chi^{(3)}_{\mathrm{R}}$ is fully imaginary, while $\chi^{(3)}_{\mathrm{NR}}$ is real [80]. Epi-CARS is another variation of CARS that looks at the back-scattered signal, which reduces the

nonresonant background because of the simple fact that the nonresonant background is always directed in the forward direction and the resonant signal much less so [81, 82]. Another popular method is FM-CARS, which takes advantage of the fact that $\chi^{(3)}_{\mathrm{R}}$, being on-resonance, is very sensitive to changes in the wavelength of the input beams, whereas $\chi^{(3)}_{\mathrm{NR}}$ is insensitive due to being very far from resonance. Applying frequency modulation to one of the input beams, creates an amplitude oscillation in the CARS signal, which allows the retrieval of purely the CARS signal by using a lock-in amplifier [83]. Then there is P-CARS which utilizes the polarization to suppress the nonresonant background by modulating the polarization of the input beams [84]. As the nonresonant background is independent of the input polarization, it is subtracted. Finally, broadband CARS measures a large part of the spectrum, which can then used to do a Kramers–Kronig transformation to retrieve the phase of the signal [75]. With the phase known, the nonresonant background can again be suppressed in the same way as with heterodyne detection.

Another CARS technique that has only recently been developed is hyperspectral CARS with which it is possible to obtain the spectrum per pixel by scanning over the frequency as well as the position [77]. This allows for a detailed image to be obtained for a sample that also contains the CARS spectrum. This provides insight in seeing which chemical is concentrated where.

For SRS, the induced nonlinear polarization is also a third-order nonlinear process that has almost the same form as for CARS. The difference is that the output frequency is either ω_p or ω_s depending on if one is looking for pump loss or Stokes gain. In formula form, the induced nonlinear polarization is

$$P_{\mathrm{NL}}(\omega_p) = \epsilon_0 \chi^{(3)}_R(\omega_p = \omega_p + \omega_s - \omega_s) E(\omega_p)|E(\omega_s)|^2 \tag{5}$$

$$P_{\mathrm{NL}}(\omega_s) = \epsilon_0 \chi^{(3)}_R(\omega_s = \omega_p - \omega_p + \omega_s)|E(\omega_p)|^2 E(\omega_s). \tag{6}$$

Thus for both CARS and SRS, the induced polarization depends on the input beams to the third power. This property of third-order processes makes them especially sensitive to field enhancements to which I will come back later.

One thing that becomes clear from these equations for CARS and SRS is that the SRS signal varies linearly with density while for CARS it scales quadratically for large densities, but linearly for low densities making it hard to quantitatively measure scatter densities with CARS. To see why, note that the induced polarization for CARS depends on $\chi^{(3)} = \chi^{(3)}_{\mathrm{R}} + \chi^{(3)}_{\mathrm{NR}}$. Since the far-field electric fields scale linearly with the constant

nonlinear susceptibility in the induced nonlinear polarization, the intensity will scale as

$$I_{\mathrm{CARS}} \propto |\chi_{\mathrm{R}}^{(3)} + \chi_{\mathrm{NR}}^{(3)}|^2 \tag{7}$$

$$= |\chi_{\mathrm{R}}^{(3)}|^2 + 2\,\mathrm{Re}\left[\chi_{\mathrm{R}}^{(3)}\chi_{\mathrm{NR}}^{(3)}\right] + |\chi_{\mathrm{NR}}^{(3)}|^2. \tag{8}$$

Thus the intensity will scale quadratically with $\chi_{\mathrm{R}}^{(3)}$ if $\chi_{\mathrm{R}}^{(3)} \gg \chi_{\mathrm{NR}}^{(3)}$, linearly with $\chi_{\mathrm{R}}^{(3)}$ if $\chi_{\mathrm{R}}^{(3)} \ll \chi_{\mathrm{NR}}^{(3)}$, and somewhere in between if $\chi_{\mathrm{R}}^{(3)} \approx \chi_{\mathrm{NR}}^{(3)}$. SRS on the other hand always scales linearly with $\chi_{\mathrm{R}}^{(3)}$ because one is measuring a gain or loss of the input beam such that in the far-field the intensity will scale as

$$I_{\mathrm{SRS}} \propto |E_p - \chi_{\mathrm{R}}^{(3)} E_p |E_s|^2|^2 \tag{9}$$

$$\approx |E_p|^2 \left(1 - 2\,\mathrm{Re}\left[\chi_{\mathrm{R}}^{(3)}|E_s|^2\right]\right), \tag{10}$$

where the approximation can be made because the pump loss is always much smaller than the input beam. Applying amplitude or frequency modulation results in the constant 1 dropping out, leaving just the linear dependence on the third-order nonlinear susceptibility.

I will use both the SRS and CARS technique to study the effect of refractive index mismatch on the far-field intensity signal. I am able to show that even though SRS is supposed to be background-free, a refractive index mismatch can still distort the signal.

1.4 My theoretical investigations

There have been great strides in the experimental part of nonlinear optical imaging. Over the past decades imaging modalities for many nonlinear optical processes have been developed, such as SRS, CARS, and SHG as I mentioned in detail above, but also processes such as difference frequency generation, sum frequency generation, third harmonic generation, two-photon absorption, three-photon absorption, and others. These techniques have been improved to provide better resolution, contrast, and imaging speed. However on the theoretical side, while there have also been strides, there is much to be done.

In this thesis, I aim to understand the image formation process using a theoretical approach and develop techniques to overcome limitations using that knowledge. While experimental work ultimately shows whether a certain concept is possible or not, theoretical work allows me to study the nonlinear optical image formation process at a much deeper level than experimental studies. As such, I am able to study the near-fields in and around the sample without affecting the measurement. I am able to vary parameters

such as the refractive index, nonlinear susceptibility, sample size, spatial configuration, and laser beam properties independently. Those changes would be hard to accomplish experimentally. For example, changing the refractive index experimentally would require changing the material, which in turn will affect other properties. It therefore becomes hard to assign changes in the far-field signal intensity to any one thing. Additionally, theoretical work gives access to the near-field as well as far-field. The image formation process can be studied at arbitrarily small length scales, which is far below the diffraction limit of any physical microscope. The theoretical scale is only limited by the amount of computational power available.

I will use a combination of computational tools to study the nonlinear optical image formation process in detail. The three main tools I use are finite-difference time-domain (FDTD) simulation, free-space Green's function calculations, and Mie theory for cylinders. These tools are described in detail in chapter 2.

FDTD is a direct discretization of Maxwell's equation [85]. The basis of this technique is the Yee cell where each of the six components of the electromagnetic field is discretized such that the derivatives in Maxwell's equations are approximated by second-order central difference derivatives [86]. This allows one to accurately simulate the interaction between light and matter. Additionally, one needs to have absorbing boundary conditions to be able to simulate infinite space, which were not developed until the eighties when Mur's absorbing boundary conditions were introduced [87]. Since then FDTD has become a very powerful tool for simulating electromagnetic processes that can largely be contributed to Taflove who facilitated FDTD to become the technique of choice for simulating electromagnetic radiation of arbitrary shapes. Indeed his book still forms the basis for many of the FDTD codes available today, either commercial or free [85, 88].

As computers get more powerful, larger FDTD simulations can be undertaken. Interactions between electromagnetic radiation and biological tissues such as the human eye were already simulated in 1975 and indeed the entire human body has been subjected to simulated electromagnetic radiation at radio frequencies ranging from 100 MHz to 350 MHz. Coincidentally, simulating the interaction of electromagnetic radiation in the human eye was one of the main reasons that Taflove started investigating FDTD [85]. Already in the nineties entire fighter aircraft could be modelled to study their interaction with radar with 3 cm resolution and 30,000 grid cells in total.

For my field of nonlinear optics, an additional component is needed, which is the nonlinear interaction [89]. This component along with the Yee cell and the absorbing

boundary conditions are detailed in section 2.1 and they form an amazing tool to simulate nonlinear optical processes. I have used it extensively throughout my Ph.D., where especially access to the powerful computers on SHARCNET, SOSCIP's BlueGene/Q, and our own group's cluster computer allowed me to run many high-resolution FDTD simulations. Such heavy computational resources are required because the FDTD algorithm is computationally very expensive.

In chapter 4, I use FDTD simulations to study the image formation process in SRS and CARS, because while nonlinear optical microscopes have advanced the understanding of biological processes significantly, for nonlinear imaging techniques to produce reliable images it is crucial to understand any effect that might cause distortions. In nonlinear optical microscopy, the effect of an inhomogeneous index of refraction is almost always ignored because, as mentioned before, the difference in refractive index is usually small in biological samples. However, referring back to equation (4), the nonlinear polarization for CARS depends on the input beams to the third power. The same holds true for SRS. I show that even small mismatches in the refractive index can create enhancements that can be an order of magnitude larger than expected in SRS and CARS images, as well as shifts in the perceived position of objects [90]. This has implications for the interpretation of SRS and CARS images for biomedical research and diagnostics as there is currently no known method to reduce these effects.

Apart from investigating distortions of the image formation process, theoretical work but can also lead to enhanced interpretation of experimental data, which in some cases can reveal information about the structure of a sample far below the physical maximum resolution of the microscope by carefully modelling *a priori* knowledge about the sample. In particular, I use the free-space Green's function formalism, which calculates the far-field signals of nonlinear optical processes occurring in arbitrarily shaped samples. The caveat is that it only works when the refractive index is homogeneous through the entire domain. The method is described in section 2.2. I use this tool to model imaging of collagen fibrils using a SHG microscope. Most biological tissues contain these fibrils and thus are an important area of research. In fact, the earliest biological studies using nonlinear optical microscopy studied exactly these fibrils because collagen generates such a strong SHG signal [15].

In collaboration with the experimental group of François Légaré we have been able to study the diameters of the fibrils in tissue through computational modelling even though the fibrils were much smaller than the optical resolution of the microscope [1].

My contribution was the theoretical model using a free-space Green's function approach to predict the relation between the fibril diameter and the ratio of the forward SHG intensity signal to the backward, the F/B ratio. Likewise, theoretical modelling can provide information about the internal orientation of the fibrils by using the coherent nature of SHG [2]. Légaré's group developed an interferometric SHG microscope with which they measured the phase of the SHG signal and they showed conclusively that dark areas in the SHG images were due to destructive interference and not due to the lack of collagen. My simulations confirmed that the measured phase can be directly linked to the overall orientation of the fibrils. My contributions as well as summaries of both papers are detailed in chapter 3. Additionally, I detail a possible future collaboration to investigate the forward and backward signals of cornea tissue and explain the speckle pattern that, depending on the tissue, is observed in the backward direction but not in the forward.

The interferometric SHG microscope we used was able to retrieve the phase information of the second-order nonlinear susceptibility of the collagen fibrils, which proved to be crucial in providing extra information about the sample. However, interferometry makes the optical set-up more complex as a reference beam is required at the nonlinear optical frequency and multiple measurements need to be taken at the same spot to retrieve the phase from the interference pattern. An alternative is to use ptychography, which is an iterative computational technique that I develop for nonlinear optical imaging and is described in chapter 5. It is able to reconstruct the complex-valued nonlinear susceptibility as well as correct for distortions in the input beams through multiple measurements at random locations on the sample while collecting the far-field signal with a CCD camera. It is based on linear ptychography that uses a similar algorithm for reconstructing the complex-valued transmission function of a sample [91, 92]. The nonlinear ptychography algorithm not only retrieves the phase information of the nonlinear susceptibility, it also increases the resolution of the image regardless of the spot size and corrects for distortions in the input beams. As examples, I show that it is possible to image simulated rat tail tendon with a resolution near the diffraction limit using SHG as well as remove the nonresonant background from CARS images. However, nonlinear ptychography can also be used for other nonlinear optical techniques where the phase of the nonlinear susceptibility is of interest. Experimental verification is forthcoming as I am currently planning the experiment with an experimental collaborator. The potential of nonlinear ptychography is substantial as it can retrieve phase information, increase resolution, and

correct for distortions in the input beams, while at the same time the technique uses a relatively uncomplicated experimental setup.

Phase plays an important role in the image formation process and it is clear that it can provide additional insights at subresolution scales. I have also talked about the importance of the refractive index in SRS and CARS microscopy and these two ideas can be combined to investigate the effect of a refractive index on imaging collagen fibrils with a SHG microscope, which is discussed in chapter 6. I concentrate on the F/B ratio where particularly for the signal in the backwards direction the phase matching is very important. Measuring the F/B ratio is useful in the biomedical sciences because changes in the F/B ratio can indicate structural changes of the sample. Also, as mentioned before, the F/B ratio is related to the diameter of the fibrils. In experiments, the F/B ratio is determined by averaging over many measurements of the SHG signal in the forward and backward direction to get an accurate ratio. However, few have investigated the effect of a small refractive index mismatch.

To investigate this, I employ yet another computational tool, which is known as cylindrical Mie theory. It is a derivation of the full electric field from Maxwell's equation that is exact with the caveat that the input beam is restricted to an incident plane wave input beam and the spatial geometry is an infinitely long cylinder of arbitrary radius. It takes into account a refractive index mismatch on the input beam. The restriction stems from the fact that Mie theory is an analytical derivation where Maxwell's equations are solved for a particular geometry. This method is discussed in detail in section 2.3, but in short, it allows me to retrieve the electric field of the input beam everywhere inside and outside the cylinder. These fields can then be used with the free-space Green's function to propagate the induced SHG signal to the far-field.

I find that for a single $n = 1.4$ fibril embedded in a medium with a refractive index of either $n = 1.33$ or $n = 1.47$, the field enhancements inside of the cylinders are only in the order of 4–5 %. However, the F/B ratio is significantly different from that of the same fibril in an index-matched $n = 1.4$ medium, but only for fibrils with a radius larger than 100 nm. The reason for the large sensitivity of the F/B ratio on small field enhancements is because SHG is a coherent process, that is, the phase-matching conditions lead to interference. In the forward direction, the far-field electric fields of scatterers inside the cylinder add up constructively in the far-field. However, in the backward direction there is no phase-matching, thus the far-field electric fields interfere with each other. So even though the field enhancements inside of the cylinder are small, they have a large effect on

the phase-matching condition and thus alter the SHG far-field intensity signal. Thus the F/B ratio is affected significantly. As the Mie/Green's function approach only takes into account the refractive index mismatch at the input beam frequency, I also use FDTD simulations to additionally examine the scattering of SHG radiation and find that this increases the distorting effect.

Fibrils in tissues such as rat tail tendon follow a distribution of diameters and hundreds of those fibrils will be inside of the laser focal spot. Fibrils with a radius larger than 100 nm do not occur often, however those larger fibrils generate the largest signal and thus their signal dominates. For rat tail tendon, I calculate the F/B ratio from 100,000 samples and compare the case of fibrils embedded in a $n = 1.47$ medium to those embedded in a $n = 1.33$ medium and find an increase in the F/B ratio of $31.8 \pm 0.7\,\%$. Stéphane Bancelin from François Légaré's group was able to produce preliminary experimental measurements on mouse tail tendon in water ($n = 1.33$) and glycerol ($n = 1.47$) and found an increase of $40 \pm 20\,\%$. My simulations for mouse tail tendon show an increase of $28.1 \pm 0.6\,\%$ which suggests the theory I developed is valid.

These results have consequences for experimental work that relies on the F/B ratio to make quantitative statements about the sample. I show that the quality of the measurement depends on the radii distribution of fibrils in the sample and as well as on the range of the refractive index. To my knowledge, this has not been investigated before.

In conclusion, by using computational tools effectively, a deeper insight can be gained about many nonlinear optical processes. I show that this leads to better understanding of SRS and CARS microscopy by highlighting the possible distortions that can occur due to refractive index mismatches between the objects and the surrounding medium as well as under which conditions those distortions occur. Similarly, refractive index mismatches can change the F/B ratio obtained from the SHG measurements of collagen fibrils. Here too, knowing the conditions under which these changes can occur aid interpretation of experimental data. Theoretical work can also improve the nonlinear image formation process: subresolution features can be extracted through careful modelling of the SHG imaging of collagen fibrils, and by developing ptychography for nonlinear optical microscopy, images can be significantly enhanced in resolution as well as augmented by obtaining phase information of the nonlinear susceptibilities. In short, I show that theoretical models and computational modelling can augment experimental work by investigating the image formation process to explain when and why distortions occur. Models can also enhance current imaging techniques to observe subresolution features or

retrieve phase information and enhance resolution.

2

Computational Methods

The tools that have been used for the research described in this thesis are largely computational in nature. Thanks to the fast computational resources that are accessible to me, I can peer into the deepest regions of samples as they are illuminated by electromagnetic radiation. I can study the interaction of matter and light at a level of detail that is not possible to do experimentally. Oftentimes I can simply turn on and off individual optical processes to study their contribution to the signal one would measure in experiments.

The power of computers has been increasing exponentially since the inception of computers based on integrated circuits. This is captured by what is known as Moore's Law, even though it is not as much as law as it is a prediction. It was first noted by Moore in 1965 and predicted that the number of transistors on a chip would double every year [93]. This exponential growth of transistor count has kept true until just a few years ago. Until a decade ago, this meant increases of the clock speed of the CPUs, but now the speedups are obtained by increasing the number of CPU cores on a chip, allowing for multithreaded programs. Computers are now able to do millions of calculations in a manner of seconds, which allows me to run the complicated simulations necessary for this thesis.

Thanks to the efforts of Compute Canada, which graciously hosts a national consor-

tium of powerful and accessible cluster computers such as those belonging to SHARCNET, Calcul Quebec, and SOSCIP, I have access to the thousands of CPUs I require. Some of the largest simulations I run are through SOSCIP on BlueGene/Q which is currently the fastest supercomputer in Canada. On top of that, our research group has its own cluster computer which has 70 nodes, each containing 8 hyperthreaded cores, to run my simulations.

For this thesis I have made use of three different types of simulations. The most resource-intensive is the finite-difference time-domain method (FDTD), which is able to simulate Maxwell's equation exactly except for discretization effects due to the need to divide space in a grid. It is discussed in section 2.1. The next type is a free-space Green's function approach which is discussed in section 2.2. It is numerically much cheaper than FDTD, but is assumes a homogeneous refractive index throughout space. Finally, in section 2.3 I talk about cylindrical Mie theory which is able to quickly calculate near-fields in and around cylindrical objects with a refractive index different from the background medium. These Mie calculations can be combined with the Green's function approach to at least incorporate an inhomogeneous refractive index for the input beams, but not for the nonlinear radiation.

One method that is not strictly a simulation, but worthwhile to mention is the method I used to numerically generate samples for the SHG imaging simulations in chapters 3 and 6. The samples represent collagen fibrils, which I model as randomly placed non-overlapping cylinders, and is discussed in section 2.4.

2.1 Finite-Difference Time-Domain

FDTD is a well-established tool for modelling the propagation and scattering of electromagnetic waves. The term was coined in the 1980s [94], but the first paper detailing the basics discretization of time and space stems from 1966 [86]. It is a direct solver of Maxwell's equations and has no approximations other than those resulting from using a discrete grid. For scattering problems, one needs a simulation domain that does not produce reflection at the boundaries, in essence, simulating light propagation to infinity. As simulating infinite space is impossible, one needs to be able to at least approximate it. For this absorbing boundary conditions are required starting with Mur's boundary conditions in 1981 [87] to the more commonly used perfectly matched layers (PML) that are used nowadays [95]. Then one needs the introduction of light sources into the simulation. By implementing the materials and their interactions with the electromagnetic fields, most electrodynamical processes can be simulated. In the case here, that would be the nonlinear optical interactions and the implementation of the nonlinear susceptibilities, $\chi^{(2)}$ and $\chi^{(3)}$, and of course the linear susceptibility $\chi^{(1)}$.

The number of papers using FDTD well exceeds a thousand per year and is still increasing. Several commercial software packages exist that use FDTD to simulate a wide range of materials in arbitrary spatial configurations. For example, the packages created by Lumerical, Optiwave, and OmniSim.

Our group has an in-house version of FDTD which was largely written by Konstantin Popov. We have our own version so that we can control every aspect of the simulations. This means we can implement any light source, such as tightly focused laser beams, and nonlinear media or even plasma. The coordinate system used in the code is such that the beams typically propagate in the x-direction and are polarized in the y-direction. Input beams can be plane waves, Gaussian beams or tightly focused beams. A near-to-far-field transform at the boundaries allows for collection of light in the far-field without needing to extend the simulation domain. It is capable of running on distributed compute platforms using many CPUs simultaneously which it is able to do thanks to the message passing interface (MPI). This allows all CPUs to only calculate their subdomain and communicate the boundaries of the subdomain easily to the other CPUs, even when those CPUs are in different computers. Since I made extensive use of our FDTD code during the course of my Ph.D., I feel I should shed some light on its inner workings.

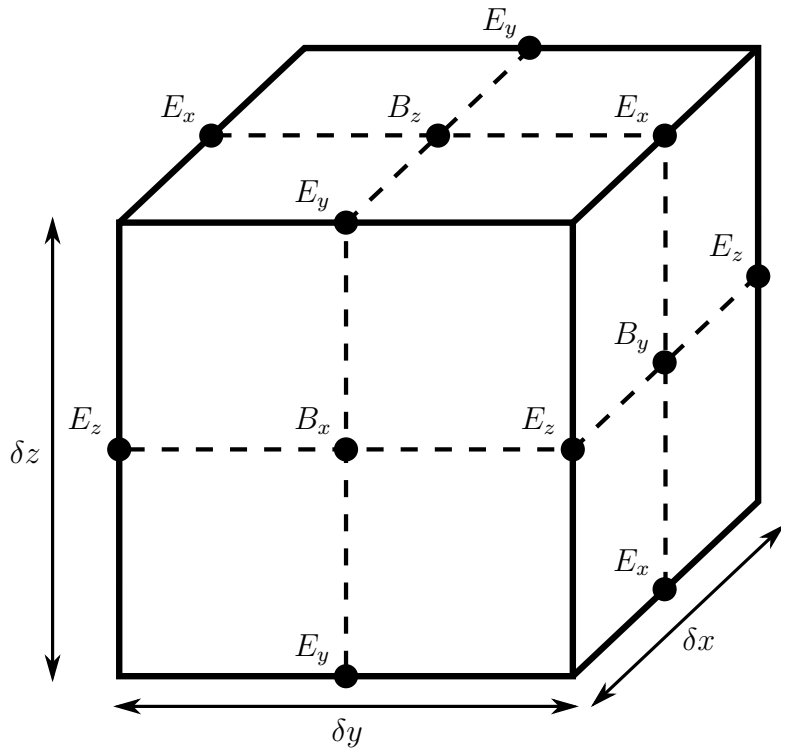

Figure 4: A single Yee cell. These make up the simulation domain. The individual field components are indicated by the dots. The cell itself has dimensions of $\delta x \times \delta y \times \delta z$.

2.1.1 Yee cell

The Yee cell is depicted in figure 4. It is a way of distributing the individual field components in such a way that only second-order central derivatives can be used when calculating the curl. As a reminder, Maxwell's equation in matter in differential form are given as [96].

$$\nabla \cdot \vec{D} = \rho_f \tag{11}$$

$$\nabla \cdot \vec{B} = 0 \tag{12}$$

$$\nabla \times \vec{E} = -\frac{\partial \vec{B}}{\partial t} \tag{13}$$

$$\nabla \times \vec{H} = \vec{J}_f + \frac{\partial \vec{D}}{\partial t}, \tag{14}$$

where $\vec{E}$ and $\vec{B}$ are the electric and magnetic fields respectively. The electric displacement is given as $\vec{D} = \epsilon_0 \vec{E} + \vec{P}$ while the auxiliary field is given as $\vec{H} = \frac{1}{\mu_0}\vec{B} - \vec{M}$ with $\vec{M}$ being the magnetization. The distribution of free charges is given by ρ_f and the free charge current by $\vec{J}$. Free charges are the electrons that are not bound to the atom making up

the material.

I will ignore the magnetization $\vec{M}$ as the materials I work with are not magnetic and there are no currents or free charges flowing so $\vec{J} = 0$ and $\rho_f = 0$, which simplifies the equations. For the FDTD algorithm, we only need equations (13) and (14). Looking at just B_x we have:

$$\frac{\partial B_x}{\partial t} = \frac{\partial E_y}{\partial z} - \frac{\partial E_z}{\partial y}. \tag{15}$$

The derivatives need to be discretized and the beauty of the Yee scheme is that this can be done by second-order central difference derivatives. To see this, consider the Taylor series of functions $f(x + \delta/2)$ and $f(x - \delta/2)$ around x:

$$f(x + \frac{\delta}{2}) = f(x) + f'(x)\frac{\delta}{2} + \frac{1}{2}f''(x)\left(\frac{\delta}{2}\right)^2 + \frac{1}{6}f'''(x)\left(\frac{\delta}{2}\right)^3 + \dots \tag{16}$$

$$f(x - \frac{\delta}{2}) = f(x) - f'(x)\frac{\delta}{2} + \frac{1}{2}f''(x)\left(\frac{\delta}{2}\right)^2 - \frac{1}{6}f'''(x)\left(\frac{\delta}{2}\right)^3 + \dots. \tag{17}$$

Subtracting these two equations and reordering the terms leads to

$$f'(x) = \frac{f(x + \frac{\delta}{2}) - f(x - \frac{\delta}{2})}{\delta} - \frac{\delta^2}{24}f'''(x) + \dots \tag{18}$$

$$= \frac{f(x + \frac{\delta}{2}) - f(x - \frac{\delta}{2})}{\delta} + \mathcal{O}(\delta^2). \tag{19}$$

So by using a central difference discrete derivative, only term of the second order remain, provided we only look at the field values at a distance $\delta/2$ away. Thus the derivative in time can be discretized as

$$\frac{\partial B_x^n(i,j,k)}{\partial t} = \frac{B_x^{n+1/2}(i,j,k) - B_x^{n-1/2}(i,j,k)}{\delta t}, \tag{20}$$

where the index n signifies the time $t_n = n\,\delta t$. Likewise space has been discretized such that $x_i = i\,\delta x$, $y_j = j\,\delta y$, and $z_k = k\,\delta z$. The spatial derivatives of equation (15) are then written as

$$\frac{\partial E_y^n(i,j,k)}{\partial z} = \frac{E_y^n(i,j,k+\frac{1}{2}) - E_y^n(i,j,k-\frac{1}{2})}{\delta z} \tag{21}$$

$$\frac{\partial E_z^n(i,j,k)}{\partial y} = \frac{E_z^n(i,j+\frac{1}{2},k) - E_z^n(i,j-\frac{1}{2},k)}{\delta y}. \tag{22}$$

If we refer back to figure 4, we see that the components on the right side of these equations exactly fall where E_y and E_z are placed in the Yee cell. This holds true for every field component.

Inserting equations (20), (21), and (22) into (15), and reordering the terms leads to:

$$B_x^{n+1/2}(i,j,k) = B_x^{n-1/2}(i,j,k) + \frac{\delta t}{\delta z}\left[E_y^n(i,j,k+\tfrac{1}{2}) - E_y^n(i,j,k-t\frac{1}{2})\right] \quad - \\ \frac{\delta t}{\delta y}\left[E_z^n(i,j+\tfrac{1}{2},k) - E_z^n(i,j-\tfrac{1}{2},k)\right]. \tag{23}$$

So the new value of $\vec{B}$ at time $t_{n+1/2}$ depends on the previous $\vec{B}$ as well as $\vec{E}$ at a half time step ago. The $\vec{E}$ and $\vec{B}$ field follow different time steps, so a single time step consists of updating the $\vec{B}$ field components, which are then used to update the $\vec{E}$ field components. Therefore all of the derivatives are second-order central differences.

In a similar fashion, we can obtain $\vec{D}$ by using equation (14) and using $\vec{H} = \vec{B}/\mu_0$, which is allowed because magnetization is not being considered. This leads to

$$D_x^{n+1}(i+\tfrac{1}{2},j+\tfrac{1}{2},k+\tfrac{1}{2}) = D_x^n(i+\tfrac{1}{2},j+\tfrac{1}{2},k+\tfrac{1}{2}) \quad + \\ \frac{\delta t}{\mu_0 \delta y}\left[B_z^{n+1/2}(i+\tfrac{1}{2},j+\tfrac{1}{2},k+1) - B_z^{n+1/2}(i+\tfrac{1}{2},j+\tfrac{1}{2},k)\right] \quad - \\ \frac{\delta t}{\mu_0 \delta z}\left[B_y^{n+1/2}(i+\tfrac{1}{2},j+1,k+\tfrac{1}{2}) - B_y^{n+1/2}(i+\tfrac{1}{2},j,k+\tfrac{1}{2})\right], \tag{24}$$

which, along with similar expressions for D_y and D_z, gets us the displacement field $\vec{D}$. So what is left is to get $\vec{E}$ from $\vec{D}$. This can be done by inverting $\vec{D} = \epsilon_0\vec{E} + \vec{P}$, which is easy to do for linear optics, where $\vec{P} = \chi^{(1)}\vec{E}$ and even then only when the tensor $\chi^{(1)}$ is diagonal. Most of the FDTD codes and applications are meant for linear optics. For nonlinear optics, things are decidedly more complicated as we shall see in the next subsection.

2.1.2 Implementing nonlinear optics

Our code supports two nonlinear susceptibilities, namely $\chi^{(2)}$ and $\chi^{(3)}$. The second-order susceptibility is used for SHG and currently supports the tensor components $\chi^{(2)}_{yyy}$ and $\chi^{(2)}_{zyy}$. The $\chi^{(3)}$ tensor is only supported as a scalar which applies to all field components equally. In simulations I only illuminated with y-polarized beams and only measure the y-polarized signal thus effectively I only investigate $\chi^{(3)}_{yyy}$. However, the $\chi^{(3)}$ is split in a resonant and nonresonant part for use with CARS and SRS.

Second-order susceptibility

We can rewrite the electric displacement to explicitly separate the linear part from the

nonlinear polarization:

$$\vec{D} = \epsilon_0 \vec{E} + \vec{P} = \epsilon_0 \epsilon_r \vec{E} + \vec{P}_{\mathrm{NL}}, \tag{25}$$

where $\epsilon_r = 1 + \chi^{(1)}$. The non-linear polarization, $\vec{P}_{\mathrm{NL}}$, for SHG is given as

$$\vec{P}_{\mathrm{NL},x} = 0 \tag{26}$$

$$\vec{P}_{\mathrm{NL},y} = \epsilon_0 \chi^{(2)}_{yyy} E_y E_y \tag{27}$$

$$\vec{P}_{\mathrm{NL},z} = \epsilon_0 \chi^{(2)}_{zyy} E_y E_y. \tag{28}$$

The components other than $\chi^{(2)}_{yyy}$ and $\chi^{(2)}_{zyy}$ are set to zero because our group has not yet had a need for the other components and this keeps the equations analytically invertible. To get the electric field, $\vec{E}$, from the electric displacement, $\vec{D}$, I need to invert equation (25). Writing out all of the components with the non-linear polarization filled in gives

$$D_x = \epsilon_0 \epsilon_r E_x \tag{29}$$

$$D_y = \epsilon_0 \epsilon_r E_y + \epsilon_0 \chi^{(2)}_{yyy} E_y E_y \tag{30}$$

$$D_z = \epsilon_0 \epsilon_r E_z + \epsilon_0 \chi^{(2)}_{zyy} E_y E_y. \tag{31}$$

The first is straightforward and is simply $E_x = D_x/(\epsilon_0 \epsilon_r)$. The second one is however more complicated because it is a second-degree polynomial in E_y. We can use the quadratic formula to get the answer:

$$E_y = \frac{-\epsilon_0 \epsilon_r \pm \sqrt{\epsilon_0^2 \epsilon_r^2 + 4 \chi^{(2)}_{yyy} D_y}}{2 \epsilon_0 \chi^{(2)}_{yyy}}. \tag{32}$$

This of course only has a solution if the argument of the square root is larger than zero. The "$-$" solution is not physical because taking the limit of $\chi^{(2)}_{yyy} \to 0$ causes the expression to become infinite. The "$+$" solution goes to $D_y/(\epsilon_0 \epsilon_r)$ in that limit and is therefore the real physical solution. Thus only the "$+$" solution is used in the code. Finally, this expression for E_y can be used to calculate the final component

$$E_z = \frac{D_z - \epsilon_0 \chi^{(2)}_{zyy} E_y^2}{\epsilon_0 \epsilon_r}. \tag{33}$$

This fully calculates $\vec{E}$, which can now be used in the next iteration of the FDTD algorithm to calculate the the magnetic field, $\vec{B}$.

When the argument of the square root above is negative, we can make an approximation by rewriting (30) as

$$D_y^{n+1} = \epsilon_0 \epsilon_r E_y^{n+1} + \epsilon_0 \chi^{(2)}_{yyy} E_y^n E_y^{n+1}. \tag{34}$$

That is, we do not take the square of E_y, but rather the product of future E_y and current E_y. This approximation only holds when $E_y^n \approx E_y^{n+1}$, which should be fine if the time resolution is high enough. Rewriting this, leads to

$$E_y^{n+1} = \frac{D_y^{n+1}}{\epsilon_0 \epsilon_r + \epsilon_0 \chi^{(2)} E_y^n}. \tag{35}$$

The method in this subsection cannot be used with a full $\chi^{(2)}$ tensor, but fortunately, this is sufficient for this thesis because I only consider cylindrical objects that are all aligned in the y-direction and only have a nonzero $\chi^{(2)}_{yyy}$ and are only illuminated by y-polarized light. Future work could allow the fibrils to be rotated along the propagation axis, but they would still be only illuminated by y-polarized light.

Third-order susceptibility

For CARS and SRS we require a resonant and nonresonant susceptibility, which I label as $\chi_R^{(3)}$ and $\chi_{NR}^{(3)}$ respectively. The resonant one corresponds to a Raman-active medium, which means it depends on frequency and is resonant at specific resonance frequency. The nonresonant one on the other hand corresponds to a Kerr medium and is approximated by not depending on frequency. The total third-order nonlinear susceptibility is the sum of the resonant and nonresonant one:

$$\chi^{(3)} = \chi_R^{(3)} + \chi_{NR}^{(3)}. \tag{36}$$

For speedier simulations, the case where $\chi_{NR}^{(3)} = 0$ is handled as a separate case.

Raman without Kerr

The implementation of $\chi^{(3)}$ in the FDTD code necessarily needs to be written in the time domain. In the most general form, the third-order nonlinear polarization can be written as

$$P_{\mathrm{NL}}^{(3)}(t) = \int_{-\infty}^{\infty}\int_{-\infty}^{\infty}\int_{-\infty}^{\infty} \chi^{(3)}(t,t',t'',t''')E(t')E(t'')E(t''')\,dt'\,dt''\,dt'''. \tag{37}$$

Using the Born–Openheimer approximation for the third-order nonlinear polarization, which assumes that the nuclei of the molecules remain static for the electronic solution because the nuclei are so much heavier than electrons, this can be approximated as [89]:

$$P^{(3)} = \epsilon_0 \chi_0^{(3)} E(t) \int_{-\infty}^{t} g(t-t')E^2(t')\,dt', \tag{38}$$

where

$$g(t) = \alpha\delta(t) + \beta g_R(t) \tag{39}$$

$$g_R(t) = \frac{\tau_1^2 + \tau_2^2}{\tau_1\tau_2^2} \exp\left(-\frac{t}{\tau_2}\right) \sin\left(\frac{t}{\tau_1}\right) u(t), \tag{40}$$

and $u(t)$ is the unit step function and the g function is a causal response function. The function g is divided in two parts and regulated by the constants α and β. The first part is the Kerr effect which here is the immediate electronic response and is represented by the delta-function. The second part is the Raman effect which is the retarded response of the atoms which is approximated as a damped oscillation with τ_1 as the characteristic period for the atom vibrations and τ_2 as the damping time constant. This approximation is valid for optical frequencies for almost all material. To have just Raman without Kerr, we set $\alpha = 0$. Then we can write $\chi_R^{(3)}$ as

$$\chi_R^{(3)}(t) = \chi_0^{(3)} g_R(t). \tag{41}$$

Because the polarization contains a convolution integral, we need to somehow keep track of the past. This can be done through an auxiliary variable S, which gets updated every time step as [97]

$$S^{n+1} = a_R S^n + b_R S^{n-1} + c_R (E^n)^2 \tag{42}$$

with

$$a_R = \frac{2 - \omega_R^2\,\delta t^2}{1 + \gamma_R\,\delta t} \tag{43}$$

$$b_R = -\frac{1 - \gamma_R\,\delta t}{1 + \gamma_R\,\delta t} \tag{44}$$

$$c_R = \frac{\chi_0^{(3)}\omega_R^2\,\delta t^2}{1 + \gamma_R\,\delta t}, \tag{45}$$

The variables ω_R and γ_R correspond to the resonant frequency and lifetime respectively and are used as the input parameters for the simulation. Though originally, they come from the time constants as

$$\omega_R = \sqrt{\frac{\tau_1^2 + \tau_2^2}{\tau_1^2\tau_2^2}} \tag{46}$$

$$\gamma_R = \frac{1}{\tau_2}. \tag{47}$$

The auxiliary variable S can be used to calculate the polarization at time step t_{n+1} as

$$P_{\mathrm{NL},R}^{n+1} = \epsilon_0 E^{n+1} S^{n+1}. \tag{48}$$

This polarization term now depends linearly on E^{n+1}, so when used with equation (25), the E^{n+1} can be calculated trivially from the D field as

$$E^{n+1} = \frac{D^{n+1}}{\epsilon_0 \epsilon_r + \epsilon_0 S^{n+1}}. \tag{49}$$

If there is also a Kerr medium, thing get more complicated because equation (48) is no longer linear.

Raman with Kerr

If there is also a Kerr medium present, then equation (48) needs to be expanded to

$$P_{\mathrm{NL},R}^{n+1} = \epsilon_0 E^{n+1} S^{n+1} + \epsilon_0 \chi_K^{(3)} \left(E^{n+1}\right)^3, \tag{50}$$

where $\chi_K^{(3)}$ is the third-order nonlinear susceptibility of the Kerr medium. Because of the third-order polynomial, it is now significantly harder to get an expression for E^{n+1} as a function of D^{n+1}. However, it can still be done with the help of the program *Mathematica*. The expression

$$D^{n+1} = \epsilon_0 \epsilon_r E^{n+1} + \epsilon_0 E^{n+1} S^{n+1} + \epsilon_0 \chi_K^{(3)} \left(E^{n+1}\right)^3 \tag{51}$$

has three solutions, but two of them turn out to be complex-valued. Since the fields in the FDTD simulation are real-valued, only one solution remains, namely

$$E^{n+1} = \frac{2\sqrt[3]{3}\epsilon_0^2 \epsilon_r \chi_K^{(3)} - \sqrt[3]{2} A^{2/3}}{6^{2/3} \epsilon_0 \chi_K^{(3)} \sqrt[3]{A}} \tag{52}$$

with

$$A = \sqrt{3\epsilon_0^4 (\chi_K^{(3)})^3 \left(27\chi_K^{(3)} (D^{n+1} - \epsilon_0 S^{n+1})^2 + 4\epsilon_0^2 \epsilon_r^3\right)} - 9\epsilon_0^2 (\chi_K^{(3)})^2 (D^{n+1} - \epsilon_0 S^{n+1}). \tag{53}$$

For speedier calculation by a factor of eight, this complicated expression is approximated by a 9-th order Taylor expansion for small values of D and S. For large values, the full expression is used.

2.1.3 Boundary conditions

To simulate free space with a finite-sized simulation domain one needs to make sure that its boundaries do not transmit any radiation back into the simulation domain. In other words, they need to be completely absorbing. One cannot simply set the fields to zero at the boundaries because that would effectively make the boundary a perfectly conducting metal, *i.e.* a perfect mirror which is exactly the opposite of what one wants to accomplish.

The first successful absorbing boundary conditions for FDTD that were numerically stable have been created by Mur in 1981 [87]. They were the final missing piece of the puzzle to create an efficient tool for simulating electromagnetic fields in infinite space [85]. It is based on the assumption that the fields at each point on the boundary continue towards infinity as outgoing plane waves perpendicular to the boundary.

Although these boundary conditions are not the most effective ones because waves propagating at an angle to the boundary are not fully accounted for, they are in most cases good enough and are relatively easy to implement. They are also quite memory efficient as only two layers of one cell thick needs to be stored for every face of the simulation domain having absorbing boundary conditions. The first layer contains the values for the fields at the boundary of the simulation domain, while the other layer contains the fields of the outermost cells of the simulation domain from the previous FDTD iteration.

The fields at the boundary must follow the wave equation that can be obtained from equations (13) and (14). By taking the curl of equation (13) one obtains

$$\nabla \times \nabla \times \vec{E} = -\partial_t \nabla \times \vec{B} = -\mu_0 \partial_t \nabla \times \vec{H}. \tag{54}$$

The left-hand side is a vector identity which equals $-\nabla^2 \vec{E} + \nabla(\nabla \cdot \vec{E})$, the second term of which is zero by equation (11) only if the refractive index is homogeneous at the boundaries. Thus for this boundary condition to work, one needs to choose a refractive index for the medium outside of the simulation domain that matches the background medium inside of the simulation domain.

The right-hand side of the equation can be obtained by substituting in equation (14), which leads to

$$-\nabla^2 \vec{E} = -\mu_0 \partial_t^2 \vec{D}. \tag{55}$$

The next assumption is that no nonlinear effects happen on the boundary such that $\vec{D} = \epsilon \mu_0 \vec{E}$. It is also assumed that ϵ does not depend on time so that it can be pulled in

front of the double time derivative. Finally, we are left with a wave equation

$$\left(\nabla^2 - \frac{n^2}{c^2}\partial_t^2\right)\vec{E} = 0. \tag{56}$$

This equation holds for each field component individually and a similar one can be derived for the magnetic fields. Alternatively, this can be written as

$$\left(\nabla^2 - \frac{1}{v^2}\partial_t^2\right)\vec{E} = 0, \tag{57}$$

where $|\vec{v}| = c/n$ is the velocity of the wave in the medium. A general solution to this is of the form $f(\vec{r} \pm \vec{v}t)$ This equation can be factored as

$$\left(\nabla - \frac{\vec{v}}{v^2}\partial_t\right)\left(\nabla + \frac{\vec{v}}{v^2}\partial_t\right)\vec{E} = 0. \tag{58}$$

So either $\left(\nabla - \frac{\vec{v}}{v^2}\partial_t\right)\vec{E} = 0$ or $\left(\nabla + \frac{\vec{v}}{v^2}\partial_t\right)\vec{E} = 0$ which corresponds with the solutions $f(\vec{r} + \vec{v}t)$ and $f(\vec{r} - \vec{v}t)$ respectively.

To apply this in practical terms, consider the boundary condition at $x = 0$ for the z-component of the electric field. We want the outgoing waves to be moving in the negative x direction in this case, so we then choose our function f to be of the form $f(x + v_x t)$, which corresponds to the following differential equation

$$\left(\partial_x - \frac{v_x}{v^2}\partial_t\right)E_z = 0 \tag{59}$$

$$\left(\partial_x - \frac{\sqrt{v^2 - v_y^2 - v_z^2}}{v^2}\partial_t\right)E_z = 0 \tag{60}$$

$$\left(\partial_x - \frac{1}{v}\sqrt{1 - (v_y/v)^2 - (v_z/v)^2}\partial_t\right)E_z = 0 \tag{61}$$

The square root can be expanded as a Taylor series and gives the order of Mur's absorbing boundary condition. In our group's code we use only first-order Mur, that is, the square root is approximated as

$$\sqrt{1 - (v_y/v)^2 - (v_z/v)^2} \approx 1. \tag{62}$$

This implies that we neglect large angles of incidence. The differential equation to solve then simplifies to

$$\left(\partial_x - \frac{1}{v}\partial_t\right)E_z = 0. \tag{63}$$

This approximation discards the directionality of the outgoing plane wave, so that these boundary conditions perform best when the electric fields inside of the simulation domain

approach the boundary head-on. Thus in the corners of the simulation domain, where the fields come in at an angle, the results will be at its poorest. The boundary conditions can be improved by going to second-order Mur, but the benefits are small [87].

This equation needs to be discretized to be compatible with the Yee cell scheme. This can be done by writing the derivatives as central discrete derivatives:

$$\frac{E_z^?(1, j+\frac{1}{2}, k) - E_z^?(0, j+\frac{1}{2}, k)}{\delta x} - \frac{1}{v}\frac{E_z^{n+1}(?, j+\frac{1}{2}, k) - E_z^n(?, j+\frac{1}{2}, k)}{\delta t} = 0. \tag{64}$$

However, there is a problem here if we want to use central difference discrete derivatives. Central difference for the first term means that the derivative is defined at grid point 1/2 in the x-directions, so that means that the question marks in the second term should be 1/2, but that location in the Yee cell that does not exist. Likewise, the central difference derivative for the time would put it at time step $n+1/2$ at which the electric field is not defined. To get around this, a second approximation is required; we take the averages of the neighbouring points that do exist. Thus, the equation then becomes

$$\begin{aligned}
&\frac{1}{2}\left[\frac{E_z^{n+1}(1, j+\frac{1}{2}, k) - E_z^{n+1}(0, j+\frac{1}{2}, k)}{\delta x} + \frac{E_z^{n}(1, j+\frac{1}{2}, k) - E_z^{n}(0, j+\frac{1}{2}, k)}{\delta x}\right] - \\
&\frac{1}{2}\left[\frac{1}{v}\frac{E_z^{n+1}(0, j+\frac{1}{2}, k) - E_z^{n}(0, j+\frac{1}{2}, k)}{\delta t} + \frac{1}{v}\frac{E_z^{n+1}(1, j+\frac{1}{2}, k) - E_z^{n}(1, j+\frac{1}{2}, k)}{\delta t}\right] = 0.
\end{aligned} \tag{65}$$

By rearranging the terms to extract $E_z^{n+1}(0, j+\frac{1}{2}, k)$, the value for the boundary condition for the FDTD algorithm can be obtained as all of the other components are known from the simulation domain or stored from the previous iteration.

$$\begin{aligned}
E_z^{n+1}(0, j+\tfrac{1}{2}, k) = {} & E_z^{n}(1, j+\tfrac{1}{2}, k) + \\
& \frac{v\,\delta t - \delta x}{v\,\delta t + \delta x}\left[E_z^{n+1}(1, j+\tfrac{1}{2}, k) - E_z^{n}(0, j+\tfrac{1}{2}, k)\right].
\end{aligned} \tag{66}$$

The only extra memory requirements come from storing $E_z^n(1, j+\frac{1}{2}, k)$, which will have been overwritten by the FDTD iteration preceding the application of these boundary conditions.

Other boundary conditions exist that are better then Mur's absorbing boundary condition. The most common condition in use today are the PML absorbing boundary conditions. It is a layer of several grid cells thick and contains a nonphysical anisotropic medium where the conductivity depends on the direction that the fields are propagating in. This gives an extra degree of freedom that allows one to solve for zero reflection between the interface of the simulation domain and the PML while still being absorbing.

PML boundary conditions are orders of magnitude better then Mur's boundary conditions [98], however the latter already only reflects 0.1 % of the incoming light in the worst case scenarios which is enough for our purposes and Mur is easier to implement. For the tightly focused beams I generally use, the reflections will not contribute substantially. Tests have shown the effect of Mur boundary conditions of the electric field magnitude near the focus of the beam to be in the order of just 0.001 %.

2.1.4 My contributions

As mentioned before, the bulk of the FDTD code was written by Konstantin Popov. During the course of my Ph.D. I did need to make some modifications to expand its capabilities. Here I will go through the most significant ones.

Near-field probes in the frequency domain

To visualize the electric fields in a manner that allows me to see the near-field enhancements clearly, it is beneficial to look at the field at a certain frequency instead of observing the pulse as it propagates through the medium. This technique is used in figures 16 and 19 in chapter 4. By examining the field at just the pump frequency I was able to see exactly where the input beam is enhanced and how it changes as a function of object shape, size, and position.

Each probe measures the real-valued field E at a given position $(i\,\delta x, j\,\delta y, k\,\delta z)$ and monitors the electric field during the entire simulation at each time step n. This information is used to perform a running discrete Fourier transform (DFT) for a specific frequency ω. The DFT is calculated as follows:

$$E(\omega; i, j, k) = \frac{1}{\sqrt{N+1}} \sum_{n=0}^{N} E^n(i, j, k) e^{2\pi \mathrm{i}\, n\omega}. \tag{67}$$

By placing these DFT near-field probes throughout the simulation domain the input and output field can be visualized separately.

Checkpointing

The simulations for the SRS and CARS simulations of chapter 4 ran on SHARCNET, which is a large high performance computing consortium in Canada. Typically these simulations required 256 CPUs, which are spread out over different compute nodes. With systems of this complexity failure sometimes occurs. Additionally, jobs are only allowed

to run for a specific maximum time before they are terminated automatically. Therefore, as a sort of insurance and a vital step in obtaining results quickly, I implemented checkpointing which is a way to store the state of the program to disk such that it can be continued later on.

Without checkpointing an aborted simulation does not generate results and needs to be restarted. As a typical job runs for three days, these delays quickly add up. Checkpointing allows a running simulation to save its memory content to disk periodically. If a job then fails, it can resume from the last checkpoint it saved and thereby substantially cut down on lost time as well as limit waste of resources.

I implemented checkpointing for our FDTD code by storing to disk the electric and magnetic fields in every MPI process as well as the numerous auxiliary fields and variables that are used by the code.

OpenGL renderer

The FDTD parameters are set through a text file containing the positions and properties of the various media as well those of the input beams. Likewise, the size of the simulation domain and the location of the probes is stored in that text file. However, a text file does not allow a quick overview of the simulation domain and the object within. To reduce the chance of errors in the input files, I implemented a 3D representation of the input file using OpenGL, which is a framework the allows for the real-time rendering of 3D scenes. Since the scene can be rotated and moved at will, it becomes very easy to interpret the input files. Any errors in the placement of objects, probes, or beams becomes quickly apparent, while in the text-based input file it could easily be overlooked.

2.2 Green's function approach for SHG imaging of collagen fibrils

The free-space Green's function solution to the Helmholtz equation is a powerful tool for calculating the electric field in the far-field as a result of some radiating source. It can also be used to calculate the near-fields, but I do not require those. It is much faster than the FDTD method as it is in the frequency domain rather than in the time domain, thus it does not require stepping through time. For my simulations only a single frequency is required; that of the nonlinear process. Furthermore, the far-field signal is in most cases only required at a single point. Calculating the electric field at that point only requires a single integration over the volume of the sample. Of course, this huge speed-up does not come for free. One major downside of using the free-space Green's function is that it assumes the index of refraction to be homogeneous throughout space. It also requires full knowledge of the electric fields inside of the sample.

I use the free-space Green's function for the simulations in chapter 3. I also use it in chapter 6 where I combine the Green's function approach with the cylindrical Mie theory calculations detailed in section 2.3. Finally, the approach also makes an appearance in my theoretical work on ptychography in chapter 5.

The Green's function approach works as follows. First Maxwell's equations are reduced to a Helmholtz equation using what is called the Hertz vector, which is defined through the electric field, $\vec{E}$ as [99]

$$\vec{E} = k^2 \vec{Z} + \nabla(\nabla \cdot \vec{Z}), \tag{68}$$

where k is the wave number and $\vec{Z}$ is the Hertz vector. Furthermore, Maxwell's equations (13) and (14) can be combined to get a free-space wave equation in the frequency domain by assuming the the electric permittivity is homogeneous in space:

$$\nabla \times \nabla \times \vec{E}(\omega) = \frac{n^2\omega^2}{c^2}\vec{E}(\omega) + \mu\mu_0\omega^2\vec{P}_{\mathrm{NL}}(\omega) + \mathrm{i}\mu\mu_0\vec{J}(\omega), \tag{69}$$

where any time-derivative operators have been replaced as $\partial/\partial t \to \mathrm{i}\omega$ and the displacement field has been written as $\vec{D} = \epsilon\vec{E} + \vec{P}_{\mathrm{NL}}$. In addition, the refractive index has been introduced as $n = \sqrt{\epsilon}$ which is in general complex-valued but I take it to be real because I do not consider absorption. The expression for the Hertz vector from (68) can be plugged into this equation to get a differential equation for $\vec{Z}(\omega)$.

$$k^2(\nabla \times \nabla \times \vec{Z}) + 0 = \frac{n^2\omega^2}{c^2}(k^2\vec{Z} + \nabla(\nabla \cdot \vec{Z})) + \mu\mu_0\omega^2\vec{P}_{\mathrm{NL}} + \mathrm{i}\mu\mu_0\vec{J}, \tag{70}$$

which, by using $k = n\omega/c$, can be simplified to

$$\nabla^2 \vec{Z} + k^2 \vec{Z} = -\frac{1}{\epsilon_0 \epsilon} \vec{P}_{\mathrm{NL}} - \mathrm{i} \frac{1}{\epsilon_0 \epsilon \omega} \vec{J}. \tag{71}$$

If we assume that there are no currents and that $\mu = 1$, then we get

$$\nabla^2 \vec{Z}(\vec{r}, \omega) + k^2 \vec{Z}(\vec{r}, \omega) = -\frac{1}{\epsilon_0 n(\omega)^2} \vec{P}_{\mathrm{NL}}(\vec{r}, \omega), \tag{72}$$

which is known as the Helmholtz equation. This equation holds for every vector component individually and can be seen as three separate scalar Helmholtz equations.

2.2.1 Green's function for Helmholtz equation

The solution to the scalar equation

$$\nabla^2 G_0(\vec{r}, \vec{r}) + k^2 G_0(\vec{r}, \vec{r}') = -\delta(\vec{r} - \vec{r}') \tag{73}$$

is well known and is the scalar free-space Green's function

$$G_0(\vec{r}, \vec{r}) = \frac{e^{\pm \mathrm{i} k |\vec{r} - \vec{r}'|}}{4\pi \, |\vec{r} - \vec{r}'|}, \tag{74}$$

where the $+$ indicates outgoing waves and the $-$ indicates incoming waves. I use the outgoing waves, since I am studying radiating sources. With the help of this Green's function, the Hertz vector can be calculated as

$$\vec{Z}(\vec{r}, \omega) = \frac{1}{\epsilon_0 n(\omega)^2} \int_V G_0(\vec{r}, \vec{r}') \vec{P}_{\mathrm{NL}}(\vec{r}', \omega) \, dV'. \tag{75}$$

This integral is easily numerically solved and can be converted back into the electric field through equation (68), though in the far-field the electric field can also be approximated as $\vec{E} = k^2 \vec{Z}$. The integral runs over the entire spatial domain, but because the induced nonlinear polarization only occurs within the object of study, this is equivalent to just performing the integral over the volume of the object. A graphical representation is shown in figure 5. The downside of this method that the integral has to be performed for each location $\vec{r}$, so one cannot get the electric fields everywhere in space as that would be computationally prohibitive. Fortunately, for the purpose I require it for, only a few points in the far-field are required, making this method orders of magnitude faster than FDTD simulations.

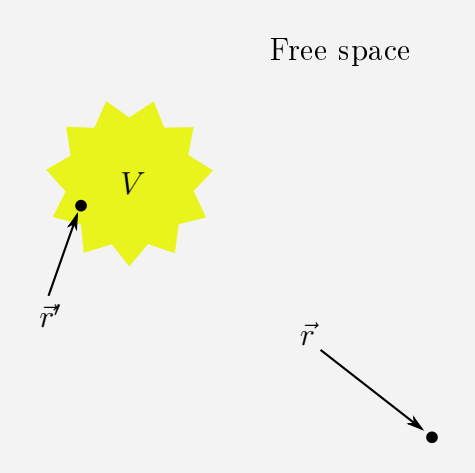

Figure 5: Integration domain of the Green's function. The integral is over the coordinate $\vec{r}'$ and runs over the entire object with volume V to calculate the electric field at coordinate $\vec{r}$ outside the object.

2.2.2 Green's function for SHG

This method was originally implemented by Konstantin Popov to study the imaging by SHG of collagen fibrils as will be discussed in chapter 3. For SHG, the nonlinear polarization is

$$P_{\mathrm{NL},i}(\vec{r}, 2\omega) = \epsilon_0 \sum_{j,k} \chi^{(2)}_{ijk}(\vec{r}, 2\omega = \omega + \omega) E_j(\vec{r}, \omega) E_k(\vec{r}, \omega), \tag{76}$$

where the summations over j and k both run over x, y, and z, while $\vec{E}$ is the electric field at the excitation frequency; we are assuming an undepleted pump approximation. Konstantin Popov's program originally only had support for a single component of the $\chi^{(2)}$ tensor, namely $\chi^{(2)}_{yyy}$. This was enough for me to use the program to simulate the SHG radiation of cylinders aligned along the y-direction, illuminated by a y-polarized Gaussian beam propagating in the x-direction. I used this to run the simulations required for the research in chapter 3.

I have since extended the program to support the full 27-component tensor while allowing the cylinders to be rotated in arbitrary directions. Since the program is geared towards collagen fibrils, I can make use of the fact that there are really only three

independent nonzero components. For collagen cylinders, the d-matrix is given as [100]

$$d = \begin{bmatrix} 0 & 0 & 0 & 0 & 0 & d_{16} \\ d_{21} & d_{22} & d_{21} & 0 & 0 & 0 \\ 0 & 0 & 0 & d_{16} & 0 & 0 \end{bmatrix}. \tag{77}$$

Some elements appear twice because cylindrical symmetry dictates that x and z are interchangeable. In the case of Kleinman symmetry there are only two independent components as then $d_{21} = d_{16}$. The d-matrix is related to the $\chi^{(2)}$ tensor through [14]

$$d_{i\ell} = \frac{1}{2}\chi^{(2)}_{ijk}, \tag{78}$$

where ℓ is related to jk as

$$\begin{array}{cccccccc} jk: & 11 & 22 & 33 & 23,32 & 31,13 & 12,21 \\ \ell: & 1 & 2 & 3 & 4 & 5 & 6 \end{array}. \tag{79}$$

The indexes for i, j, and k can take the values 1, 2, and 3, which corresponds with the coordinates x, y, and z respectively.

The fibrils can be rotated in arbitrary directions, which means that not only the spatial dimensions of the cylinders need to be rotated, but also that the $\chi^{(2)}$ tensor must rotate accordingly. Rotating a tensor is slightly more involved than rotating a vector, but the same principles apply. For example, to rotate a vector $\vec{a}$ by an angle θ in the xy-plane, one would multiply the vector by a rotation matrix R as follows:

$$\vec{a}' = \begin{bmatrix} \cos\theta & \sin\theta & 0 \\ -\sin\theta & \cos\theta & 0 \\ 0 & 0 & 1 \end{bmatrix} \begin{bmatrix} a_x \\ a_y \\ a_z \end{bmatrix} = R\,\vec{a}. \tag{80}$$

In tensor notation, this can be written as $a'_j = R_j{}^i a_i$, where the summation over i is implied. To rotate the $\chi^{(2)}$ tensor, a similar transformation can be done, but this time over all the indexes:

$$\chi^{(2)\,\prime}_{\ell mn} = R_m{}^i R_n{}^j R_\ell{}^k \chi^{(2)}_{ijk}, \tag{81}$$

where there is an implicit summation over i, j, and k.

Combining the rotated fibrils in space with the rotation of the $\chi^{(2)}$ tensor allows me to simulate SHG imaging of fibrils in any orientation. Figure 6 shows the far-field SHG intensity signal resulting of a fibril that has $\chi^{(2)}_{yyy} = 0.14$ while the other components are

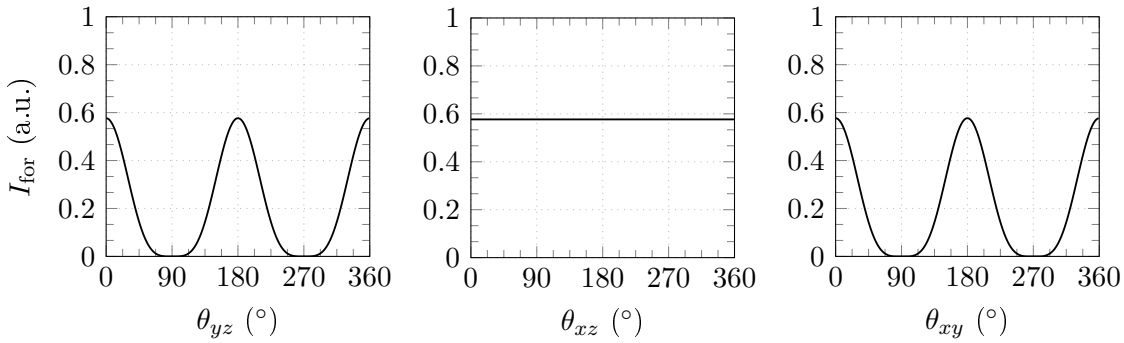

Figure 6: The SHG intensity signal in the forward direction versus, from left to right, a rotation of the fibril in the yz, xz, and xy plane. The fibril has $\chi^{(2)}_{yyy} = 0.14$ while the other components are zero.

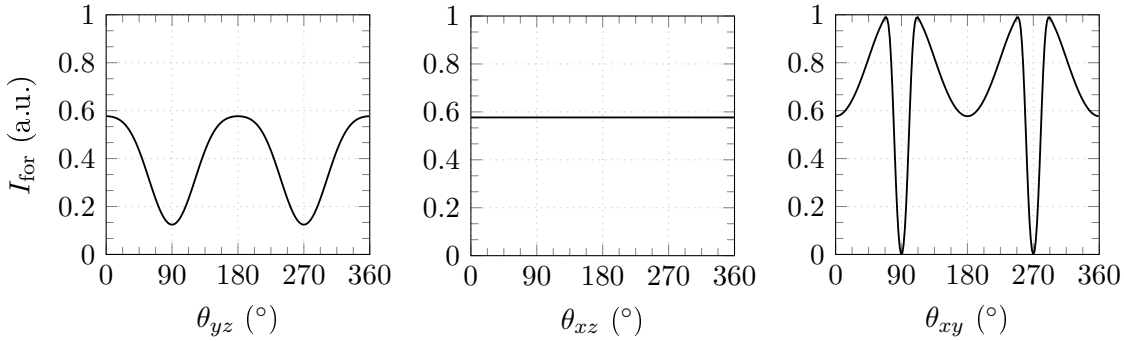

Figure 7: The SHG intensity signal in the forward direction versus, from left to right, a rotation of the fibril in the yz, xz, and xy plane. The fibril has $\chi^{(2)}_{yyy} = 0.14$ and $\chi^{(2)}_{xyy} = 0.065$ while the other components are either zero or follow Kleinman symmetry.

zero. The cylinder is illuminated by a Gaussian beam with a wavelength of 1000 nm and a waist of 1.1 µm. Both the fibril and the surrounding medium have a refractive index of $n = 1.4$. From the middle plot, it can be seen that a rotation of the fibril in the xz-plane has no effect because the cylinder is aligned along the y-axis. Figure 7 shows the same rotations under the same illumination, but now with $\chi^{(2)}_{yyy} = 0.14$ and $\chi^{(2)}_{xyy} = 0.065$. The other components are either zero or follow Kleinman symmetry. The third plot for the rotation in the xy plane shows a higher far-field SHG intensity signal because the fibril is being rotated towards the laser propagation axis. Thus despite the fact that the effective $\chi^{(2)}$ decreases due to the rotation, more of the material is illuminated and thus more signal is generated.

The code supporting rotation of fibrils can be used on collections of multiple fibrils

to model tissue samples where the fibrils are not all aligned in the same direction. This is planned as a future project. Currently no results are available.

2.3 Cylindrical Mie theory

Mie theory allows for the calculation of the near-field inside and outside a geometrical object with a refractive index that is different from the background medium. Like the Green's function approach, the Mie solution is an analytical solution to the Maxwell's equations. Unlike the Green's function approach however, it does take into account a refractive index mismatch. It was first developed by Gustav Mie in 1908 [101]. The solution he described is for a plane wave illuminating a spherical object [102], but solutions also exist for non-spherical objects, such as cylinders [103, 104], which is what is used in the simulations for chapter 6.

To get an analytical solution for the electromagnetic field, the wave equation from Maxwell's equation needs to be solved using cylindrical coordinates. Mie theory assumes that the refractive index inside the cylinder, n_{in}, is homogeneous, as well as the refractive index outside of the cylinder, n_{out}. However, generally $n_{\text{in}} \neq n_{\text{out}}$.

I will not endeavour to give a full derivation of the Mie solution for cylinders. Partly because the solution is already derived by H.C. van de Hulst [103], but also because the actual implementation was done by the combined work of two undergraduate students, Julien Roy and Charalambos Kioulos, the latter of which was under my supervision. What follows is merely the overview of the derivation to highlight the key points.

The wave equation that follows from Maxwell's equations for a system without free charges is

$$\nabla \times \nabla \times \vec{E}(\omega, \vec{r}) - \frac{n^2\omega^2}{c^2}\vec{E}(\omega, \vec{r}) = 0, \tag{82}$$

where ω is the frequency of the incoming light and n can be either n_{in} or n_{out}. Using the identity $\nabla \times \nabla \times \vec{A} = \nabla(\nabla \cdot \vec{A}) - \nabla^2\vec{A}$ and the fact that $\nabla \cdot \vec{D} = \epsilon\nabla \cdot \vec{E} = 0$, this wave equation can be rewritten as

$$\nabla^2\vec{E}(\omega, \vec{r}) + \frac{n^2\omega^2}{c^2}\vec{E}(\omega, \vec{r}) = 0. \tag{83}$$

This is the familiar Helmholtz equation that we already saw in section 2.2. However, this time it needs to be solved for cylindrical boundary conditions instead of free space. To facilitate the solving of this equation, the vectorial Helmholtz equation can be transformed into scalar one by introducing the derived vector fields $\vec{M}$ and $\vec{N}$ such that [103]

$$\vec{M} = \nabla \times (\vec{r}\psi) \tag{84}$$

$$\vec{N} = \frac{n\omega}{c}\nabla \times \vec{M}, \tag{85}$$

where ψ is the new scalar field that satisfies

$$\nabla^2\psi(\omega,\vec{r}) + \frac{n^2\omega^2}{c^2}\psi(\omega,\vec{r}) = 0. \tag{86}$$

Then the electric field is given as

$$\vec{E} = \vec{M} + \mathrm{i}\vec{N}. \tag{87}$$

The scalar Helmholtz equation needs to be solved using cylindrical coordinates, (ρ,θ,z), because of the cylindrical boundary conditions, thus the equation becomes

$$\frac{\partial^2\psi}{\partial\rho^2} + \frac{1}{\rho}\frac{\partial\psi}{\partial\rho} + \frac{1}{\rho^2}\frac{\partial^2\psi}{\partial\theta^2} + \frac{\partial^2\psi}{\partial z^2} + \frac{n^2\omega^2}{c^2}\psi = 0. \tag{88}$$

The cylinders are considered to be aligned along the z-axis. The equation can be solved using separation of variables. That means the solution is a product of $\sin(\nu\theta)$ or $\cos(\nu\theta)$ with a ν-th order Bessel function of the first or second kind for the dependence on ρ. The full solution can be written as [103]

$$\psi_\nu = e^{\mathrm{i}\nu\theta} Z_\nu\left(\rho\sqrt{\frac{n^2\omega^2}{c^2} - h^2}\right) e^{-\mathrm{i}hz}, \tag{89}$$

where h is an arbitrary constant while ν is an integer and Z stands for the Bessel function. It should be noted that these functions form a complete basis, that is, any arbitrary function can be expressed as a superposition of the above solutions.

Now that the Helmholtz equation is solved, the boundary conditions need to be applied. There are two types: the boundary conditions at infinity and those at the surface of the cylinder. Since the cylinder is illuminated from the outside by a plane wave, which scatters off the cylinder, the electric field outside of the cylinder can be written as $\vec{E}_{\mathrm{inc}} + \vec{E}_{\mathrm{scatter}}$. Inside the cylinder the field is denoted by $\vec{E}_{\mathrm{cyl}}$. The incoming field, $\vec{E}_{\mathrm{inc}}$ is known and can be expressed in terms of the basis function from equation (89). Furthermore, the scattered wave should behave as an outgoing cylindrical wave, which means it will be a Hankel function of the second kind, *i.e.* $J_n - \mathrm{i}Y_n$. This is analogue to the spherical case, where the scattered field at infinity should be an outgoing spherical wave.

Finally, the boundary conditions at the cylinder surface are used to determine the linear coefficients of the superposition of (89) that compose the interior electric field and those of the scattered wave. These boundary conditions arise from Maxwell's equations

as well and are

$$\hat{n} \times (\vec{E}_{\text{out}} - \vec{E}_{\text{in}}) = 0 \tag{90}$$

$$\hat{n} \times (\vec{H}_{\text{out}} - \vec{H}_{\text{in}}) = 0 \tag{91}$$

$$\hat{n} \cdot (n_{\text{out}}^2 \vec{E}_{\text{out}} - n_{\text{in}}^2 \vec{E}_{\text{in}}) = 0 \tag{92}$$

$$\hat{n} \cdot (\vec{H}_{\text{out}} - \vec{H}_{\text{in}}) = 0. \tag{93}$$

This leads to a linear system of equations for each order ν which can be solved to generate the coefficients for the electric field inside the cylinder and outside. This is a lengthy calculation, in the end it leads to

$$\vec{E}_{\text{in}}(\rho, \theta, z) = \sum_{\nu=0}^{N} d_\nu \frac{n_{\text{in}}}{n_{\text{out}}} (-\mathrm{i})^\nu e^{\mathrm{i}\theta} J_\nu(k_{\text{in}}\rho) \tag{94}$$

$$\vec{E}_{\text{out}}(\rho, \theta, z) = \sum_{\nu=0}^{N} (-\mathrm{i})^\nu e^{\mathrm{i}\theta} \left(J_\nu(k_{\text{out}}\rho) - b_\nu H_\nu^{(2)}(k_{\text{out}}\rho) \right), \tag{95}$$

where the coefficients d_ν and b_ν are given by

$$d_\nu = \frac{\left(H_{\nu-1}^{(2)}(\alpha) - H_{\nu+1}^{(2)}(\alpha) \right) J_\nu(\alpha) - H_\nu^{(2)}(\alpha) \left(J_{\nu-1}(\alpha) - J_{\nu+1}(\alpha) \right)}{\frac{n_{\text{in}}}{n_{\text{out}}} \left(H_{\nu-1}^{(2)}(\alpha) - H_{n+1}^{(2)}(\alpha) \right) J_\nu(\beta) - \frac{n_{\text{in}}^2}{n_{\text{out}}^2} H_\nu^{(2)}(\alpha) \left(J_{\nu-1}(\beta) - J_{\nu+1}(\beta) \right)} \tag{96}$$

$$b_\nu = \frac{n_{\text{in}}(J_{\nu-1}(\beta) - J_{\nu+1}(\beta)) J_\nu(\alpha) - n_{\text{out}} J_\nu(\beta)(J_{\nu-1}(\alpha) - J_{\nu+1}(\alpha))}{n_{\text{in}}(J_{\nu-1}(\beta) - J_{\nu+1}(\beta)) H_\nu^{(2)}(\alpha) - n_{\text{out}} J_\nu(\beta)(H_{\nu-1}^{(2)}(\alpha) - H_{\nu+1}^{(2)}(\alpha))}. \tag{97}$$

And furthermore, $\alpha = k_{\text{out}} a$ and $\beta = k_{\text{in}} a$ with a being the radius of the cylinder.

Using this method in combination with the free-space Green's function approach from section 2.2 allows one to calculate the far-field signal. This can be employed to study the effect of refractive index mismatches between collagen fibrils and their surrounding medium as I will do in chapter 6. It is orders of magnitude faster than comparable FDTD simulations. It however does not account for the effect of refractive index on generated nonlinear radiation, though in future work this can be accounted for by using a cylindrical Green's function approach instead [105]. If multiple cylinders are present in very close proximity to each other, then the Mie-Green's function approach does not account for the effects of neighbouring cylinders and FDTD is required to account for those.

2.4 Generating a distribution of collagen fibrils

For the research in collagen fibrils, I needed to numerically generate the tissue sample to be imaged as well. For chapters 3, 5, and 6, simulated rat tail tendon, human cartilage and cornea is required. These tissues consist of fibrils that are mostly aligned in the same direction on the scale of the laser focal spot and can thus be modelled as cylinders that are all parallel to the y-axis. The difference between the tissues is given by three properties, the number of fibrils with a positive and negative $\chi^{(2)}$, and the distribution of fibril diameters.

The distribution of fibril diameters can be a fixed diameter which is how I model cornea, where fibrils have effectively a single size, and cartilage, where the fibril diameter is only considered to vary with tissue depth. The distribution can also be a custom distribution meant to resemble rat tail tendon [106, 107]. The total number of fibrils in the simulation domain is determined by the packing fraction, ρ, which is the ratio of the area in the xz-plane that the fibrils occupy to the total area of the simulation domain in the xz-plane. Finally, the positive-to-total ratio, f is determined by the number of fibrils with a positive second-order nonlinear susceptibility to the total number of fibrils as

$$f = \frac{N_+}{N_+ + N_-}, \tag{98}$$

where N_+ is the number of fibrils with a positive susceptibility and N_- with a negative one. The fibrils can be either positive or negative because the collagen proteins are achiral and they assemble into fibrils in such a way that this property is preserved along hundreds of microns along the length of the fibril [108]. Thus depending on the chirality, the sign of the $\chi^{(2)}$ is determined.

Our group already had code to generate these collections of fibrils by randomly trying to place a fibril in the simulation domain and simply reject it if it overlapped with any of the previously placed fibrils. While this method works well to create collections of fibrils with a packing fraction up to $\rho = 0.5$, it fails to create more densely packed collections because the already placed fibrils leave no room for additional fibrils.

To overcome this, I have written a molecular dynamics simulation to distribute the fibrils. It works as follows. First fibrils are randomly generated using a size distribution until the required packing fraction is reached. Then these fibrils are randomly placed in the simulation domain, where many of them will initially overlap. Finally, the molecular dynamics simulation runs on these fibrils, which pushes them apart until none of the fibrils overlap anymore. This method is able to reach $\rho = 0.7$ using the rat tail tendon

diameter distribution. Both the fibril diameter distribution and the molecular dynamics simulation are detailed below.

2.4.1 Diameter distribution

In nature, collagen fibril diameters follow specific size distributions depending on the type of tissue and age. For example, human cornea has fibrils that within a very tight margin have a diameter of 32 nm, whereas rat tail tendon for 13–14 week old rats follow a distribution of the form [107]

$$f(d) = \frac{4d}{d_0^2} \exp\left(-\frac{2d}{d_0}\right), \tag{99}$$

where d is the diameter and d_0 is the mean diameter. This formula was chosen to have a convenient analytical form that fits the actual diameter distribution; there is no significant meaning behind it.

Rat tail tendon tissue of rats younger than 13 weeks follow a bimodal Gaussian distribution of the form [106]

$$f(d) = c_1 \exp\left(-\frac{(d-d_{0,1})^2}{\sigma_1^2}\right) + c_2 \exp\left(-\frac{(d-d_{0,2})^2}{\sigma_2^2}\right), \tag{100}$$

where $c_{1/2}$ are the height of the peaks, $\sigma_{1/2}$ are the widths, and $d_{0,1/2}$ are the mean diameters for each peak. Tail tendon of mature mice follows a similar distribution to that of young rats, except that instead of bimodal, the diameters follow trimodal Gaussian distribution.

To generate these distributions numerically, various techniques can be employed. Konstantin Popov has programmed the rat tail tendon distribution for 13–14 week old rats by inverting the normalized cumulative distribution. This allows one to use an uniform random number generator to generate a number between 0 and 1, which is then used as an argument for the inverted distribution. The output is a diameter that follows the original distribution.

I implemented the bimodal distribution by employing the Boost libraries, which contain a random number generator for normally distributed samples. I implemented the bimodal distribution by first using an uniform random number generator to select either Gaussian $i = 1$ with probability $\frac{c_1}{c_1+c_2}$ or Gaussian $i = 2$ with probability $\frac{c_2}{c_1+c_2}$. Then I select a diameter using the normal distribution with mean $d_{0,i}$ and width σ_i. The trimodal Gaussian distribution is implemented similarly.

2.4.2 Molecular dynamics simulation

A molecular dynamics simulation involves N particles experiencing a force. In its simplest form, *i.e.* the "forward Euler" algorithm, the acceleration, velocity, and position for each particle is updated every time step according to the equations [109]

$$\vec{a}_i^{n+1} = \Delta t \sum_{\substack{j=0 \\ j\neq i}}^{N} F(\vec{x}_i^n, \vec{x}_j^n) \tag{101}$$

$$\vec{v}_i^{n+1} = \vec{v}_i^n + \vec{a}_i^{n+1}\,\Delta t \tag{102}$$

$$\vec{x}_i^{n+1} = \vec{x}_i^n + \vec{v}_i^{n+1}\,\Delta t, \tag{103}$$

where the force F usually depends on the position of both the i-th particle and that of the other particles through an attractive or repulsive force. It should be mentioned that "forward Euler" algorithm is generally the worst for simulating physical processes because it tends to suffer from energy drift which means that the total energy of the system is not conserved. However, it suits my purposes perfectly as I am only interested in getting the fibrils to not overlap anymore; the motion itself is not of interest.

The molecular dynamics simulations starts with overlapping fibrils. I then define a force on a cylinder at positions $\vec{x}_1$ from one at $\vec{x}_2$ with radii r_1 and r_2 as

$$\vec{F} = \begin{cases} -\frac{\vec{x}_1 - \vec{x}_2}{|\vec{x}_1 - \vec{x}_2|} & |\vec{x}_1 - \vec{x}_2| \leq r_1 + r_2 \\ \vec{0} & |\vec{x}_1 - \vec{x}_2| > r_1 + r_2 \end{cases}. \tag{104}$$

That is, if the cylinders overlap, they will experience a repulsive force, otherwise no force is applied. More complicated expressions for the force are possible but lead to slower convergence. The boundaries of the simulation domain are elastic such that cylinders hitting the boundaries are reflected.

To achieve convergence, the speed of the cylinders is reduced by 50 % every time step, which leads to exponential decay. Therefore, cylinders that are no longer touching will quickly settle in their final position because they experience no forces. Convergence is usually reached within seconds depending on the input parameters.

In figure 8, three frames are shown from an example molecular dynamics simulation. A box was chosen of $1\,\mu\text{m} \times 1\,\mu\text{m}$. The diameters of the cylinders were randomly chosen to reflect fibrils found in 13–14 week old rat tail tendon. The number of cylinders is such that the packing fraction is $\rho = 0.70$. The initial placement of the cylinders is shown in the left plot where most of the cylinders overlap. Then the molecular dynamics simulation is started. The middle plot shows the result after 100 iterations. Only two

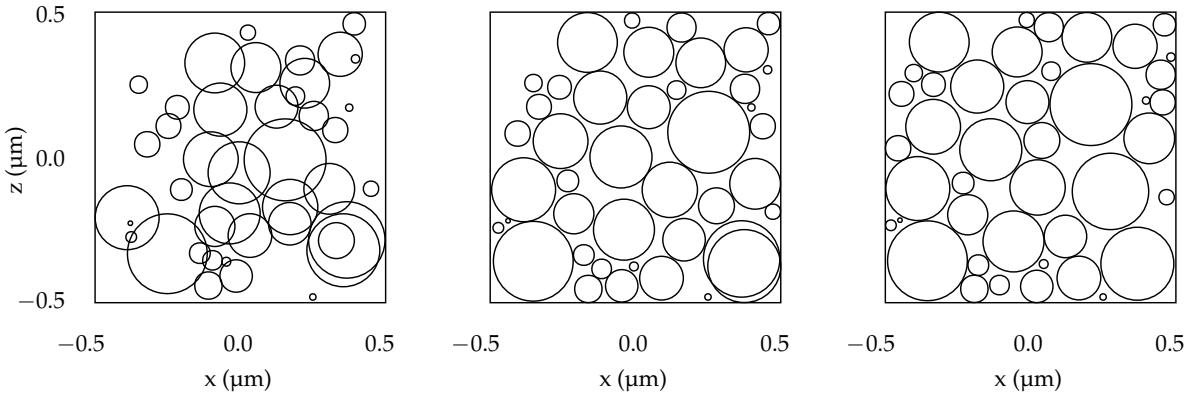

Figure 8: Three frames from the molecular dynamics simulation. The left plot is the initial random placements of the cylinders with overlapping circles. The middle plot shows iteration 100 and the right plot shows the last converged sample at iteration 708.

cylinders still overlap in the bottom because they are large and started in the corner. The right plot shows the converged simulation after 708 iterations. The cylinder that was overlapping at iteration 100 has been pushed towards the centre while pushing the other cylinders away to make room.

3

Obtaining subwavelength information using Second Harmonic Generation

SHG is a nonlinear optical imaging technique that is particularly well-suited for imaging collagen fibrils. The maximum theoretical obtainable resolution of any optical imaging technique is limited by the Abbe diffraction limit which is $\lambda/2$, where λ is the wavelength of the SHG signal. For collagen imaging the wavelength of the input beam is 810 nm. Because of the frequency doubling, the maximum observable detail is thus 203 nm . Fibrils diameters are almost always smaller than that and therefore cannot be imaged directly with SHG.

However, since SHG is a coherent technique, interference effects can occur between individual fibrils. Through careful modelling it is possible to extract additional information about the subwavelength structure of the sample. For example, two papers on which I am co-author demonstrate this. The first shows that the ratio of the SHG intensity signal in the forward and backward direction, the F/B ratio, has information about the fibril diameter [1]; this is described in section 3.1. The other, described in section 3.2, demonstrates how obtaining the the phase information using interferometric SHG provides insight into the orientation of fibrils within the sample [2]. In both cases

I provided the numerical modelling to relate experimental results to the subwavelength properties. In as yet unpublished work, I also studied imaging of collagen in cornea, that is intended to be part of a collaborative experimental-theoretical future work; I describe this in subsection 3.3.

3.1 Analysis of fibril diameters in bone and cartilage

For the first paper, Houle et al. [1] investigate collagen type I as it is found in human bone as well as type II as it can be found in articular cartilage. The type designation refers to the tissue's macrostructure. In type I, the fibrils are aligned in tight bundles at the microscale but on the 10 µm scale these bundles are oriented in different directions. For type II collagen, the fibrils are more randomly oriented at the microscale but still present an overall constant orientation on the macroscale. Types I and II are one of the most common and form fibrillar structures, where type I can be found most often in bone, skin, and tendon, whereas type II is usually found in cartilage [37]. The structural changes of the collagen in these tissues are related to ageing, wound healing and disease. Therefore it is important to be able to examine these fibrillar structures at the nanoscale.

One way of doing this is, is by imaging the sample in both the forward and backward direction with a SHG microscope. Since SHG is a coherent technique, phase matching conditions are crucial in forming the radiation pattern. If the phases of the incoming beam and the generated outgoing beam match perfectly, there will be purely constructive interference from the microscopic fibrils, resulting in strong radiation. Without phase matching, the SHG radiation will interfere with its neighbouring scatterers and destructive interference will occur depending on how the neighbouring scatterers are distributed. Destructive interference also occurs in bulk material when using a focused beam due to the Gouy phase shift. However, the fibrils considered here are small, thus this does not occur. I assume for simplicity that the refractive index at ω is the same as at 2ω, which is a valid approximation as the difference in the refractive index of collagen only differs by $\Delta n = 0.03$ at the wavelengths used. Thus only for length scales of more than 4 µm would an effect be noticeable; fibrils are much smaller than that. I have phase matching if the relation of $\vec{k}_{\mathrm{SHG}} + \vec{k}_{\mathrm{input}} = 0$ holds, where $\vec{k}_{\mathrm{SHG}}$ is the wave vector of the SHG radiation and $\vec{k}_{\mathrm{input}}$ that of the input beam. Thus by looking at the ratio of the forward and backward direction, information about the inner structure of the tissue can be gleaned.

A 10 µm slice of human knee cartilage and bone was imaged using a laser-scanning SHG microscope in both the forward and backward direction. In the forward direction

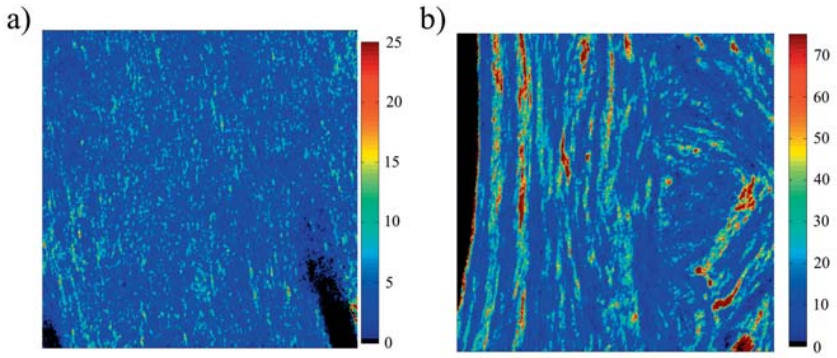

Figure 9: Experimental image of forward-to-backward ratio of articular cartilage (a) and bone (b) [1]. The colour bar indicates the F/B ratio. Images are 100 µm × 100 µm.

the signal is collected by a photomultiplier tube through an objective that has an NA of 0.8 and in the backward it is collected through the microscope objective and then passed through a dichroic mirror onto another photomultiplier tube. The polarization is rotated such that the maximum signal is obtained which occurs when the polarization of the incoming beam is aligned with the direction of the fibrils. Since we were interested in the forward-to-backward (F/B) ratio of the sample, this means we needed to compensate for difference in the detection efficiency between the forward and backward direction. This was done by calibrating the microscope using two-photon excited fluorescence (TPEF) of a solution of Coumarin 440. Since TPEF emits equally in every direction the signal strength in both the forward and backward direction is the same.

The solution was then substituted by the actual sample of cartilage or bone, of which a SHG image was obtained in both the forward and backward direction by raster scanning. This was then assembled in a single 2D image displaying F/B ratio as a function of position as seen in figure 9. The F/B ratio was found to range from 1 to 70, where a ratio of 1 indicates that the sample at that position radiates equally strong in the forward as in the backward direction. A ratio of 70 means that the fibrils there show a strong preference to emit in the forward direction. In itself, this does not provide detailed information about the internal structure. However, by performing numerical simulations we are able to connect these values to fibril diameter size.

My contribution was to model the forward and backward intensity using the Green's function approach outlined in section 2.2 on a collection of fibrils of fixed diameter d. A single such collection is shown in figure 10. As the samples I consider are thin, backscattering is ignored. The fibrils are represented by infinitely long cylinders along the

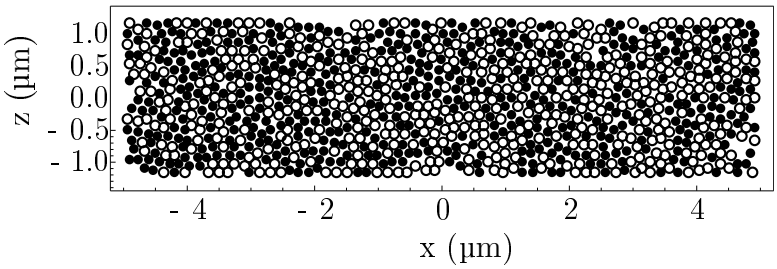

Figure 10: Example of a typical fibril distribution for human cartilage with fixed diameter of 150 nm and filling fraction of $\rho = 0.7$. Cylinders are aligned in the y-direction. Filled disks indicate a fibril with positive $\chi^{(2)}$ while empty circles indicate negative $\chi^{(2)}$.

y-axis while the input beam was modelled as a y-polarized Gaussian beam propagating in the x-direction. Furthermore, the simulated sample has a filling ratio ρ, which is the ratio of the area in the xz-plane occupied by the cylinders over the total area. For different ρ and d a thousand samples were generated with the cylinders placed at random locations using the methodology outlined in section 2.4. Typically, each sample contains thousands of fibrils depending on the fibril diameter. Each fibril in a sample has either a positive of negative second-order nonlinear electric susceptibility, $\chi^{(2)}$. The probability is for a positive or negative $\chi^{(2)}$ is assumed to be equal. Work in the next section shows the probability to be between 45 % to 55 %. In this thesis, in figure 33, I also show that this does not impact the results presented here.

Each sample is then illuminated by a Gaussian beam with wavelength 810 nm and a waist size of 1.25 µm. For each sample, the electric field of the SHG signal in the far-field was calculated using the Green's function approach on each fibril in the sample and summing their far-field electric fields. From the electric field of the SHG signal in the far-field, the far-field SHG intensity is obtained. An ensemble average of the intensities in the forward direction is taken over all the samples, and same for the intensities in the backward direction. The ratio of those averages is the F/B ratio.

The results of the simulations are shown for a fixed diameter $d = 150$ nm as a function of filling ratio ρ in figure 11a. It can be seen that the F/B ratio does not depend on the filling ratio ρ, even though the forward and backward SHG signal do depend on ρ (not shown). Figure 11b shows the F/B ratio for a fixed filling ratio $\rho = 0.6$ as a function of fibril diameter and shows that the F/B ratio does depend on the diameter d of the cylinders. Since the F/B ratio depends only on the diameter and not on the filling ratio, this allows us to link the F/B ratio directly to the cylinder diameter. Thus given a F/B ratio, we can use figure 11b to infer the fibril diameter.

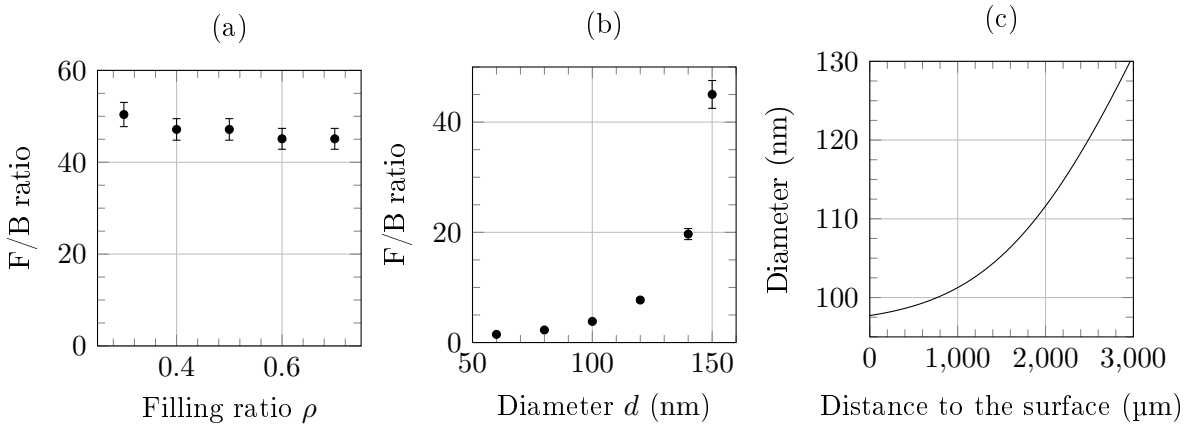

Figure 11: F/B ratio as a function of filling fraction ρ for a constant diameter of $d = 150\,\text{nm}$ (a) and for a constant filling fraction of $\rho = 0.60$ (b) [1]. Incident laser beam has waist of 1.25 µm and wavelength of 810 nm. The inferred fibril diameter as a function of depth is shown in (c).

Returning back to figure 9, We can now claim that areas in bone where the F/B ratio is 70 corresponds to a fibril diameter of 160 nm. On the other hand, in cartilage, the F/B ratio is only as high as 8, which corresponds to a maximum diameter of 11 nm. Recall that these SHG images were created using an image beam with a wavelength of 810 nm. Therefore the wavelength of the SHG radiation is 405 nm which leads to an Abbe diffraction limit of 203 nm. The fibril diameters we obtained from modelling the image formation process is well below this diffraction limit, *i.e.* we obtained subresolution information using SHG imaging.

Using the 3D capabilities of nonlinear optical imaging by moving the laser focus into the sample, we can measure the F/B ratio as a function of depth. The absorption of the tissue, which would affect the measured forward and backward signal is taken into account through the calibration with TPEF. By linking the measured F/B ratio directly to the fibril diameter, we can produce the plot shown in figure 11c which shows the fibril diameter as a function of depth. As we go deeper into the cartilage from the surface towards the cartilage-bone interface, the fibril diameter increases from 85 nm to 125 nm. These observations match what is known in literature where scanning electron microscopes were used [110, 111].

We were successfully able to link the measured F/B ratio to the fibril diameters using SHG microscopy alone through numerical modelling. In doing so, we are able to glean information about the tissue at length scales smaller than the diffraction limit

for frequency of the SHG radiation. These finding can be used to track changes in the fibrillar structure of tissue due to ageing or disease.

3.2 Fibril alignment in cartilage

More information can be obtained than just the fibril diameters. It is also possible to study the alignment of the fibrils in tissue using the coherence properties of SHG, which is the second paper I co-authored [2]. In it, we study juvenile equine cartilage, which contains type I collagen, using a new technique called interferometric SHG (I-SHG).

It is known that in these tissues the fibrils tend to align in parallel and anti-parallel fashion, which means that the fibrils either have a positive or negative $\chi^{(2)}$ [14, 108, 112]. This means a positive fibril will emit SHG radiation that is out of phase with that of a negative fibril by π, which will affect the I-SHG image. It also means that the SHG signal from two close-by fibrils with opposite polarity will cancel out. Therefore the SHG signal does not only depend on the density of scatters, but also its structure. In normal SHG imaging it is therefore not possible to directly relate regions of low far-field SHG in the image to the absence of collagen; there may in fact be significant amounts of collagen present. This depends on the number of fibrils with positive $\chi^{(2)}$, N_+, and negative, N_-. We define the ratio f as before as

$$f = \frac{N_+}{N_+ + N_-}. \tag{105}$$

If the ratio f is 0.5, then equal numbers of positive and negative fibrils are present and this can be expected to reduce the SHG signal significantly, though not completely, as the f ratio is defined over a large region of tissue, and there are statistical variations within the sample from laser shot to laser shot. If we were to know what the value of f is, we can take this into account when interpreting the SHG image. We show that the f ratio can be obtained from the phase information of the second-order nonlinear susceptibility.

I-SHG allows for the retrieval of the phase information from a sample by interfering the scanning laser microscope with a reference beam. The reference beam is generated by sending the input beam through a quartz plate, so both the input beam and the reference beam traverse the sample. The input beam generates SHG radiation inside the sample, which subsequently interferes with the reference beam. By introducing a phase delay, ϕ_{ref}, the signal received by the PMT either constructively or destructively interferes according to the simple relation $\cos(\phi_{\text{exp}} - \phi_{\text{ref}})$. The intensities are measured

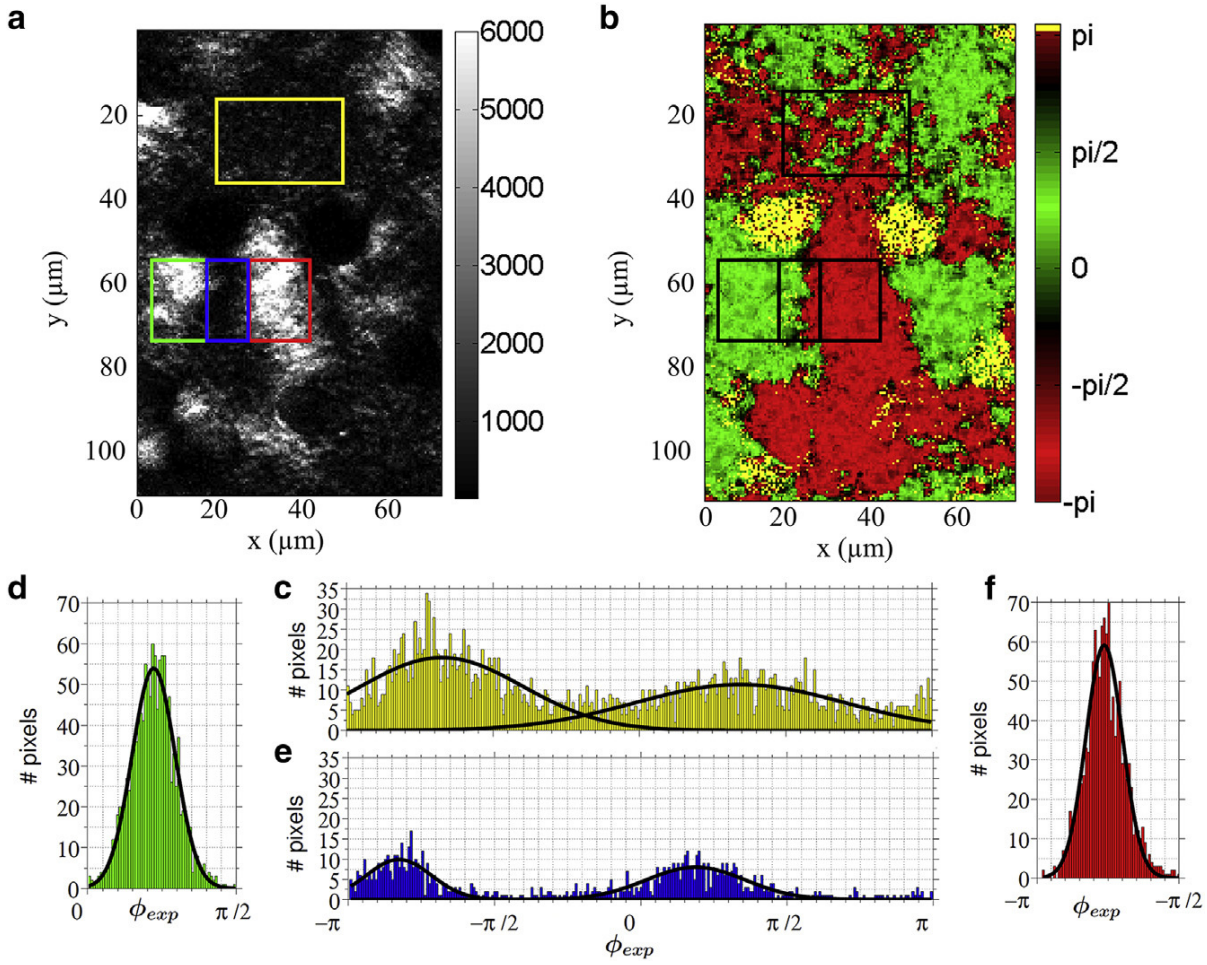

Figure 12: Experimental image of equine cartilage is shown for intensity (a) and phase (b). The coloured boxes in (a) are regions of interest for which the phase distribution is shown in (c), (d), (e), and (f) [2]. Copyright © 2015 Biophysical Society. Published by Elsevier Inc. All rights reserved.

multiple times at the same pixel with different values of ϕ_{ref}. Fitting the cosine function to the measured intensities as a function of this phase delay, allows for the full retrieval of ϕ_{exp}, which is the phase introduced by the sample and can range from $-\pi$ to π. The full experimental setup is detailed in [2].

Figure 12a shows a typical SHG intensity image, whereas figure 12b shows the phase. The yellow areas indicate areas where there is not enough intensity to reliably determine the phase, but the red and green sections clearly have a determined phase. The phase distribution in the regions of interest are shown in figure 12c, d, e, and f. The high intensity areas in the green and red square have a sharp peak, which means the phase is well-defined there. In those areas f deviates from 0.5 significantly, leading to mostly constructive interference and thus high intensity. The blue and yellow boxes on the other hand have little intensity, but a look at the phase distribution in figure 12e shows two distinct peaks. This means that the low SHG intensity measured there is not the result from a low density of scatters, but rather destructive interference.

In fact, the widths of the peaks contain information about the underlying f ratio. To extract this information we require the use of the simulations I ran. The simulations are similar to those in the previous section, that is, the fibrils were modelled as cylinders aligned in the y-direction with either a positive of negative $\chi^{(2)}$. The cylinders were randomly placed in a non-overlapping manner such that the filling ratio is $\rho = 0.7$ which corresponds approximately to those found in nature. They were then illuminated by a Gaussian beam with a waist size of 1.1 µm and wavelength of 810 nm as was used in the experiment. Both the cylinders and the surrounding medium have a refractive index of $n = 1.4$, where the refractive index of the surrounding medium is assumed to be the same as that of the fibrils. The ratio f was varied from 0.25 to 0.75 and for each f a thousand numerically generated samples were simulated and the far-field phase was collected in each case. Then the standard deviation of the phase of the SHG field was determined for each f as well as the intensity. The result is plotted as the black points in figure 13. Figure 13a shows the ratio f as a function of standard deviation σ. When the number of positive or negative fibrils is dominant, it can be expected that the measured phase if always close to 0 or π for each sample. That is, the standard deviation is going to be small. On the other hand, when the number of positive and negative is nearly equal ($f = 0.5$), then the phase in the far-field is going to be different for each simulated sample. The standard deviation in that case if going to be very large. This is indeed what we see in figure 13a. Likewise, when most of the fibrils are either positive of negative,

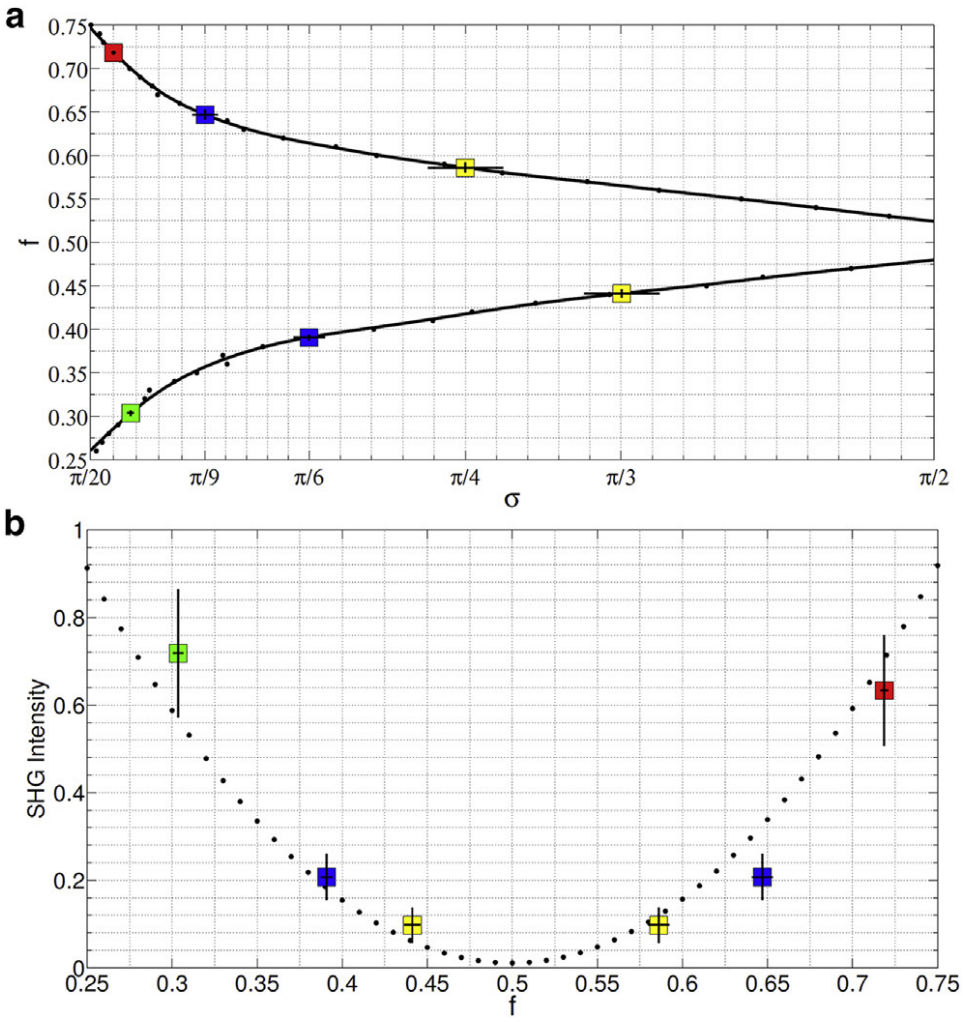

Figure 13: (a) shows the ratio of positive cylinder, f, as a function of the standard deviation of the phase, σ. (b) shows the SHG intensity signal as a function of f [2]. The black dots are the results of simulations for 1000 samples illuminated by a Gaussian beam with waist 1.1 µm and wavelength of 810 nm. The coloured squares correspond to the coloured regions of interest from figure 12a.

the far-field signal is going to be the result of many fibrils coherently adding up and will therefor be large. With similar numbers of positive and negative fibrils, the far-field signal will suffer from destructive interference and be low. This is shown in figure 13b.

By comparing these simulations to the experimental measurements, we can obtain the f ratio in the regions of interest. The coloured boxes from figure 12a are shown in figure 13 and correspond to the measured standard deviation in figure 13a and intensity in 13b. The green region of interest has a small standard deviation and large intensity. Based on the standard deviation, the f ratio in that region should correspond to $f = 0.30$. Of course, it also matched $f = 0.70$, but we can determine from the phase measurement by the I-SHG microscope that most of the fibrils in that region have a negative $\chi^{(2)}$, thus $f = 0.30$. Likewise, the red region of interest has mostly positive fibrils and thus $f > 0.5$. Based on the measured standard deviation, the region of interest will have $f = 0.72$. The blue and yellow regions are more ambiguous as there are two peaks in the phase graph from figure 12c and e. Matching the standard deviation from each peak to figure 13a results in blue having f between 0.39 and 0.65 and yellow being between $f = 0.44$ and $f = 0.59$.

When we plot the SHG intensity as a function of these found f ratios, we get the plot shown in figure 13b. The measured SHG intensity lines up well with the SHG intensity predicted by the simulations, which further proves that the resulting SHG signal is the result of interference rather than density as each simulation was performed as the same density.

In conclusion, I-SHG is a great tool for investigating the alignment of fibrils in collagen tissue. We can obtain information about the sample on the nanoscale, well below the optical resolution of the SHG microscope. Using my simulations, we have been able to show that SHG signal intensity does not arise solely from scatterer density, but is highly dependent upon the underlying nanoscale structure because SHG is a coherent process.

In chapter 5, I introduce an alternative technique for retrieving the phase information without interferometry. It is based on a computational iterative reconstructive algorithm that uses far-field intensity patterns captured by a CCD camera.

3.3 Imaging cornea

Another interesting collagen-containing tissue is cornea, which is the transparent layer that sits on top of the eye pupil and iris. Damage to the cornea could lead to loss of sight and it is therefore important to be able to study changes in the structure of cornea.

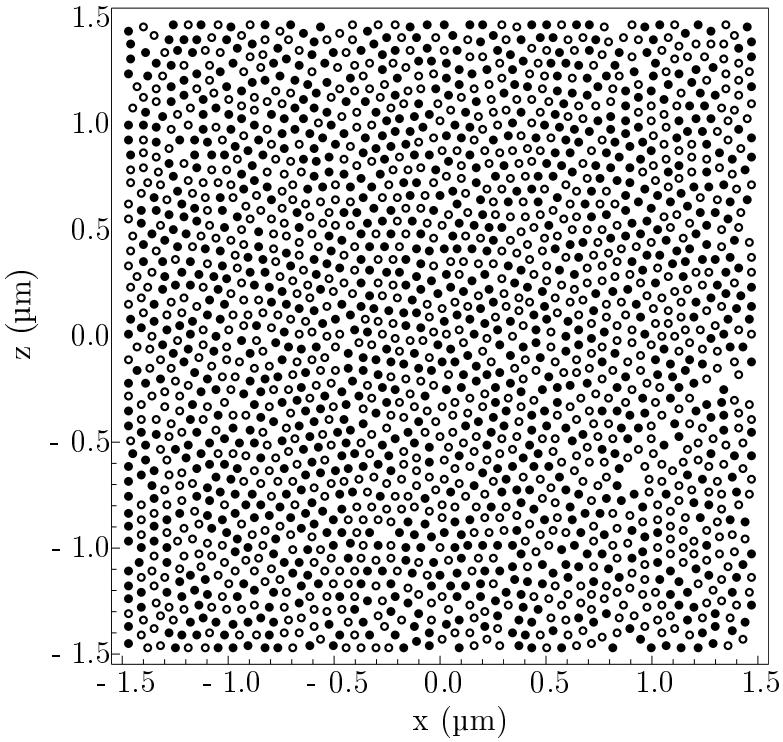

Figure 14: Example of a typical fibril distribution for cornea with fixed diameter of 32 nm and average distance of 64 nm from centre to centre. Cylinders are aligned in the y-direction. Filled disks indicate a fibril with positive $\chi^{(2)}$ while empty circles indicate negative $\chi^{(2)}$.

Genetic disorders such as keratoconus leads to thinning and deformation of the cornea tissue [113]. Wound healing and maturing also intimately affects fibril organization [114, 115]. Typically these fibrils have diameters of only tens of nanometers and are therefore hard to be directly image with any optical technique or require the use of electron or atomic force microscopes. However, structural information can still be obtained by once again using SHG microscopes. For example, cornea tissues diseased with keratoconus can be distinguished from healthy cornea using SHG microscopy [116].

The fibrils in cornea have a diameter of 32 µm are not tightly packed but maintain a distance of 64 nm from centre to centre, which allows them to be transparent [37, 117]. A sample simulated distribution is shown in figure 14. The fibrils are aligned in sheets called lamellae which are about 3 µm thick. These lamellae are rotated with respect to each other. While imaging these structures, it has been found that images obtained in the forward direction show structure while the image in the backward direction are just a speckle pattern [29, 118]. By running simulations for a single lamella, I am able to show

that this is caused due to the randomization of the phase in the backward direction. As the fibrils themselves are small, they act as dipole emitters, so a single fibril will have the same forward and backward signal. However, when a distribution of fibrils is present, each fibril will have a random position. That means that there will be phase difference between the fibrils, but only in the backward direction.

To visualize this, assume two fibrils in positions (x_1, y_1) and (x_2, y_2) with $x_2 > x_1$ are illuminated by a plane wave travelling in the x-direction with wave number k_i. At the first fibril, the propagation phase of the incident light is $k_i x_1$ assuming it was zero at the origin. Since the induced nonlinear polarization is $P \propto E^2$, this means that the phase imprinted on the generated SHG radiation with wave number $k_{\mathrm{SHG}} = 2k_i$ is $k_{\mathrm{SHG}} x_1$. Similarly, the phase of the incoming plane wave and subsequently the induced SHG radiation at the second fibril is $k_i x_2$ and $k_{\mathrm{SHG}} x_2$ respectively.

In the forward direction, the SHG radiation from the first fibril will travel to the second, picking up an additional propagation phase of $k_{\mathrm{SHG}}(x_2 - x_1)$, which makes the final phase $k_{\mathrm{SHG}}(x_2 - x_1) + k_{\mathrm{SHG}} x_1 = k_{\mathrm{SHG}} x_2$, which is exactly the phase of the SHG radiation imprinted on the SHG radiation from the second fibril. Because the phase is the same, full constructive interference occurs in the forward direction in the limit where we can ignore walk-off due to dispersion. As before, I still consider the refractive index to be the same for the input beam and the SHG radiation.

In the backward direction, the SHG radiation from the second fibrils instead travels to the first fibril. The propagation phase it picks up is, as before, $k_{\mathrm{SHG}}(x_2 - x_1)$. Thus the total phase of the SHG radiation from the second fibril at the first fibril $k_{\mathrm{SHG}}(x_2 - x_1) + k_{\mathrm{SHG}} x_2 = k_{\mathrm{SHG}}(2x_2 - x_1)$, which does not match the phase of $k_{\mathrm{SHG}} x_1$ that is generated by the first fibril. This phase difference between the SHG radiation of the first and second fibril leads to destructive interference depending on the relative positions of the fibrils.

These statements hold true for large collections of fibrils as well; SHG radiation in the forward direction always adds coherently while in the backward direction it does not. In the lamellae, the fibrils are all aligned. However, they may be parallel or anti-parallel to each other, that is, the second-order nonlinear susceptibility is either positive or negative. I again calculate the forward and backward far-field SHG intensity signal using the same Green's function formalism as before but now with an input beam with a waist of 0.525 µm and wavelength of 810 nm. Due to nonlinear susceptibility being randomly positive of negative with equal probability, destructive interference can also occur in the forward direction, the phase is however still well-defined as seen in figure 15.

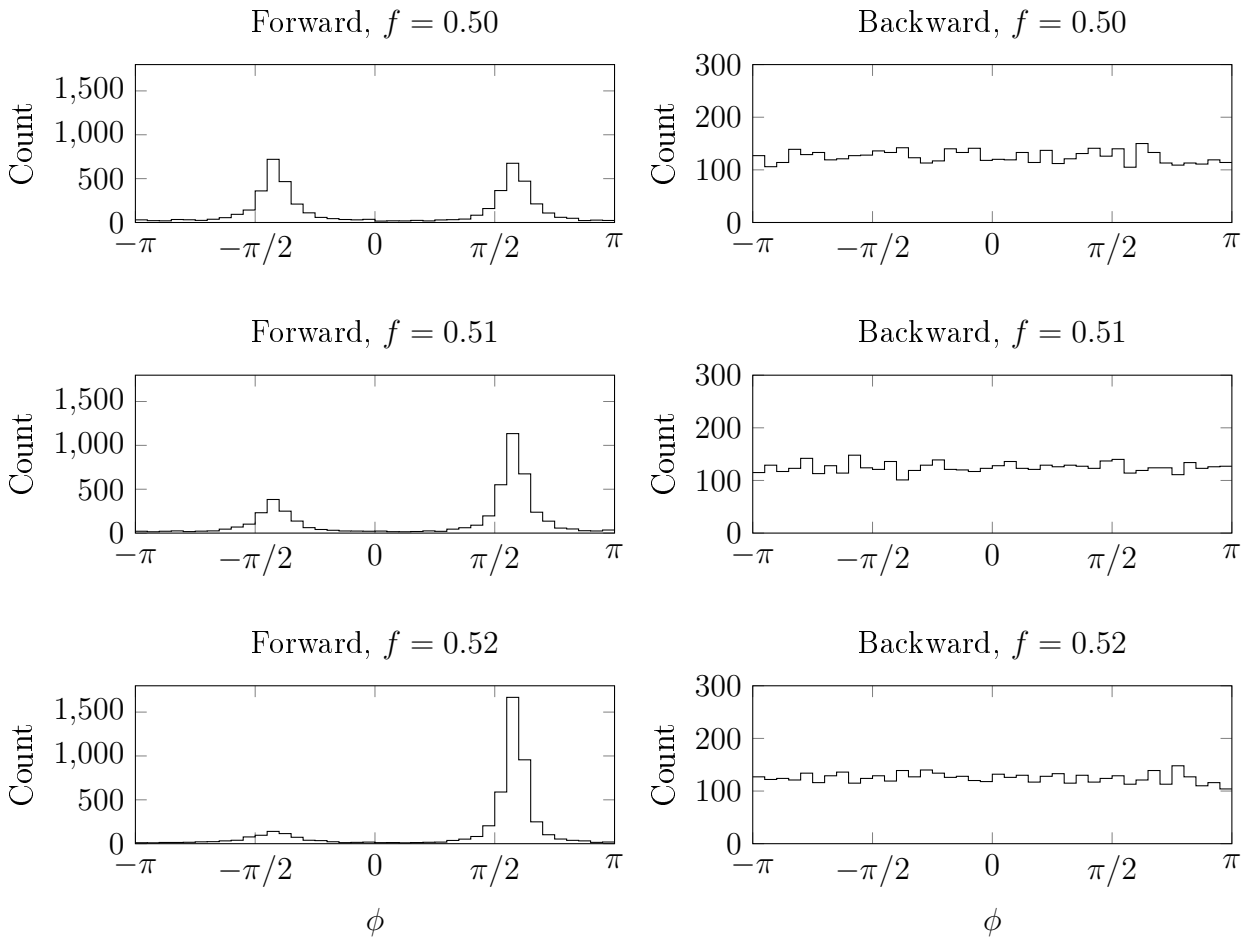

Figure 15: Distribution of phase in the forward and backward direction for a positive-to-total ratio of $f = 0.50, 0.51, 0.52$.

For the forward direction two distinguished peaks are visible for $f = 0.5$ in the top left plot of figure 15, while for the backward direction in the top right plot of figure 15, the phase is uniformly distributed. As the ratio of positive fibrils to total number of fibrils, f, is increased just slightly (middle and bottom rows of figure 15) a single peak is becomes dominant. Due to the random nature of the distribution of positive and negative fibrils, the f number will fluctuate naturally, so a well-defined phase in the forward direction is expected, which explains why in the forward direction one can observe structure, but not in the backward direction where the interference destroys any image formation.

4

Effects of refractive index mismatch on SRS and CARS microscopy

This chapter is a verbatim copy of my article "Effects of refractive index mismatch on SRS and CARS microscopy" that was published in *Optics Express*[1] [90]. It should be noted that even though the article concerns only SRS and CARS, it may apply to other nonlinear optical techniques as well.

4.1 Introduction

Nonlinear optical imaging microscopes allow for label-free non-destructive imaging of biological processes in cells and tissues [78, 119]. Two such techniques are stimulated Raman scattering (SRS) microscopy and coherent anti-Stokes Raman scattering (CARS) microscopy, which allow for video-rate [51, 54, 55] and hyperspectral imaging [77], where in the latter per-pixel spectral information is obtained. Using broadband CARS one can obtain high resolution 3D images of the entire fingerprint region [48], where most

[1] J.N. van der Kolk, A.C. Lesina and L. Ramunno, *Effects of refractive index mismatch on SRS and CARS microscopy*, Optics Express, **24**(22):25752 (2016)

organic molecules have their identifying Raman peaks and ranges from 500–2000 cm^{-1}. Meanwhile, SRS with its linear dependence on density and enhanced contrast has been used to obtain multispectral images at 30 frames per second allowing one to identify virtually any organic molecule, even when their vibrational spectra are very similar [55], including in the fingerprint region [120]. This is useful for biomedical applications such as tracking drugs as they move through tissue [62, 63], detecting tumours [64], and the tracking of newly synthesized proteins as they are being produced [65].

For these imaging techniques to produce reliable images, it is crucial to understand the nonlinear image formation mechanisms, especially with regards to contrast and distortions. Due to the coherent nature of CARS, interference of the CARS signal with the signal from the nonresonant background (NRB) can occur — even when techniques such as FM-CARS are used — resulting in reduced contrast, spatial shifts [69] and spatial-spectral coupling, where distortions in the Raman spectrum as retrieved from the CARS spectrum were observed [76]. Unlike CARS, SRS does not have a comparable nonresonant process, but when the background is inhomogeneous in the nonresonant third-order non-linear susceptibility, a background signal can be generated on the same order of magnitude as the SRS signal [70].

In this paper, we find that the difference between the refractive index of an object and the background medium, even when $\Delta n/n < 0.12$, can cause significant distortions of SRS and CARS images due to near-field enhancement of the input laser beams and microlensing. Though the modest differences in the indices of refraction in biological material between the objects and the background medium are exploited in phase-contrast microscopy [6], these differences are ignored in most models for CARS and have not been explored in SRS. For CARS, it is known that such a refractive index mismatch in the surrounding medium can cause the epi-CARS signal to be masked by reflections of the forward CARS signal [121]. Microlensing through spheres on top of a glass plate has been investigated as well and shows photonic nanojets forming as well as diffraction rings in the far field [122]. The linear index can also cause shadows in the nonresonant background [71] though filtering techniques such as FM-CARS have not been investigated in that regard. In theoretical work in CARS, enhancements to the induced nonlinear polarization near the interface of a single dielectric sphere and a surrounding medium have been explored [72] as well as the near-field enhancements for two such spheres [73]. These last two works, however, did not not have the nonlinear effects directly incorporated in their FDTD simulations but instead manually obtained the induced

polarization from the calculated input field and used the free space Green's function to propagate the CARS signal into the far-field. Additionally, they only considered objects at the laser focus which does not represent a true measure of the strength of the far field CARS signal, due to interference effects with the background anti-Stokes signal [69].

We use FDTD simulations to show that significant changes of the measured SRS and CARS signal can occur in the far-field images depending upon the refractive indices, the shape of the Raman scatterer, and the position of the input laser focus. The enhanced near fields of the input beams around and within a single Raman-active sphere do not have a large effect on the magnitude of the CARS and SRS signal. They do, however, affect the perceived object position. Furthermore, when only off-resonant material is present, false SRS and CARS far-field signals occur due to inhomogeneities in the refractive index alone.

We then turn our attention to a pair of spheres and observe CARS and SRS signals can be an order of magnitude larger than what would be expected and object positions are shifted up to 1.0 µm. One sphere acts as a microlens, and creates a field enhancement inside the second sphere, leading to an enhanced CARS or SRS polarization. Microlensing from dielectric spheres on top of a sample has been used to create photonic nanojets to obtain superresolution CARS images [123], whereas the microlensing here is due to the internal objects present in the sample. This internal microlensing we found leads to an enhancement and shifted position in the image, suggesting a larger scatterer density than actually exists in the object. These effects depend on the numerical aperture (NA) of the collection lens and can be reduced, but not eliminated, by increasing the NA. This microlensing effect continues to create large signal enhancements when the spheres are moved several sphere radii apart, and causes the sphere closer to the laser source to be masked by the first one, up to a separation distance of 1.0 µm for two $r = 0.5$ µm spheres. Understanding these mechanisms is key to correctly interpreting CARS and SRS images.

4.2 Methods

We employ FDTD to study the impact on SRS and CARS images of refractive index mismatch between wavelength-sized spherical objects and a background medium. The input laser beams are Gaussian beams focused by a parabolic mirror. Intensities are measured in the far-field by taking the electric field at the domain boundary, extracting a particular frequency component using a direct Fourier transform and then using the fields at that frequency to calculate the far-field using a free-space Green's function

approach. This near-to-far-field transformation is an exact solution for a homogeneous background medium outside of the simulation domain and is equivalent to extending the simulation domain. Furthermore, the obtained far-fields are integrated over the surface of a collection lens so any diffraction effects are automatically accounted for. Inside the simulation domain, near fields are measured at the pump and Stokes frequencies through a discrete Fourier transform in time. The polarization for SRS at the Stokes (ω_S) and pump (ω_p) frequencies can be written as [14]

$$P_{\mathrm{SRS}}(\omega_S) = 6\epsilon_0\chi_R^{(3)}(\omega_S = \omega_p - \omega_p + \omega_S)|E(\omega_p)|^2E(\omega_S) \tag{106}$$

$$P_{\mathrm{SRS}}(\omega_p) = 6\epsilon_0\chi_R^{(3)}(\omega_p = \omega_p - \omega_S + \omega_S)E(\omega_p)|E(\omega_S)|^2, \tag{107}$$

where $\chi_R^{(3)}$ is the frequency-dependent resonant third-order nonlinear susceptibility and ϵ_0 is the vacuum permittivity. The electric fields in the medium as a result of illumination by the input pump and Stokes beams are represented by $E(\omega_p)$ and $E(\omega_S)$ respectively. The polarization for CARS can be written as

$$P_{\mathrm{CARS}}(2\omega_p - \omega_S) = 3\epsilon_0\left[\chi_R^{(3)}(\omega_{AS} = \omega_p + \omega_p - \omega_S) + \chi_{NR}^{(3)}\right]E^2(\omega_p)E^\star(\omega_S), \tag{108}$$

where ω_{AS} is the anti-Stokes frequency and $\chi_{NR}^{(3)}$ is the nonresonant third-order non-linear susceptibility, which we take to be that of a frequency independent Kerr medium. Our implementation of $\chi_R^{(3)}$ and $\chi_{NR}^{(3)}$ automatically calculates both polarizations. We solve the non-magnetic 3D Maxwell equations in CGS units, using

$$\vec{D} = \left[1 + 4\pi\left(\chi^{(1)}(\vec{r} + \chi_{NR}^{(3)}(\vec{r})E^2\right)\right]\vec{E} + 4\pi\vec{P}_R, \tag{109}$$

where $\chi^{(1)}$ and $\chi_{NR}^{(3)}$ are the first- and third-order instantaneous susceptibilities, respectively, and the polarization of the resonant medium is [97]

$$\vec{P}_R(\vec{r},t) = \frac{1}{4\pi}\vec{E}\cdot\left(\chi_R(\vec{r},t)\star E^2(t)\right), \tag{110}$$

where $\star$ denotes a convolution and

$$\chi_R(\vec{r},t) = \chi_R^{(3)}(\vec{r})\mathcal{F}^{-1}\left(\frac{\omega_R^2}{\omega_R^2 - \omega^2 + 2\mathrm{i}\,\omega\gamma_R}\right). \tag{111}$$

Here, $\chi_R^{(3)}(\vec{r})$ is the time-independent amplitude of the Raman susceptibility, ω_R the resonant frequency of molecular vibrations, and γ_R the damping factor; $\mathcal{F}^{-1}$ denotes the inverse Fourier transformation. The χ_R allows us to simulate the nonlinear polarizations for both SRS and CARS. This, along with the particular values of the nonlinear coefficients used, is described in section 3 of Popov et al. [69].

When the difference $\omega_p - \omega_S$ matches a resonance in the Raman spectrum of the molecule of interest, the induced polarization is very strong and becomes the dominant source for the measured signal. This is what allows for label-free imaging. For CARS the signal measured at ω_{AS} does not come only from the induced polarization that scales with $\chi_R^{(3)}$, but also from nonresonant processes ($\chi_{NR}^{(3)}$), which we model as a frequency-independent Kerr medium and are responsible for the NRB. It is generally much weaker than the CARS signal, but its effect increases as the size of the Raman-active object decreases, and becomes comparable to the wavelength of the input beams. Often frequency modulation of one of the input beams is used to reduce the effects of the NRB, thus we include FM-CARS in our studies. The SRS process leads to loss in the pump beam and gain in the Stokes beam which is measured at the pump or Stokes frequency. The change in signal is very small compared to the input beams, so an AM or FM lock-in technique is used to extract the SRS signal. Therefore, for SRS, we study both AM-SRS and FM-SRS.

Our simulation domain contains either one or two spheres in a background medium. The objects can have a linear refractive index either different from, or the same as, the background medium. Additionally, the background medium always has a homogeneous $\chi_{NR}^{(3)}$ to simulate the NRB while the spheres can be made Raman-active by setting $\chi_R^{(3)}$ non-zero. Because we can turn on and off all of these individual properties, we can determine the consequence of each effect separately. We use $\lambda_S = 800\ nm$ and $\lambda_p = 1042\ nm$ beams in a medium with $n = 1.33$. The objects themselves can have $n = 1.5$ or $n = 1.33$. The entire simulation domain has a size of $12 \times 12 \times 12\,\mu\text{m}$ with a resolution of 25 nm [70].

The input beams are Gaussian laser beam sources, tightly focused through a parabolic mirror of radius 500 µm with an NA of 0.95 and a ratio of beam waist to mirror radius of 0.4. The focal point is at the centre of the simulation domain. The far-field signal is collected by integrating over a transverse area in the far field corresponding to an NA of 0.6, except for simulations where we vary the NA from 0.1 to 0.6. For ease of calculation, we simulate the scanning of the laser over the sample by moving the object inside the simulation domain and keep the laser focus constant. As we only move along the laser propagation axis, we consider only normal incidence. The pump and Stokes beams propagate in the x direction and are polarized in the y direction. The objects are placed on the x-axis and their positions are taken to vary with x, including through the focal point of the lasers.

4.3 Numerical results for a single Raman-active sphere

4.3.1 Single Raman-active sphere on resonance

In order to study the effects of object/background refractive index mismatch on SRS and CARS images, we first look at the magnitude of the electric field at the pump frequency, ω_p, around and within a single spherical object as it moves through the focal point of the tightly focused pump laser source. The left plots of Fig. 16 show the undistorted pump field in the x-y plane for a single sphere with the same index of refraction as the homogeneous background medium with $n = 1.33$. The plots on the right show the field strengths when the sphere has a larger refractive index of $n = 1.5$. The difference in the refractive index between the sphere and the medium is modest, but distortions to the fields are clearly visible: The focal point is shifted and additionally the field strength is increased up to 53%. A ring can be seen in the top right and is similar to those found by Ferrand et al. [122]. The near-field plots for the Stokes beam are similar (not shown). Though we only show the pump beam here, in our FDTD simulations both the pump and Stokes beams are included. Since the polarization in Eqs. (106)–(108) scale as the cube of the pump/Stokes field, the maximum measured signal, *i.e.* the intensity, can potentially increase by a factor of 13. However, for that scenario the input fields would have to be enhanced uniformly everywhere inside the sphere, which is clearly not the case. From the top left and top right pump field plots in Fig. 16, we note that there is very little field enhancement inside of the sphere therefore only small effects on SRS and CARS images are expected. However, there is a strong focused spot in the background medium caused by the object which acts as a microlens.

In Fig. 17, we plot the simulated far-field intensity of the CARS/FM-CARS and AM-/FM-SRS signals generated from a $r = 1.24\,\mu\text{m}$ sphere with and without linear index mismatch to the background, as the object is moved through the laser focus along the laser propagation axis (x-axis). In all cases, we find that signal strength remains almost unchanged. However, the measured position of the sphere is shifted towards the collecting lens by $0.4\,\mu\text{m}$ for CARS and FM-CARS and by $1.0\,\mu\text{m}$ for AM-SRS and FM-SRS. From earlier work [69], we determined that the refractive index mismatch affects the perceived position of the object in CARS and FM-CARS for a $r = 0.4\,\mu\text{m}$ sphere, but there the dominant effect was due to interference with the NRB and the Gouy phase shift at the position of the object, leading to an order of magnitude larger shift than that caused by refractive index mismatch. Here the sphere is much larger so the effect

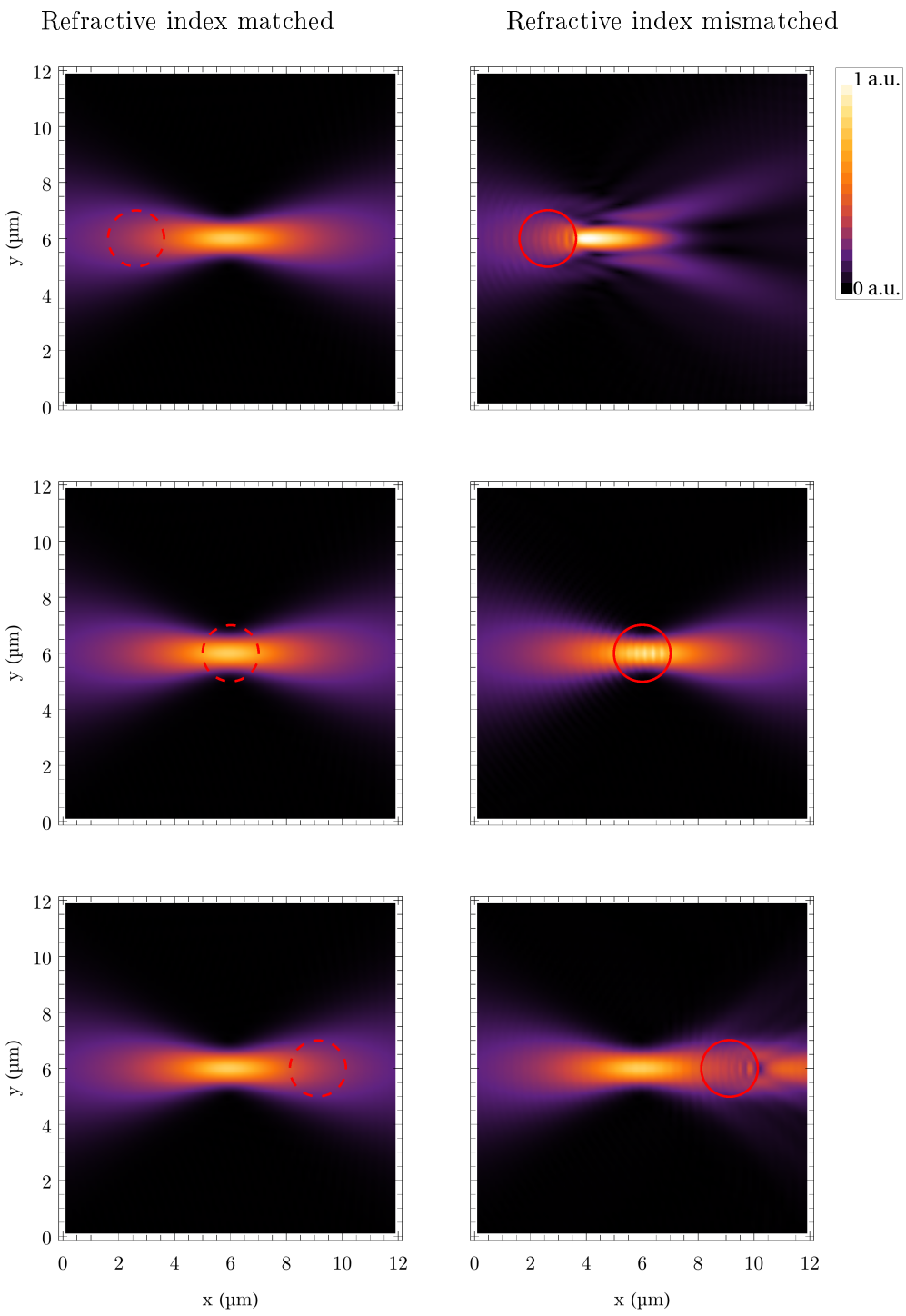

Figure 16: The field magnitude of the pump beam in a $n = 1.33$ medium focused at $x = 6.0\,\mu\text{m}$ is shown in the presence of a homogeneous refractive index (left) and for the case where it is distorted by the presence of a $r = 1.0\,\mu\text{m}$ sphere with $n = 1.5$ (right). The position of the sphere is indicated by the (red) circles, where a dotted line means the sphere is refractive index-matched, and a solid line means it is index mismatched.

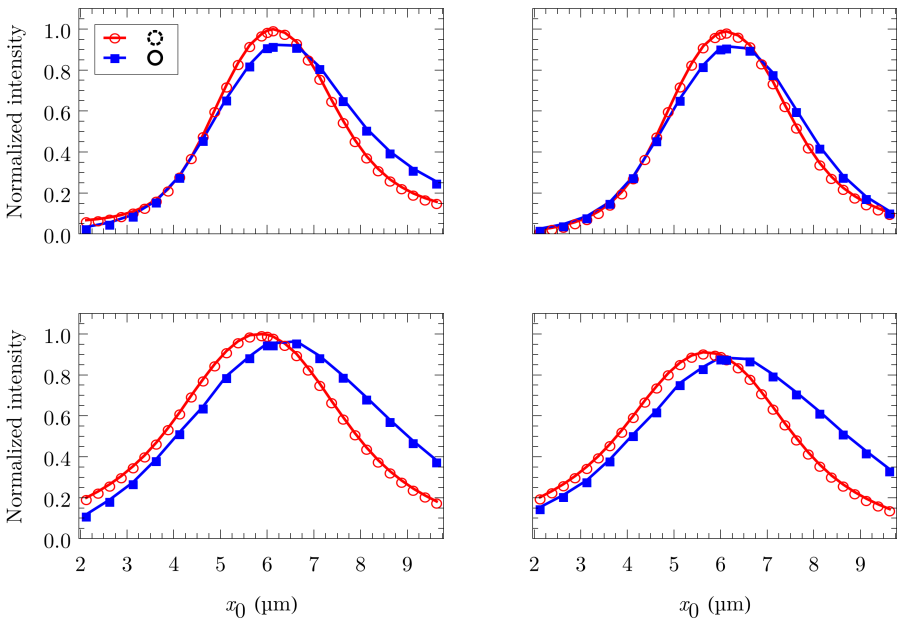

Figure 17: CARS (top left), FM-CARS (top right), AM-SRS (bottom left) and FM-SRS (bottom right) far-field signals as a function of bead positions, x, along the laser propagation axis of a single $r = 1.24\,\mu\text{m}$ sphere with (blue filled squares) and without (red open circles) a linear index mismatch with the background medium ($n = 1.33$). In all cases, the laser focal spot is at $x = 6.0\,\mu\text{m}$.

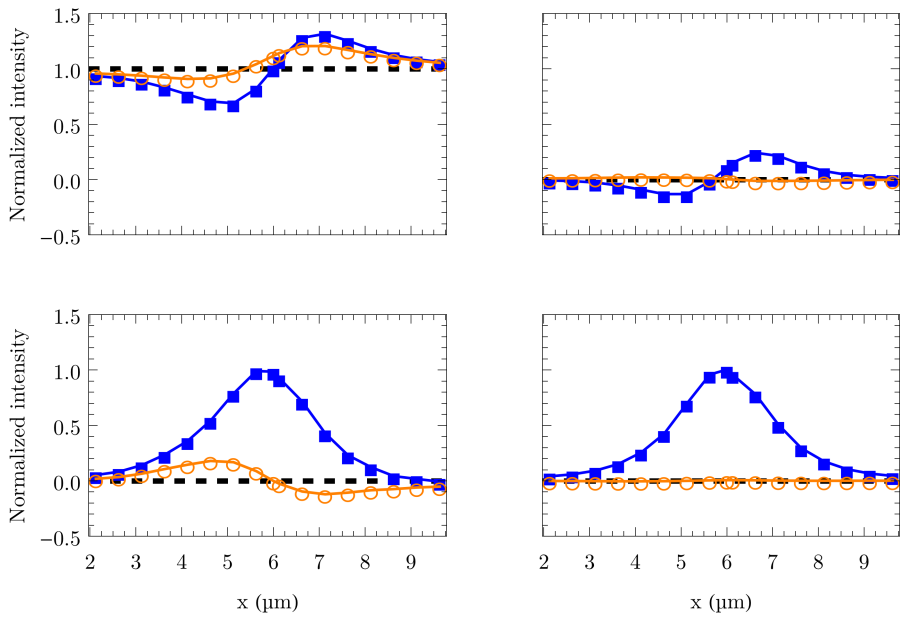

Figure 18: Far-field signals for anti-Stokes (top left), FM anti-Stokes (top right), AM pump (bottom left) and FM pump (bottom right) as a function of bead position x. This is for a single $r = 0.25\,\mu\text{m}$ sphere ($n = 1.5$) index mismatched with a background medium ($n = 1.33$) and a collecting lens NA of 0.6. The solid blue squares are for a resonant sphere and the orange open circles are for a nonresonant one. The top plots are expressed in units of the far-field NRB signal from bulk. The index-matched off-resonant signal, *i.e.* the NRB, is indicated by the black dashed line. The bottom plots have been scaled such that the peak value of the solid line for each sphere is one. In all cases, the laser focal spot is at $x = 6.0\,\mu\text{m}$.

of the NRB is much smaller in comparison as can be deduced from the signal strength of CARS and FM-CARS being nearly the same. As the NRB plays only a very small role for CARS and FM-CARS, and does not exist for AM-SRS and FM-SRS, the deviation in the measured position arises exclusively from the refractive index mismatch.

4.3.2 Single Raman-active sphere off resonance

Next we investigate the effect of near-field enhancements of the pump and Stokes field on the off-resonant SRS and CARS for a single sphere of radius $r = 0.25\,\mu\text{m}$. The nonresonant susceptibility, $\chi^{(3)}_{NR}$, is taken to be the same for the sphere and the background and $\chi^{(3)}_{R}$ is either nonzero for the on-resonant case or zero for the off-resonant case. We measure the far-field signal at the SRS and CARS frequencies for those two

cases, the results of which are shown in Fig. 18. In the CARS measurements (Fig. 18 top left), a large signal above the NRB baseline for a homogeneous nonlinear susceptibility is detected despite the lack of resonant material. Turning off the linear index mismatch leads to a flat uniform NRB (thick black dashed line) as expected. The strength of the off-resonant signal (orange open circles) is about half of that of the on-resonant case (filled blue squares). The fact that this occurs with a homogeneous $\chi^{(3)}_{NR}$ shows that the patterns in the nonresonant background commonly seen in CARS measurements are not only the result of an inhomogeneous nonlinear susceptibility, but can also be caused by an inhomogeneous index of refraction. FM-CARS reduces these off-resonant signals, but a small signal remains (Fig. 18 top right). As expected the CARS and FM-CARS signal of the on-resonant sphere are not centred at the focal point of the laser source [69]. There is however also a shift in the off-resonant signals, which cannot be caused by interference as there is no resonant signal to interfere with. It is instead caused by the refractive index mismatch that causes an enhancement in front of the sphere due to microlensing. Therefore, the strongest nonresonant signal does not occur when the sphere is exactly in the focal point of the laser, but when the sphere is in front of the focal point.

In Fig. 18 (bottom left), we also observe a clear signal in off-resonant AM-SRS where we would expect no signal at all. Like for CARS, it is induced by inhomogeneous $\chi^{(1)}$ due to microlensing. In previous work [70], we showed that an inhomogeneous nonlinear susceptibility generated a background signal in off-resonant AM-SRS. This was due to the fact that the different beam intensities between the Stokes beam being on and off caused a difference in the induced refractive index through the Kerr effect via $n = n_0 + n_2 I$ in combination with the inhomogeneous n_2. This in turn led to an NA-dependent difference in the collected signal in such a way that increasing the NA of the collecting lens decreases the nonresonant signal. Here we have a homogeneous $\chi^{(3)}$ everywhere and we find that the nonzero off-resonant signal is caused by the refractive index mismatch between the sphere and the background medium. Additionally, the off-resonant signal now depends on the position of the sphere because the near-field enhancements depend on object position.

4.4 Numerical results for double spheres

The situation is very different in the case of multiple spheres as is evident from the near-field plots at the pump frequency for two touching $r = 1.0\,\mu\text{m}$ spheres shown in Fig. 19. The plots show two spheres in a background medium illuminated by a tightly

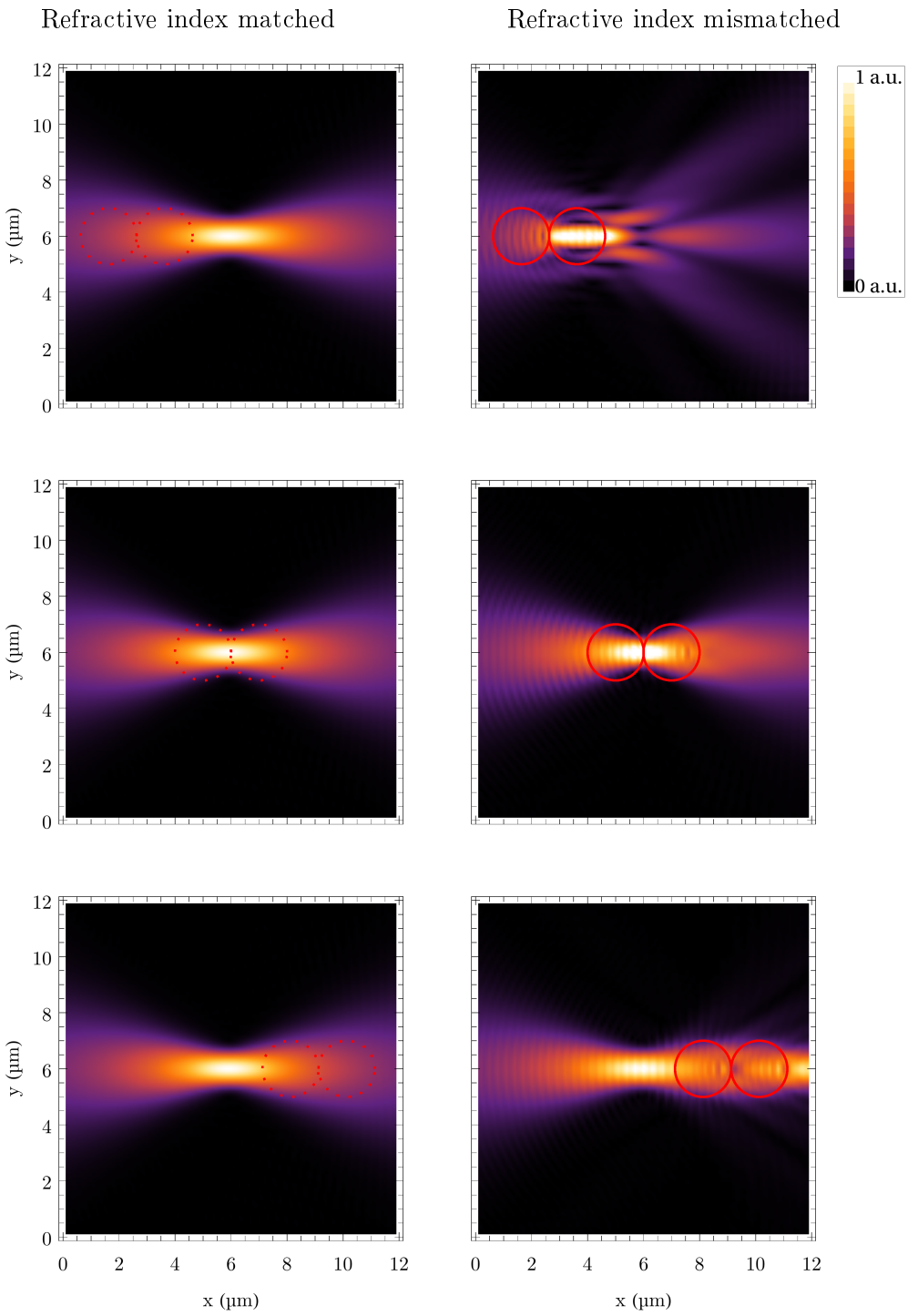

Figure 19: The field magnitude of the pump beam in a $n = 1.33$ medium focused at $x = 6.0\,\mu\text{m}$ is shown in the presence of a homogeneous refractive index, configuration I, (left) and for the case of two $r = 1.0\,\mu\text{m}$ spheres, configuration II (right). The position of the sphere is indicated by the (red) circles, where a dotted line means the sphere is refractive index-matched, and a solid line means it is index mismatched. The field magnitudes for a single index-mismatched sphere, configuration III, are similar to those plotted on the right side of Fig. 16.

focused laser beam. In the left plots, the spheres have the same refractive index as the background while in the plots on the right, the spheres are index-mismatched. In the latter, the sphere closest to the laser source acts as a microlens, resulting in an enhancement of the pump field strength up to 51%. Even though the enhancement is slightly less than for the single sphere, the location of the maximum enhancement is now inside the second sphere. As a result, the nonlinear induced polarization in the sphere closest to the collecting lens increases significantly and becomes the dominant source for the measured SRS and CARS signal. As the spheres decrease in size, the enhancement effects also decrease. However, they remain significant. We find that there is always an enhancement inside the second sphere due to the microlensing effect for spheres with radii as small as $r = 0.2\,\mu\text{m}$, where an enhancement of up to 26% in pump field strength can be observed.

To gain deeper insight into the effects of object shape on SRS and CARS far-field measurements, we compare the far-field signal for three configurations that have the same volume of Raman-active medium and thus the same total number of scatterers. The first configuration I is two touching spheres that have the same refractive index as the background medium ($n = 1.33$). The second configuration II has the same shape as the first, but the refractive index of the spheres ($n = 1.5$) does not match the background medium. Finally, we consider configuration III, which is a single larger index-mismatched sphere with a volume equal to the combined volume of the two spheres in I or II. The near-fields look similar to those depicted on the right side of Fig. 16. Since each configuration has the same total volume, one would expect roughly the same signal strength from each. When interpreting SRS and CARS images, it is commonly assumed that the measured signal scales linearly (for SRS) or quadratically (for CARS) with density. However, our simulations show that this need not be the case.

First we consider the effect of the refractive index mismatch by comparing configurations I and II, which have identical shapes. In Fig. 20, we plot the far-field intensity for two $r = 1.0\,\mu\text{m}$ spheres as they are moved along the propagation axis for configurations I and II. The differences between the far-field intensities are substantial. First, the magnitude of the signal for configuration II (filled blue squares) has nearly doubled for every vibrational technique compared to the index-matched case I (open red circles). Because the induced nonlinear polarization is a third-order process, the field enhancements inside of the second sphere cause the induced nonlinear polarization to be greatly enhanced which creates a significantly larger signal. Second, the perceived position of the object

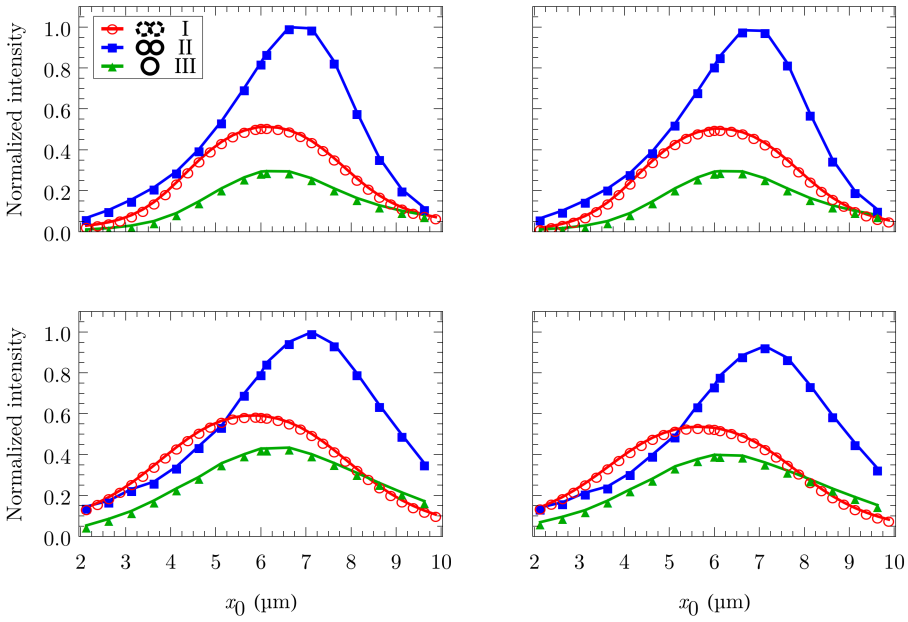

Figure 20: CARS (top left), FM-CARS (top right), AM-SRS (bottom left) and FM-SRS (bottom right) far-field signals as a function of position along the laser propagation axis of two touching $r = 1.0\,\mu\text{m}$ spheres with (blue filled squares) and without (red open circles) a linear index mismatch. The green filled triangles are the signal for a single index-mismatched sphere of $r = 1.25\,\mu\text{m}$. The single sphere has the same volume as the two $r = 1.0\,\mu\text{m}$ spheres combined.

in the image created by the index-mismatched spheres II is shifted towards the collecting lens by almost a micrometer. This is because the induced polarization in the second sphere is much larger than that of the first causing the total signal of the configuration to shift in the direction of the second sphere.

To determine the effect of the distribution of scatterers, *i.e.* object shape, we next consider the far-field intensity of configuration II versus III, which have the same refractive index-mismatch with the background medium. In Fig. 20, we see that for each technique the signal enhancement effect is even more pronounced with an intensity enhancement of up to a factor of four for the double spheres (filled blue squares) versus the same volume single sphere (filled green triangles). This is partly because the single index-mismatched sphere does not contain an enhanced field within it, whereas the two spheres in configuration II do. Additionally, because the focal spot is wider along the propagation direction than it is in the perpendicular direction, the scatterers shaped as two touching spheres experience a higher field strength on average than a single large sphere. This indicates that far-field signal strength does not directly correlate with scatterer density as is commonly assumed, but is highly dependent on object shape.

We perform the simulations for configurations I, II, and III for a range of radii from 0.4 µm to 2.0 µm, and extract the largest far-field signal for each configuration and radius. We do this for each vibrational technique as well as for collecting lens NA's of 0.1, 0.3, and 0.6. The ratios of these peak values provide an enhancement factor which quantifies the effects of shape and refractive index mismatch. In Fig. 21, we plot the ratio of the signal strength for configuration II to I, which shows the enhancement due to refractive index-mismatch between the objects and the background medium. When using a collecting lens of NA = 0.1 (left plot), a factor of up to six in far-field signal strength is measured for all of the techniques. For larger collection NA's (middle and right plot) the enhancement is reduced, but still can be over a factor of two depending on the size of the spheres. There is a small difference between CARS and SRS signal enhancement which is due to the fact that the polarization for SRS in Eq. (107) scales with $E(\omega_p)|E(\omega_S)|^2$ while for CARS it scales with $E^2(\omega_p)E^\star(\omega_S)$. The difference in wave length of the pump and Stokes field causes the near-field enhancements to be different.

In Fig. 22 we show the ratio of the peak far-field intensity strength of configuration III to II, where all objects have an index of refraction that is different from the background medium. A factor of up to seven in signal strength is measured between the double and single sphere for AM-SRS and FM-SRS. For CARS and FM-CARS, the enhancement

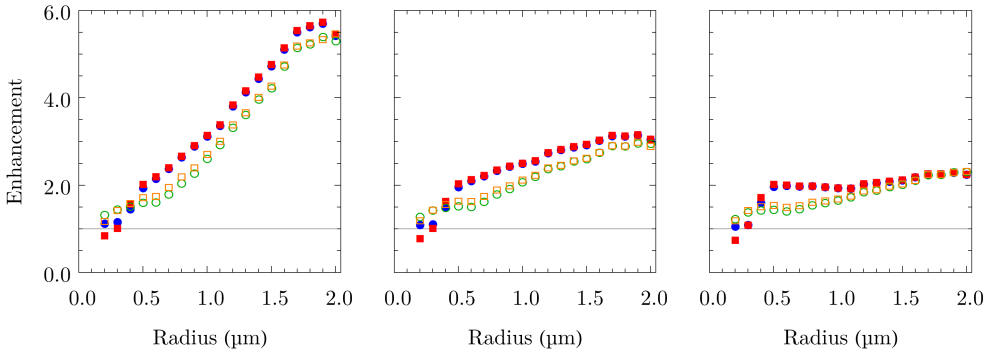

Figure 21: Far-field enhancement factor calculated as the ratio between the far-field signal intensity from two index-mismatched touching spheres of configuration II to that of two index-matched ones of configuration I. Blue filled circles are CARS, red filled squares are FM-CARS, green empty circles are AM-SRS, and orange empty squares are FM-SRS. That is, the top two lines are CARS/FM-CARS and the bottom two are AM-SRS/FM-SRS. From left to right a collection lens NA of 0.1, 0.3, and 0.6 is used.

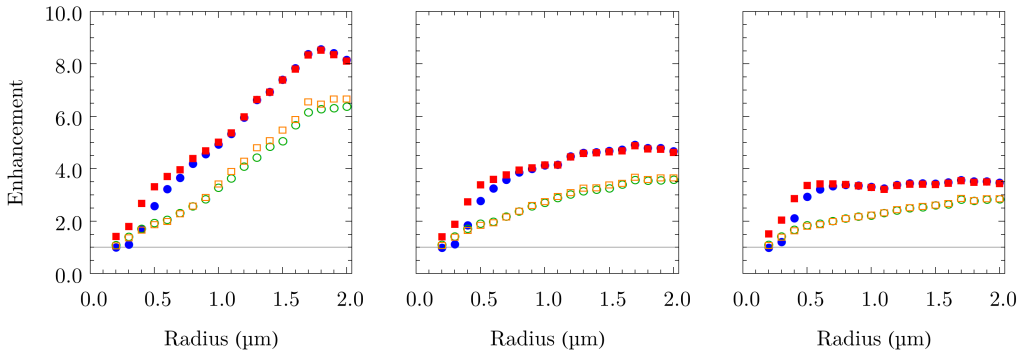

Figure 22: Far-field enhancement factor calculated as the ratio between the far-field signal intensity from two touching spheres of configuration II to that of a single sphere with equivalent volume of configuration III. Blue filled circles are CARS, red filled squares are FM-CARS, green empty circles are AM-SRS, and orange empty squares are FM-SRS. That is, the top two lines are CARS/FM-CARS and the bottom two are AM-SRS/FM-SRS. From left to right a collection lens NA of 0.1, 0.3, and 0.6 is used.

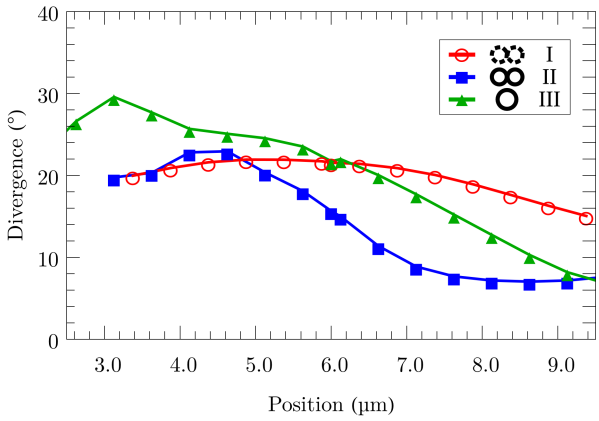

Figure 23: Comparison of the far-field CARS intensity signals for $r = 1.5\,\mu\text{m}$ index-matched double spheres (red open circles) of configuration I, index-mismatched double spheres (blue filled squares) of configuration II, and single index-mismatched sphere of double volume (green filled triangles) of configuration III. Plotted is the divergence of the signal on the collecting lens. The divergence is taken as the width of a Gaussian function in units of angle fitted to the far-field intensity distribution.

is up to a factor of nine. The SRS enhancements are similar for both AM-SRS and FM-SRS, but the CARS enhancements differ between CARS and FM-CARS for small radii. That difference is due to the NRB. When the spheres are small, the CARS signal is dominated by the NRB for configurations II and III. For larger spheres, the CARS signal becomes more dominant than the NRB, which is why the CARS and FM-CARS enhancements plots in Figs. 21 and 22 converge to the FM-CARS enhancements where the NRB is largely filtered out. The difference between the SRS and CARS signal is larger compared to that in Fig. 21. The shape determines the areas where the far-field signal is generated by the induced nonlinear polarization. As the focal spot size of the incoming pump and Stokes laser sources is different, due to the different wavelengths, the SRS and CARS far-field signals will be even more affected through the different dependence on the Stokes and pump field illustrated earlier in Eqs. (107) and (108).

The large far-field signal enhancements due to the structure of the refractive index (Fig. 22), or due to the complex shape (Fig. 21) make it appear as if there is more of the molecule of interest present than is actually there. For a collecting lens NA of 0.6, the enhancements are clamped to a factor of two to four. However, this is still an appreciable amount, especially when considering the modest mismatch in refractive index between the spheres and the background medium. The reason that the far-field

intensity enhancement depends on the NA is that the radial intensity pattern of the SRS and CARS far-field signals is wider in cases I and III than it is for case II. This can be seen in Fig. 23 where we plot the width of the far-field CARS intensity radiation pattern of configurations I, II and III as a function of object position along the laser propagation axis. The radiation pattern for two index-mismatched spheres II is narrower due to the microlensing of the second sphere. While the effect of this lensing on the image can be reduced by capturing as much of the radiation pattern as possible, signal enhancement effects cannot be reduced further by increasing the NA of the collecting lens. This is because the effects due to near-field enhancements cannot be eliminated. The total irradiated power is itself increased and the enhancements are not just a diffraction effect.

The far-field SRS and CARS signal enhancements also occur when the spheres are no longer touching. They fall off very slowly as a function of distance between the spheres. In Fig. 24, we show the enhancement of SRS and CARS as a function of distance, as well as the FM-SRS signal for various separations as a function of object position along the laser propagation axis for two $r = 0.5\,\mu\text{m}$ spheres (top) and two $r = 1.0\,\mu\text{m}$ spheres (bottom). For an edge-to-edge distance between $2.0\,\mu\text{m}$ of the two spheres, the far-field enhancement effect in the left plots is still very noticeable. A factor of two in signal enhancement for SRS and a factor of more than three for CARS is observed for both the $r = 0.5\,\mu\text{m}$ and $r = 1.0\,\mu\text{m}$ spheres. The microlensing of the first sphere makes the pump beam field more narrow and enhanced over a long range as can be seen, for example, in the first two plots of the pump beam enhancement for a single sphere in Fig. 16. Thus the spheres need not be touching for a significant modification of SRS/CARS imagery. For the same reason, we see in the lower right plot of Fig. 24 that the far-field FM-SRS signal of the second $r = 1.0\,\mu\text{m}$ sphere completely masks that of the first to such an extent that the first sphere is invisible in the far-field signal for all separation distances considered. Even for the $r = 0.5\,\mu\text{m}$ spheres (top right), the second sphere only becomes distinguishable from the first when they are more than two sphere radii apart, even though the spot size of induced third-order polarization is significantly smaller than that. More complicated structures with multiple differently shaped objects with different refractive indices in the sample will have more complicated effects on the SRS and CARS signal.

4.5 Conclusion

We have shown that the near-field enhancements due to the refractive index mismatch can play a large role in SRS and CARS images. Objects act as internal microlenses.

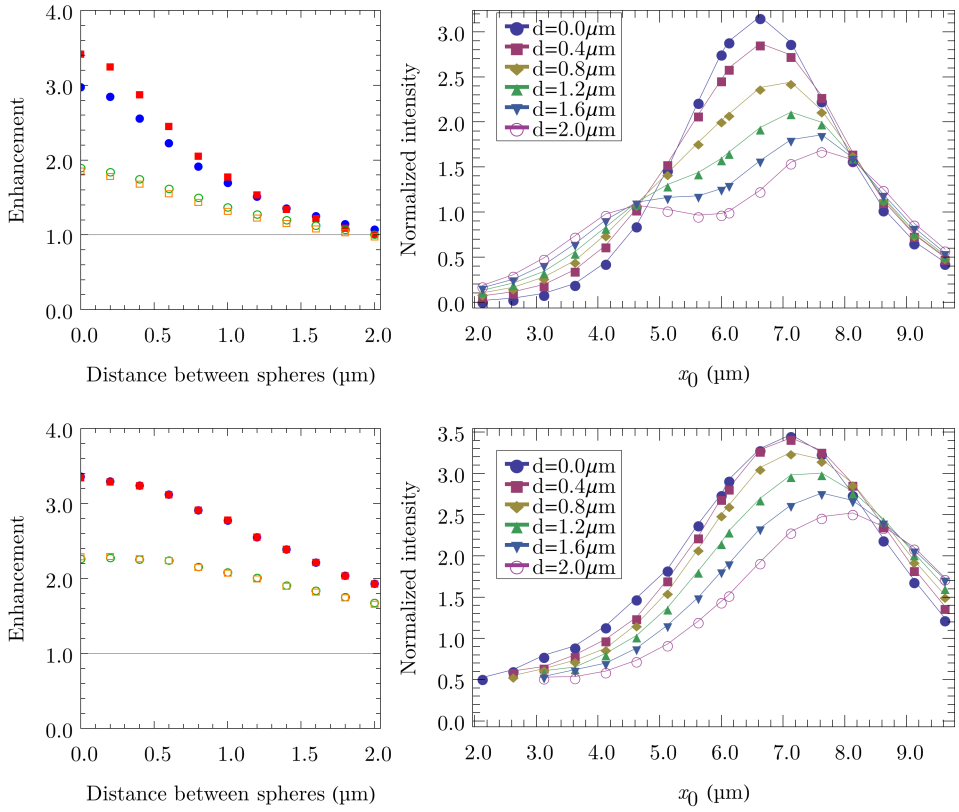

Figure 24: Left: Enhancement (the ratio of the maximum far-field signal intensity for two separated spheres and a single sphere with the same total volume) versus edge-to-edge separation distance of the two spheres. Top left is for two $r = 0.5\,\mu\text{m}$ spheres and one $r = 0.63\,\mu\text{m}$ sphere. Bottom left is for two $r = 1.0\,\mu\text{m}$ spheres and one $r = 1.25\,\mu\text{m}$ sphere. The signal was collected with a collection lens with an NA of 0.6. Blue filled circles are CARS, red filled squares are FM-CARS, green empty circles are AM-SRS, and orange empty squares are FM-SRS. That is, the top two lines are CARS/FM-CARS and the bottom two are AM-SRS/FM-SRS. Right: FM-SRS far-field intensity for two $r = 0.5\,\mu\text{m}$ spheres (top) and two $r = 1.0\,\mu\text{m}$ spheres (bottom) as a function of position along the laser propagation axis. Different curves represent different sphere separation distances as indicated in the legends. Intensity was normalized to that of a single sphere.

Due to the third-order nature of the nonlinear SRS and CARS processes, these field enhancements are cubed in the polarization term, which causes large distortions in the far-field.

Even for the modest differences in the refractive index, such as those occurring in biological material, far field signal enhancements of an order of magnitude can occur and objects can appear shifted on the order of micrometers, even using FM techniques. These results break the assumption that far-field intensity scales linearly with the number of scatterers for SRS or quadratically for CARS.

Further, linear index mismatch on its own can cause significant non-uniform off-resonant CARS and AM-SRS signals. The latter is especially noteworthy as AM-SRS should be background free. These off-resonant signals were greatly reduced in FM-CARS and FM-SRS, indicating the importance of using frequency-based filtering methods, such as hyperspectral analysis or FM techniques.

The objects studied in this paper are simple examples of inhomogeneous samples. In nature, an inhomogeneous sample will have a much more complicated structure, both in shape and refractive index profile, which can result in a complex pattern of near-field enhancements. This in turn would introduce complicated distortions into the SRS and CARS signal. No technique can remove all of these effects. Therefore the only way to account for them when studying SRS and CARS imagery, is to be aware of the range of the value for the refractive index throughout the sample and the length scale at which it changes. We have shown here that $n = 1.5$ objects embedded in a $n = 1.33$ background can lead to an order of magnitude higher far field signal; a larger mismatch would be expected to give even more significant enhancement.

5

Ptychography for nonlinear optical microscopy: retrieving phase without interferometry

This chapter is a verbatim copy of the article that has been submitted to *Biomedical Optics Express*[2] with the addition of section labels for ease of navigating this thesis. Additionally, the ptychographic algorithm for nonlinear optical microscopy is explained in more detail in appendix 5.A at the end of this chapter. I gave an invited talk at the 2017 OSA Biophotonics conference about this work as well as an oral presentation at the 2017 CLEO and Photonics North conferences.

5.1 Introduction

Ptychography is an iterative computational technique for imaging that can reconstruct both the complex-valued transmission function of an illuminated object as well as the

[2]J.N. van der Kolk and L. Ramunno, *Ptychography for nonlinear optical microscopy: retrieving phase without interferometry*, Biomedical Optics Express, submitted

near-field magnitude and phase of the illuminating beam [91, 124, 125]. The scattered light from the object is captured on a CCD directly with or without a collecting lens. By using multiple, overlapping far-field intensity patterns generated from random points within the sample, the algorithm reconstructs the transmission function from the overlapping measurements and can achieve a resolution much smaller than the spot size of the input beam. Detailed information about the input beam is not necessary, as it is also reconstructed, which allows for low quality and imperfect light sources.

Ptychography was originally developed for imaging crystalline objects with electron microscopy in 1969 [126, 127]. Due to insufficient detector quality it was not until 1994 that the technique could be applied experimentally [128]. The breakthrough algorithm, ptychographical iterative engine (PIE), was introduced in 2004 where multiple far-field diffraction images from different beam positions — instead of a single wide-field image — were used to reconstruct both the phase and magnitude of the transmission function. Proof of concept was shown for visible light [124, 129]. Extended PIE (ePIE) further allowed for the reconstruction of the complex-valued near-fields of the input beam, thus enabling ePIE to correct for beam distortions [125]. For X-ray and electron microscopes, PIE/ePIE allows one to do away with expensive optics as no collecting lens is needed. The technique was also used with visible light as phase-imaging provides enhanced contrast [124, 130].

Ptychography found broad application in X-ray imaging, *e.g.* cell imaging [131–133], and has been used to achieve 16 nm resolution in 3D [134], and 5 nm in 2D [135]. The ePIE algorithm has allowed atomic resolution in electron microscopy, shown as proof of concept for carbon films with 2-5 nm gold particles [136] and boron nitride cones [137].

In brief, linear ePIE works as follows. First, a number of far-field diffractive images are recorded by a CCD camera while an input beam (probe) illuminates a sample (object), at different positions. An initial guess is made for the object's complex-valued transmission function, as well as for the electromagnetic field of the probe in the plane of the sample. The product of these is the exit-field and represents the electromagnetic field just after the sample. Using a Fourier transform, the exit-field is transformed to the far-field, the phase of which is multiplied with the measured far-field intensity to obtain a fully complex electric field. This is transformed back to the near-field and compared to the original exit-field. The guessed object and probe are updated to new guesses and the procedure repeats for each measurement multiple times until convergence is reached.

In this paper, we develop ptychography for application to nonlinear optical microscopy

based on ePIE. Nonlinear optical microscopy offers several advantages, including allowing for label-free imaging and providing contrast in biological samples where the refractive index is nearly homogeneous. We present a general framework for nonlinear ptychography and focus on two numerical examples: retrieving the phase of $\chi^{(2)}$ of collagen fibrils in tendon with second harmonic generation (SHG); and retrieving the phase of the coherent anti-Stokes Raman scattering (CARS) signal of fibroblast cells that we use to separate resonant and nonresonant contributions.

5.2 Methods

We find enhanced resolution similar to linear ptychography. Though focused beams generally used in nonlinear optical microscopy have small spot sizes, and therefore produce high resolution images, we find that nonlinear ptychography can increase the resolution further, up to the diffraction limit of the nonlinear frequency. More importantly, it gives access to the phase of the nonlinear susceptibility without the need for interferometry. Finally, we demonstrate that disturbances in the input beam(s) can be reconstructed.

The PIE/ePIE algorithms were developed for reconstructing transmission functions, which in the absence of scatterers have a value of one. Here the object we wish to reconstruct is the nonlinear optical susceptibility, which is zero in the absence of nonlinear scatterers. We take the exit-field to be the induced nonlinear polarization in the sample, P, which for arbitrary nonlinear processes is $P \propto \chi^{(n)} E_1 E_2 \cdots E_n$, where $\chi^{(n)}$ is the n-th order nonlinear susceptibility tensor, and E_i is the electric field vector of the i-th input beam. Considering the exit-field to be the product of object and probe, we see from the expression for P that we can choose the probe to be the product of the electric field components of the input beams. When multiple input beams are involved we lose the ability to reconstruct individual input beams, however the product of those fields does get reconstructed and therefore the ability to correct for distortions in any of the input beams is preserved. Finally, the far-field image is obtained through a Fourier transform of P, where those far-field images can be at a different frequency than that of the input beam(s).

In our hypothetical experimental set-up, we consider an input beam or beams incident from the left, propagating in the z-direction and polarized in the y-direction, that illuminates a 2D sample oriented in the xy-plane. This results in a nonlinear signal being generated which is focused by a collecting lens in the far-field onto a CCD camera. We consider a high-NA collecting lens as is typical in nonlinear optical microscopy. Here

we use an NA of 1.0 as an example. The far-field image is determined at $z_{far} = 1\,\text{mm}$ such that $z_{far} \gg \lambda, w_0$, where λ and w_0 are the wavelength and waist size of the input beam(s), respectively. The pixel count of the CCD determines that of the reconstructed image, which we take as 1024×1024.

The sample is probed at M different random locations such that the waists of neighbouring probe beams overlap by 30 % and then the resulting nonlinear optical microscopy far-field images are calculated. With these M images, the nonlinear iterative ptychography algorithm is executed. The first step is to make a guess for both the object, *i.e.* the n-th-order nonlinear susceptibility $\chi^{(n)}(x, y)$, and the probe, *i.e.* the product of the electric fields of each of the input beams at the sample surface, $E_i(x, y)$. The coordinates x and y range over the entire area to be imaged. We use random complex-valued noise as the guess for the object, but for the initial input beams we use Gaussian functions. We iterate over the M images N times to get ever closer to the original object and probe. We show that not only do we have improved resolution over traditional nonlinear optical imaging, we have the phase information as well.

5.3 Results for second harmonic generation

As our first example, we apply the nonlinear ptychographic reconstruction algorithm to the SHG imaging of a 2D sample. Since the induced nonlinear polarization scales as $P \propto \chi^{(2)} E^2$, we use $\chi^{(2)}$ as our object and E^2 as our probe. SHG is often used for studying collagen fibrils, which can be found in a wide array of tissues such as bones, tendons, arteries, and cornea, and are responsible for most of their mechanical properties [38]. Moreover, diseases such as osteoarthritis have changes in collagen tissue as one of the earliest pre-symptomatic indicators [138].

Fibrils in tendon generally align in a parallel fashion where individual fibrils have either positive or negative chirality resulting in a sign of $\chi^{(2)}$ that is either positive or negative [112]. Using interferometric SHG (I-SHG) one can probe the orientation and structure of collagen fibrils via the phase of $\chi^{(2)}$ [2, 107]. We show that we can use ptychography in place of interferometry to probe fibrillar orientation and structure.

For our numerically generated sample, the fibrils are randomly placed in a non-overlapping manner and are all parallel in the y-direction. Their diameters are randomly generated using the distribution for tail tendons from 13–14 week old rats where the mean fibrillar diameter is 130 nm, but individual fibrils can be as large as 400 nm [106]. The yyy component of the $\chi^{(2)}$ tensor is either positive or negative and we consider here

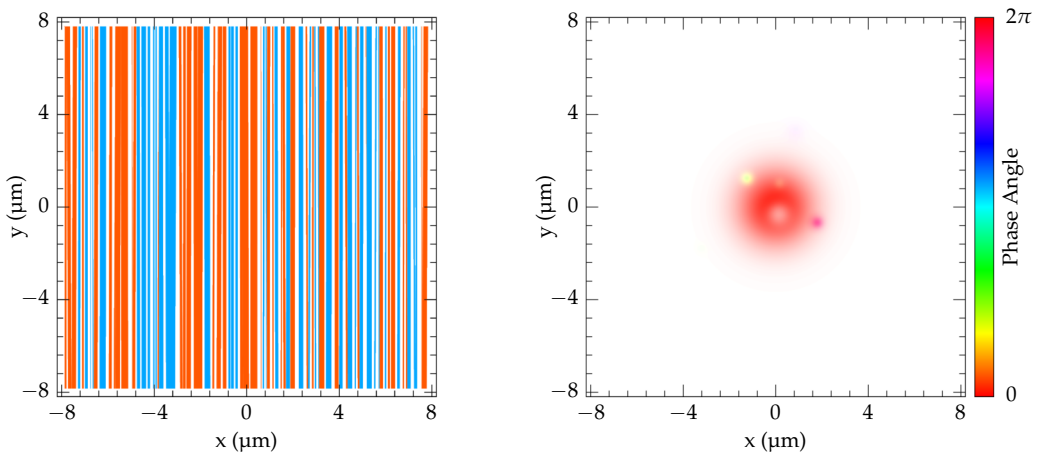

Figure 25: The phase of $\chi^{(2)}$ for the real object (left) and phase of E^2 for the real probe (right). The phase is indicated by the colour, where white indicates zero amplitude.

that this occurs randomly in a 1:1 ratio. The other components are disregarded as we only consider a y-polarized input beam and the $\chi^{(2)}$ component along the fibril length is the largest. The sample is restricted to a 2D object of 16 µm by 16 µm. Our sample is consistent with that imaged with the I-SHG technique by Rivard et. al [107], where they studied the structural organization of fibrils in rat tail tendon and found that an overall orientation of the noncentrosymmetric structures persists over tens of microns.

To simulate a systematic fault in the optics system we added distortions to the Gaussian input beam(s) by adding smaller Gaussian bumps at random locations with random widths, phases, and amplitudes up to 25 % of the maximum. The central wavelength is 810 nm and thus the SHG radiation is at 405 nm.

In Fig. 25, the phase of the actual object, that is, the phase of the nanoscopic $\chi^{(2)}$ of our generated 2D rat tail tendon sample, is shown on the left; white indicates zero amplitude, where the phase would be undefined. The right shows the phase of the actual probe including defects. These defects can have a different phase than that of the main beam which is why there is a small amount of destructive interference near the centre. We have used a beam waist of 2.20 µm.

We create far-field intensity patterns, or "measurements", of the sample from $M = 60$ different probe beam positions, by calculating the induced nonlinear polarization in the sample, propagating the SHG signal to the far-field using a Fourier transform, and collecting the far-field images. We use $N = 200$ iterations for the ptychography algorithm where probe reconstruction was turned on after 100 iterations, which leads to

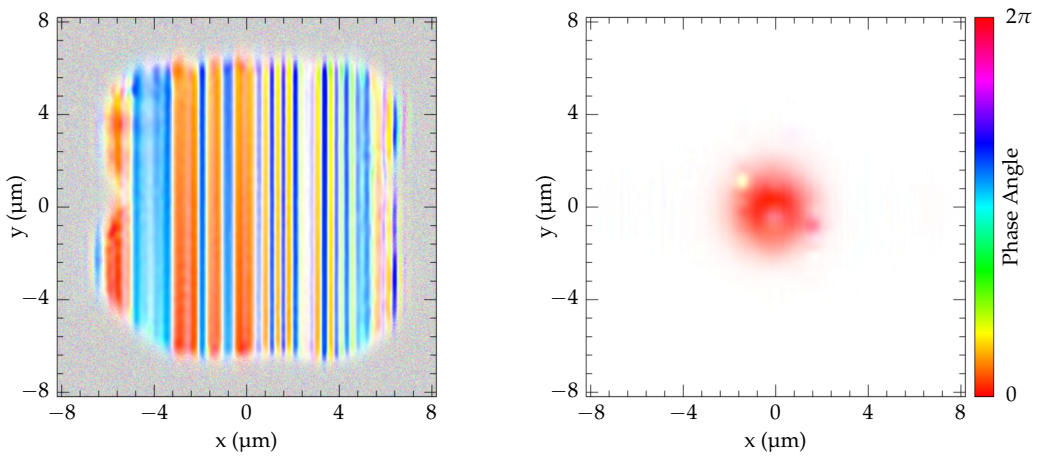

Figure 26: The reconstruction of Fig. 25.

a reconstructed object and probe whose phases are shown in Fig. 26. More measurements can be used to improve the quality of the reconstruction up to the diffraction limit of the SHG frequency. The reconstruction is able to resolve most fibrils completely, and includes the phase information which corresponds very closely to that of the real object in Fig. 25. At $x = 3.0\,\mu\text{m}$, no material appears to be present as neighbouring fibrils have opposite sign and therefore the SHG signals interfere destructively in the far-field. The defects in the probe have also been reconstructed. The blurry edges in Fig. 26 are areas where the input beam has not scanned and thus remain the random initial guess for $\chi^{(2)}$ because there is not enough information for reconstruction.

Fig. 27 shows a cut of the phase of $\chi^{(2)}$ along the y-axis, with the corresponding amplitude in Fig. 28, for both the original object (blue) as well as for several reconstructed objects where the input beams used for the imaging have differing beam waist radii, namely: $0.55\,\mu\text{m}$ (red), $1.10\,\mu\text{m}$ (green), and $2.20\,\mu\text{m}$ (orange). We used $M = 960$ for $w_0 = 0.55\,\mu\text{m}$ and $M = 240$ for $w_0 = 1.10\,\mu\text{m}$ to keep the total scanned area the same, which makes the algorithm computationally more expensive than for larger beam waists. Fig. 27 shows that fibrils as small as 200 nm can be individually resolved via their phase, corresponding to the diffraction limit at the SHG wavelength of 405 nm. If multiple smaller fibrils are close together and have the same $\chi^{(2)}$ phase, the overall phase is still reconstructed. This occurs for example between $x = -3.0\,\mu\text{m}$ to $-2.0\,\mu\text{m}$. If multiple small neighbouring fibrils have opposite $\chi^{(2)}$ phase, their far-field signals cancel as is seen between $x = 2.5\,\mu\text{m}$ to $3.0\,\mu\text{m}$.

The amplitudes are plotted in Fig. 28. Fibrils of a diameter of 200 nm are again able

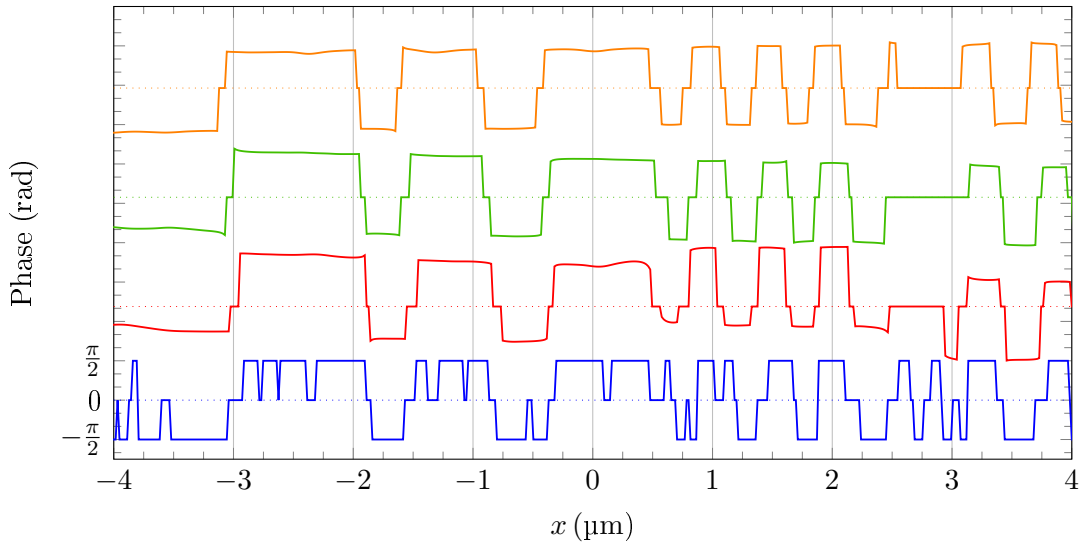

Figure 27: Phase of $\chi^{(2)}$ at $y = 0$ for the object in Fig. 25 (blue) and those reconstructed with input beams with waist sizes of 0.55 µm (red), 1.10 µm (green), and 2.20 µm (orange). The plots have been vertically translated; dotted lines indicate 0 phase lines. Phase for very small $\chi^{(2)}$ has been set to zero.

to be resolved, though without the sharp edges of the phase reconstructions in Fig. 27. We compare the reconstructions to a hypothetical SHG imaging experiment where the sample is moved on a translation stage. For each scanned point, we calculate the far-field intensity value by integrating the far-field intensity over a collecting lens, simulating what would be measured by a photomultiplier tube. We use a beam waist of 0.55 µm and a NA = 1.0 collecting lens. The result is shown in purple in Fig. 28, where we see that the nonlinear ptychographic reconstructions (orange, green, red) are able to resolve individual fibrils better than the simulated experiment (purple). For example, around $x = 0.0$ µm, we see two fibrils close to each other. In the simulated experiment, this becomes a single peak whereas in the reconstructions, two peaks are distinguished.

In typical I-SHG measurements, a lateral resolution of 0.6 µm can be obtained [2], where 16000 scanned points per millimeter are required to retrieve the phase of $\chi^{(2)}$. Thus the 12 µm × 12 µm area that we image here would require 4000 measurements for phase retrieval with I-SHG. Our nonlinear ptychography scheme in contrast requires almost two orders of magnitude fewer measurements.

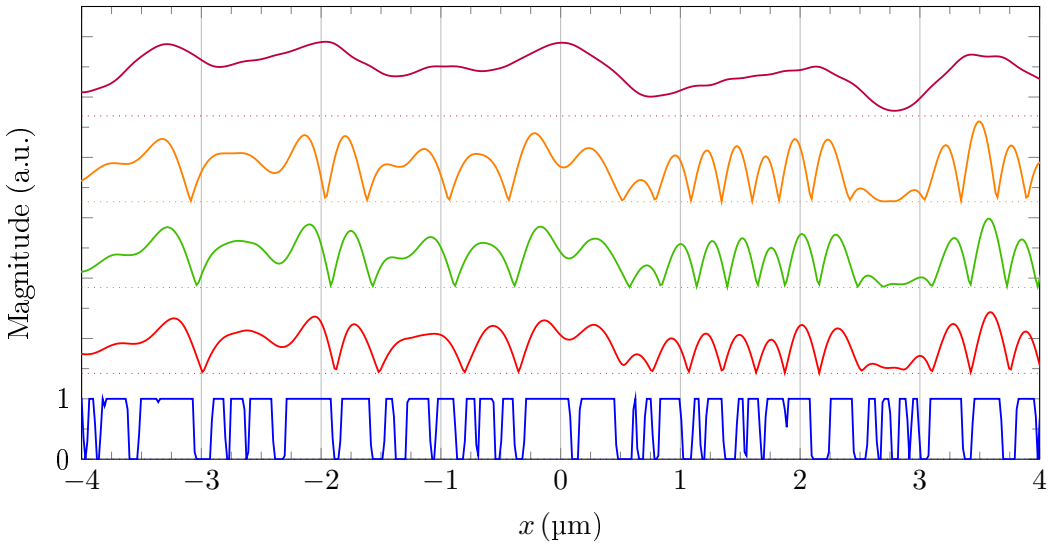

Figure 28: Magnitude of $\chi^{(2)}$ for the object in Fig. 25 (blue) and those reconstructed with input beams with waist sizes of 0.55 µm (red), 1.10 µm (green), and 2.20 µm (orange). A simulated experiment measuring only far-field intensity with a 0.55 µm beam and a 1.0 NA collecting lens is plotted on top in purple.

5.4 Results for coherent anti-Stokes Raman scattering

For our second example, we apply nonlinear ptychography to CARS, which provides label-free molecule-specific non-destructive imaging of biological samples and tissues [78, 119]. It allows for video-rate [51, 54, 55] and hyperspectral imaging [77], where in the latter per-pixel spectral information is obtained. CARS probes the third-order nonlinear susceptibility, $\chi^{(3)}$, using two input beams (called the pump and Stokes beams). When the frequency difference between these two beams is resonant with an unique vibrational mode for a particular molecular species, the signal at the anti-Stokes frequency will become very strong, allowing for chemical specificity. However, nonresonant processes from the background material can significantly degrade the CARS signal-to-noise ratio. Numerous techniques already exist to reduce the nonresonant background, such as heterodyne detection [80] and FM-CARS [83]. However, we find that nonlinear ptychography can also reduce the nonresonant background, providing in addition enhanced resolution and compensation for beam distortions.

The induced nonlinear polarization for CARS scales as $P \propto \chi^{(3)} E_p^2 E_s^\star$, where E_p is the electric field from the pump beam electric field at the sample and E_s the Stokes. To apply nonlinear ptychograpy to CARS, we take $\chi^{(3)}$ as the object, and $E_p^2 E_s^\star$ as

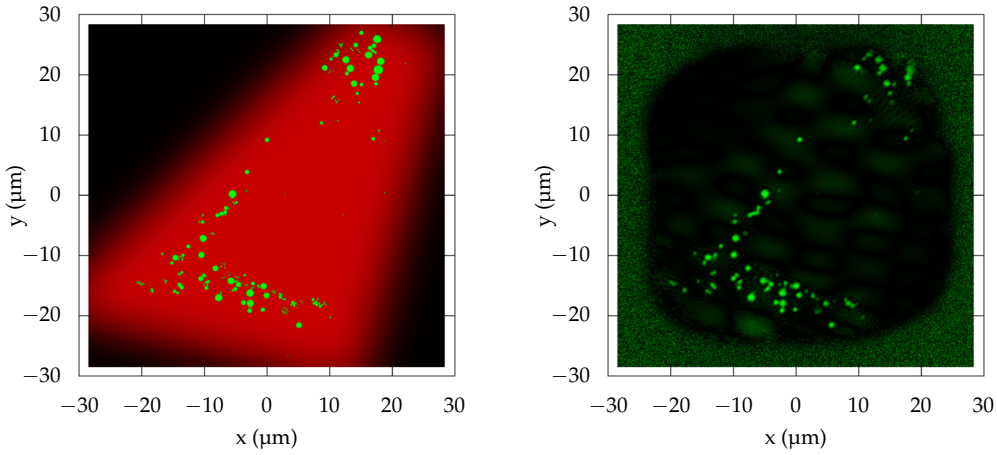

Figure 29: Simulated fibroblast imaged using CARS. The left plot shows the original simulated cell with resonant material in green and nonresonant material in red. In the right plot the imaginary component of the reconstruction is shown. Little nonresonant material is visible.

the probe. The nonlinear optical susceptibility contains resonant, $\chi_{\mathrm{R}}^{(3)}$, and nonresonant parts, $\chi_{\mathrm{NR}}^{(3)}$, where $\chi_{\mathrm{R}}^{(3)}$ is imaginary and $\chi_{\mathrm{NR}}^{(3)}$ is real, *i.e.*, a phase difference of $\pi/2$ between them. Retrieving the phase therefore allows us to distinguish the nonresonant background signal from the resonant CARS signal, thus improving the signal-to-noise ratio, similar to heterodyne detection [80].

An example is shown in Fig. 29 for a generated object similar to an experimental image by Nan et. al of a fibroblast cell [139]. Our generated sample is shown on the left plot in Fig. 29 where lipid spheres with diameters up to 1.3 µm (green) are contained in a nonresonant background (red). We calculate $M = 100$ images in the far-field with an NA=1.0 lens. We use distorted Gaussian pump and Stokes beams at 712 nm and 892 nm, respectively, generating an anti-Stokes signal at 592 nm. For both beams the waist radius is 10 µm. We iterate the algorithm $N = 300$ times and plot on the right of Fig. 29 the imaginary part of the reconstructed $\chi^{(3)}$. Even though the nonresonant background has not completely been removed, it is reduced significantly and the plot shows good agreement with the resonant part of the original object.

5.5 Conclusion

In conclusion, we developed ptychography for nonlinear optical microscopy that we applied to SHG imaging of simulated rat tail tendon and to CARS imaging of a simulated

fibroblast cell, in both cases using distorted input beams. We were able to reconstruct $\chi^{(2)}$ of the rat tail tendon, including its phase, without interferometry, and with orders of magnitude less laser exposures than required by interferometric SHG. Further, we obtained higher resolution than standard SHG imaging. We also reconstructed $\chi^{(3)}$ of the fibroblast cell, including its phase, using ptychography with CARS. This reduced the nonresonant background without requiring nonlinear interferometric vibrational spectroscopy [83, 140]. Our nonlinear ptychography scheme can potentially be applied to other nonlinear optical imaging processes, allowing one to obtain phase without interferometry, enhanced resolution, and to account for random defects in the input beams.

5.A The ePIE algorithm for nonlinear optical microscopy

In the preceding sections, I have shown how the ePIE algorithm has been extended such that is can be used with nonlinear optical microscopy. Here I will expand on the algorithm I used in more detail so that it can be understood without needing a background in ptychography. A well-written overview for linear ptychography going into great detail was done by Rodenburg [91]. It however lacks the reconstruction of the input beam, which was published later by Maiden et al. [125]. Neither cover nonlinear optical microscopy.

The ability to reconstruct the phase from only the far-field intensity comes in essence from the extra information in overlapping measurements. To illustrate the point how it is possible to obtain phase information from intensity measurements alone, imagine a 1D object that consists of just two points of unknown complex-valued susceptibility. Now suppose the imaging beam is a top-hat function. Positioning the beam such that it images just one of the points will reveal the magnitude of the susceptibility of that point. Positioning the beam such that both points are illuminated, will result in an interference pattern in the far-field that is essentially Young's double-slit experiment in the limit of infinitely small slits. When one of the slits has a phase delay of ϕ, the interference pattern is given as

$$I(\theta) \propto \cos^2\left(\frac{kd}{2}\sin\theta + \phi/2\right), \tag{112}$$

where d is the distance between the two points, k is the wave number, and θ is the far-field angle. From this pattern both the distance between the two points and the relative phase-difference of their complex-valued susceptibilities can be deduced. This is the basis for ptychography. Interference of the coherent light scattered (or emitted) by the sample

itself allows for the phase of the sample to be retrieved through multiple measurements.

Of course, for more complex samples than just two points the far-field pattern gets a great deal more complicated. However, the general idea is the same; a coherent source is needed and there needs to be overlap between the measurements and this is the basis on which ptychography rests.

In the case of nonlinear optical microscopy, the object to be reconstructed by ePIE is a spatial varying two-dimensional ν-th-order nonlinear susceptibility, $\chi^{(\nu)}(\vec{r})$, where $\vec{r}$ represents the two spatial coordinates in the sample plane. The electric field of the i-th input beam, $\vec{E}_i(\vec{r}-\vec{r}_m)$, is a Gaussian beam where $\vec{r}_m$ indicates the position of its centre on the sample. The index m corresponding to one of the M measurements which together form the input of the ePIE algorithm. The induced nonlinear polarization for a nonlinear optical process has the form

$$\vec{P}_{\mathrm{NL}}(\vec{r},\vec{r}_m) = \epsilon_0 \sum_{ij_1j_2\ldots j_\nu} \chi^{(\nu)}_{ij_1j_2\ldots j_\nu}(\vec{r}) E_{j_1}(\vec{r}-\vec{r}_m) E_{j_2}(\vec{r}-\vec{r}_m)\ldots E_{j_\nu}(\vec{r}-\vec{r}_m)\hat{e}_i, \tag{113}$$

where $\hat{e}_i$ is an unit vector and $\chi^{(\nu)}(\vec{r})$ is a rank $\nu+1$ tensor. To simplify matters, I will only consider an input beam that is polarized in the y-direction and propagating in the z-direction. Furthermore, I choose the only non-zero component of $\chi^{(\nu)}$ to be the y...y-component. In that case, only the y-component of $\vec{P}$ is nonzero and we can drop the indexes to get only the scalar expression

$$P_{\mathrm{NL}}(\vec{r},\vec{r}_m) = \epsilon_0 \chi^{(\nu)}(\vec{r}) \prod_{j=1}^{\nu} E_j(\vec{r}-\vec{r}_m) \tag{114}$$

$$= \epsilon_0 \chi^{(\nu)}(\vec{r}) \mathcal{E}(\vec{r}-\vec{r}_m), \tag{115}$$

where I have introduced the shorthand $\mathcal{E}$ to represent the combined electric field of all the input beams. The part of this expression that relates to the sample is called the object and is just $\chi^{(\nu)}$. The fields are called the probe, which in this case is $\mathcal{E}$. This can be generalized to include other components of the tensor, but for simplicity I consider only one here.

Since the probe is the product of all the input beams, it is only possible to reconstruct the electric field of the input beam if there is only one input beam. For example, for SHG I have $\mathcal{E} = E^2$ and only a square root is needed. But for CARS, where $\mathcal{E} = E_p^2 E_s^\star$, there are two input beams and the electric field of each input beam separately cannot be recovered. This however is not a problem because even though the individual input beams are not reconstructed, $\mathcal{E}$ is. Therefore any systematic errors in any of the input beams are still accounted for.

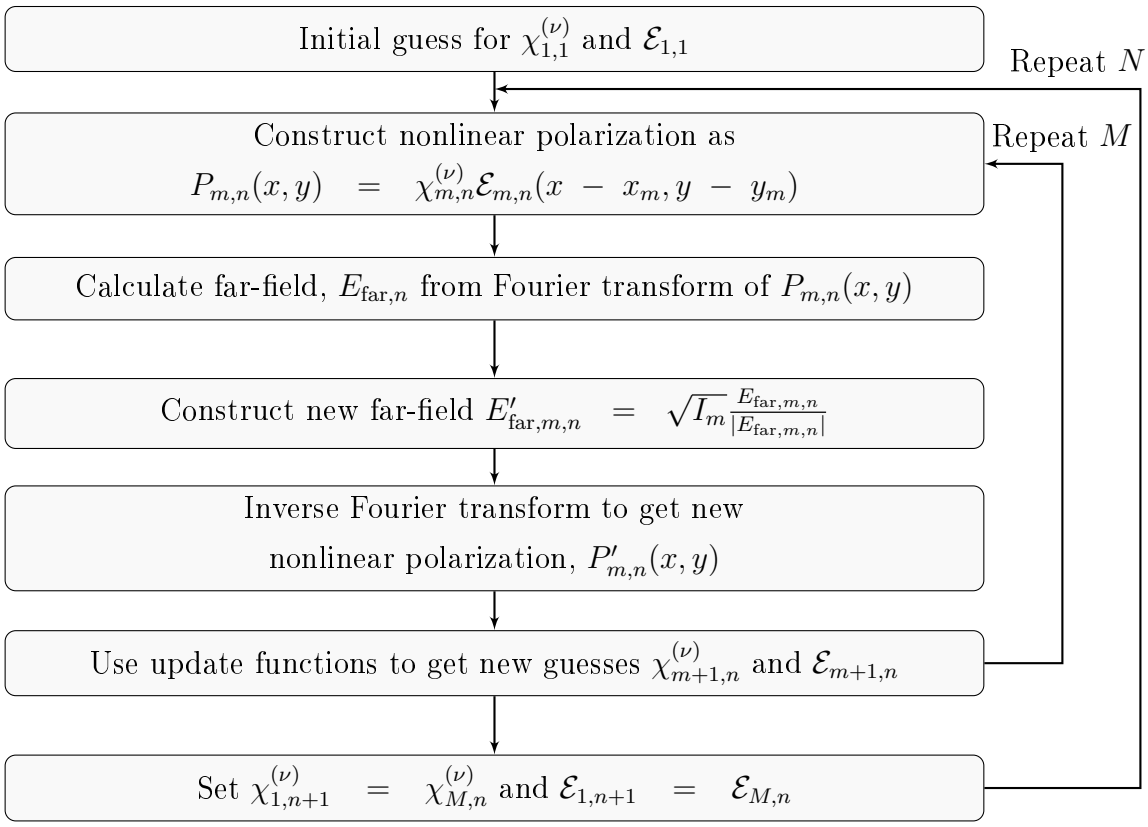

Figure 30: Flow chart for the ptychography algorithm.

The first step of the ptychography algorithm is to make guesses for the object $\chi^{(\nu)}$ and and probe $\mathcal{E}$. The guess for the object is initialized with complex-valued random noise. For the input beam I already have some information, namely that they are roughly Gaussian beams. So instead I initialize that with a pure real-valued Gaussian function with a waist approximately the same as the observed spot size in the hypothetical experiment. This helps the algorithm to converge much faster.

To get an overview of the algorithm, a flow chart of the process is shown in figure 30. After the initial guesses, the induced nonlinear polarization of equation (114) is used to calculate the far-field image using the Green's function approach as we saw for SHG in chapter 3. In the far-field this approach is equivalent to taking a Fourier transform, as I derive explicitly in appendix 5.B. As a Fourier transform, the operation is now mostly invertible which is a property needed for the ptychographic algorithm. It is not fully invertible because in the far-field, the evanescent waves will have disappeared. Thus calculating the inverse Fourier transform only the lower spatial frequencies are available, which is the reason that the resolution of the reconstruction cannot go beyond

the diffraction limit.

At this stage I have the guessed electric field in the far-field, E_{far}, which is complex-valued, *i.e.* it has information on both the magnitude and phase. It does however not have any information about the sample because it is only based on the guessed nonlinear susceptibility and the guessed input fields. The CCD provides the actual measurement of the far-field intensity pattern, I, but this of course only has information about the magnitude and knows nothing of the phase. To get information from the measurements into the guesses, I combine the fields by taking the phase from the guess and the magnitude from the measurement to obtain a hybrid field as

$$E'_{\text{far}} = \sqrt{I}\arg(E_{\text{far}}). \tag{116}$$

Using an inverse Fourier transform of this quantity results in a hybrid polarization, P'_{SHG} that contains information about the measurements.

The difference between P' and P contains information about how far off the guesses are from the real sample and input beams. By using this difference to update the nonlinear susceptibility and the electric field product of the input beams, we can obtain guesses that are closer to the real object and input beams. The expressions for updating the object, $\chi^{(\nu)}$, and the probe, $\mathcal{E}$, are

$$\chi^{(\nu)}_{m+1,n}(\vec{r}) = \chi^{(\nu)}_{m,n}(\vec{r}) + \alpha\frac{\mathcal{E}m,n^{\star}(\vec{r}-\vec{r}_m)}{\max\left[|\mathcal{E}_{m,n}(\vec{r}-\vec{r}_m)|^2\right]}\left[P'_{m,n}(\vec{r}) - P_{m,n}(\vec{r})\right] \tag{117}$$

$$\mathcal{E}_{m+1,n}(\vec{r}-\vec{r}_m) = \mathcal{E}_{m,n}(\vec{r}-\vec{r}_m) + \beta\frac{\chi^{(\nu)}_{m,n}(\vec{r})^{\star}}{\max\left[|\chi^{(\nu)}_{m,n}(\vec{r})|^2\right]}\left[P'_{m,n}(\vec{r}) - P_{m,n}(\vec{r})\right], \tag{118}$$

where the function $\max[|A|^2]$ takes the maximum of $|A|^2$ in the entire spatial domain. To see why this works, recall that P is the product of the object and probe, thus to get a correction for the object from the difference between P' and P one would ideally like to divide out the probe. That cannot be done directly because divisions by zero could occur. Instead one multiplies by the conjugate of the probe and divides by the absolute value squared. By taking instead the spatial maximum of the absolute value squared, the problem of dividing by zero is circumvented. The same applies to the expression for updating $\mathcal{E}$ and dividing by the object $\chi^{(\nu)}$.

The coefficients α and β determine the rate of convergence of the object and probe respectively. Choosing these too large will make the algorithm divergent as the correction to the guess is too large and overshoots. When they are too small, the convergence will take too long. I choose $\alpha = 1$ and set $\beta = 0$ for the first 100 iterations and $\beta = 1$

afterwards. This allows the object to be reconstructed from the random noise before the reconstruction of the probe commences. We can do this because we know the probe is Gaussian-like and doing so aids convergence.

After performing this procedure for all M recorded images, the new guessed object $\chi^{(\nu)}_{M,n}$ and guessed probe $\mathcal{E}_{M,n}$ will be closer to the real object and probe. This concludes the first iteration, $n = 1$, of the algorithm. The input guess for the next iteration is the output of the last iteration such that

$$\chi^{(\nu)}_{1,n+1} = \chi^{(\nu)}_{M,n} \tag{119}$$

$$\mathcal{E}_{1,n+1} = \mathcal{E}_{M,n}. \tag{120}$$

The reconstruction gets better with more iterations where we can use the same previously recorded M images. I iterate over the M images N times to get ever closer to the original object and probe.

5.B Green's function to Fourier transform

The far-field SHG-signal can be calculated using the Green's function approach as

$$E_{\text{far}}(\omega_{\text{NL}}, \vec{r}) = \int P(\omega_{\text{NL}}, \vec{r}')G(\vec{r}, \vec{r}')d^3\vec{r}', \tag{121}$$

where ω_{NL} is the output frequency and P is the induced nonlinear polarization for the nonlinear optical process of interest, which can be written as $P(\omega_{\text{NL}} = \omega_{\text{NL}}, \vec{r}) = \chi^{(\nu)}(\omega_{\text{NL}}, \vec{r}) \prod_{i=1}^{\nu} E(\omega_i, \vec{r})$. For example, for SHG the induced nonlinear polarization is $P(2\omega, \vec{r}) = \chi^{(2)}(2\omega, \vec{r})E^2(\omega, \vec{r})$. Finally, $G(\vec{r}, \vec{r}')$ is the Green's function for the free-space Helmholtz equation as was also discussed in section 2.2. The form of this Green's function is

$$G(\vec{r}, \vec{r}') = \frac{\exp(\mathrm{i}\, k_{\text{NL}}|\vec{r} - \vec{r}'|)}{4\pi|\vec{r} - \vec{r}'|}, \tag{122}$$

where k_2 is the wave number for the SHG radiation. In the far-field, $r \gg r'$, the quantity $|\vec{r} - \vec{r}'|$ can be simplified:

$$|\vec{r} - \vec{r}'| = \left[(x - x')^2 + (y - y')^2 + (z - z')^2\right]^{1/2} \tag{123}$$

$$= r\left[1 + \frac{-2xx' - 2yy' - 2zz' + (r')^2}{r^2}\right]^{1/2} \tag{124}$$

$$\approx r\left[1 + \frac{1}{2}\frac{-2xx' - 2yy' - 2zz'}{r^2}\right] \tag{125}$$

$$= r - \frac{xx' + yy' + zz'}{r}. \tag{126}$$

I can plug that into the numerator of (122) and use only $|\vec{r}-\vec{r}'| \approx r$ in the denominator. This is equivalent to the Fraunhofer diffraction condition. Then put that in turn into (121) to get an expression for the far-field pattern as

$$E_{\text{far}}(\omega_{\text{NL}}, \vec{r}) = \frac{\exp(\mathrm{i}\, k_{\text{NL}} r)}{4\pi r} \iiint \chi^{(\nu)}(\omega_{\text{NL}}, \vec{r}') \prod_{i=1}^{\nu} E(\omega_i, \vec{r}') \times \exp\left(-\mathrm{i}\, k_{\text{NL}} \frac{xx' + yy' + zz'}{r}\right) d^3\vec{r}'. \tag{127}$$

Since our sample is 2D, the integral over z' is over an infinitesimal distance δz over which z' is constant, or more specifically, zero. I then have

$$E_{\text{far}}(\omega_{\text{NL}}, \vec{r}) = \frac{\delta z \exp(\mathrm{i}\, k_{\text{NL}} r)}{4\pi r} \iint \chi^{(2)}(\omega_{\text{NL}}, \vec{r}') \prod_{i=1}^{\nu} E(\omega_i, \vec{r}') \times \exp\left(-\mathrm{i}\, k_{\text{NL}} \frac{xx' + yy'}{r}\right) dx'\, dy'. \tag{128}$$

I introduce variables $K_x = k_{\text{NL}} x/r$ and $K_y = k_{\text{NL}} y/r$, so the equation becomes

$$E_{\text{far}}(\omega_{\text{NL}}, \vec{r}) = \frac{\delta z \exp(\mathrm{i}\, k_{\text{NL}} r)}{4\pi r} \iint \chi^{(\nu)}(\omega_{\text{NL}}, \vec{r}') \prod_{i=1}^{\nu} E(\omega_i, \vec{r}') \times \exp\left[-\mathrm{i}\, (K_x x' + K_y y')\right] dx'\, dy', \tag{129}$$

which is just a Fourier transform of the quantity $\chi^{(\nu)}(\omega_{\text{NL}}, \vec{r}') \prod_{i=1}^{\nu} E(\omega_i, \vec{r}')$, where the far-field coordinates x and y correspond to the wave numbers as $x = rK_x/k_{\text{NL}}$ and $y = rK_y/k_{\text{NL}}$.

6

Role of refractive index in SHG imaging of fibril bundles

In Chapter 3, I have investigated the imaging of collagen fibrils with SHG and have shown that by comparing the experimental data to simulations, subresolution features can be obtained such as fibril diameter by examining the F/B ratio and fibrillar orientation by examining the standard deviation of the phase of the forward far-field SHG signal. In chapter 4, I have also demonstrated that for SRS and CARS imaging, near-field effects can play a large role. In this chapter, I investigate the effect of a refractive index mismatch on imaging collagen fibrils with SHG. The fibrils are much smaller than the spheres studied in chapter 4, so the enhancement will not be as large and the forward directed SHG signal not largely affected. However, I will show that the backward directed signals can be significantly affected due to an altered phase matching condition due to near-field effects, and that these effects remain significant, and are measurable, in collagenous tissues such as tendon.

The simulations are presented in this chapter have not all been done by myself directly, though I directed all the simulations and provided all the parameters. Antonino Calà Lesina performed the FDTD simulations with his own code [141] while Charalambos

Kioulos implemented the cylindrical Mie solution with the free-space Green's function approach, both under my direction. My simulations are also based on the Mie solution, but have corrections to the phase that I implemented, which are required to alter the refractive index of the background medium for the outgoing propagating wave calculated from the free-space Green function. The ensemble average calculations as well as the text is solely my work.

We are currently preparing a manuscript based on this chapter that will be submitted soon[3]. Based on the results presented here, our collaborators have become interested in the topic, and we aim to publish another joint theory/experimental paper over the next several months. Some of their preliminary results appear here.

6.1 Introduction

From section 1.2, recall that collagen fibrils are found in a wide array of biological tissues such as bones, tendons, arteries, cornea and many others, and that they form the basis for more complex hierarchies such as collagen fibres which in turn can comprise tendons and bone [38].

Additionally, some pathologies are traced down to failures in the structure created by fibrils. Diseases such as Osteoarthritis, which leads to joint pain, show changes in the structure of the collagen tissue and cartilage degradation as one of the earliest symptoms [138]. No effective treatment exists yet to either stop the progression or to reverse the disease, nor is the cause well known at this time. Thus early detection will be enormously beneficial in the understanding of such diseases. Other diseases such as diabetes increase crosslinking between collagen fibrils and molecules leading to accelerated ageing [142].

Studying these fibrils in detail requires high-resolution microscopes as the diameters of the fibrils range from only 10 nm to 500 nm. Techniques that allow for this include transmission electron microscopy, atomic force microscopy and fluorescence microscopy. However, all of these methods require sample preparation, and the first two would be hard to implement in-vivo. Fluorescence microscopy is more suited for in-vivo, but requires the use of labels or has to rely on the weak two-photon excited fluorescence [143]. Second Harmonic Generation (SHG) is a non-linear optical process that is particularly strong in collagen fibrils due to the chiral structure of the collagen molecules, which enables label-free imaging of collagen tissue [15]. The fibrils are smaller than the diffraction limit at

[3] J.N. van der Kolk, C. Kioulos, A.C. Lesina, and L. Ramunno, *Near-field effects on SHG Imaging*, in preparation

the commonly used infrared frequencies, but it has been shown that the radiation pattern of the SHG signal correlates with both the size and distribution of subwavelength-sized scatterers because of the coherent nature of SHG [32]. In particular, the ratio of the far-field SHG intensity in the forward direction to that in the backward, *i.e.* the F/B ratio, is a metric that is often used. For example, morphology changes as a function of depth are observed [144], and morphology changes as indicated by the F/B ratio can also be used as a diagnostic tool to predict preterm birth [145] and observe progression of breast cancer [146]. Through numerical modelling, properties such as fibril diameter and fibril bundling are obtained quantitatively from the F/B ratio [147–149] and images of the F/B ratio map out the distribution of fibril size in cartilage and bone [1].

However, most models do not take into account inhomogeneity of the linear index of refraction. The few that do only consider scattering [150] or the refractive index mismatch of the cover slip [151]. My calculations show that small differences of the refractive index of $\Delta n/n = 0.1$ between the collagen fibrils and the background medium, as commonly found in biological tissue and prepared samples, can lead to a change in the measured F/B ratio of a distribution of fibrils of $\sim$30 % in rat tail tendon between those embedded in a $n = 1.47$ background medium versus those in $n = 1.33$. Due to a mismatch in refractive index between fibrils and the background medium, near-field enhancements of the pump occur inside the fibrils in the order of a few percent. While I find that this does not significantly affect the far-field signal in the forward direction, the far-field signal in the backward direction is particularly sensitive as these enhancements alter phase matching conditions.

To test the validity of my theoretical findings, I have sought collaboration with Stéphane Bancelin and François Légaré whose preliminary experimental measurements for mouse tail tendon show that a change of the refractive index of the background medium can alter the F/B ratio by as much as 40 ± 20 % which is consistent with my theoretical results for mouse tail tendon is $\sim$30 % (similar to rat tail tendon).

To understand the effect of a refractive index mismatch between fibrils and the background medium, I first examine the case of a single fibril using analytical calculations as well as simulations. Subsequently, I extend this to simulated samples of rat tail tendon which will contain a distribution of fibrils in the laser focal spot, and finally compare theoretical results to experimental results in mouse tail tendon.

6.2 Single fibrils

I model collagen fibrils as infinitely long dielectric cylinders aligned along the y-axis with a nonzero second-order nonlinear susceptibility, $\chi^{(2)}$. I only consider the $\chi^{(2)}_{yyy}$ component to be nonzero because it is the largest component due to the molecular structure in the collagen molecules. Furthermore, the fibril is illuminated by a y-polarized plane wave propagating in the x-direction. The fibril has a refractive index of $n = 1.4$ while the background medium is either index-matched or has $n = 1.33$ (water) or $n = 1.47$ (paraffin/glycerol).

For the index-matched case, there exists an analytical expression for the far-field SHG electric field in the forward and backward direction, which I write as, respectively [15]:

$$E_f \propto \chi^{(2)} E_0^2 k^2 \pi r^2 \tag{130}$$

$$E_b \propto \chi^{(2)} E_0^2 k \pi r J_1(2kr) \exp(-2\mathrm{i}\, kx), \tag{131}$$

where E_0 is the field strength for the incoming plane wave, r is the radius of the cylinder, k is the wave number for the SHG radiation, and x is the position of the fibril along the x-axis. The full derivation is found in appendix 6.A. The constants containing the distance to the far-field have been left out as they are the same for the forward and backward direction when the distance to the fibril is the same. The expression for the total radiated SHG far-field in the forward direction does not depend on the position of the fibril as it is always phase-matched to the incident light. This is true down to the level of the individual scatterers inside the cylinder, which is why the forward field simply scales with the area of the cylinder cross section, πr^2. In the backward direction, the phase matching is only over very short distances, which means that the fields of the individual scatterers in the cylinder interfere destructively in larger fibrils. The radii for which complete destructive interference occur correspond to the zeros of the expression for the backward far-field signal, equation (131), which are the zeros of the Bessel function of the first kind. From these expressions, I calculate the F/B ratio as:

$$\frac{I_f}{I_b} = \frac{|E_f|^2}{|E_b|^2} = \frac{k^2 r^2}{J_1^2(2kr)}. \tag{132}$$

When complete destructive interference occurs in the backward direction, the F/B ratio becomes infinite due to the backward signal being zero. Of course in experiments the backward signal is never completely zero, for example, due to the shot noise of the detector. However, the F/B ratio will still be very large.

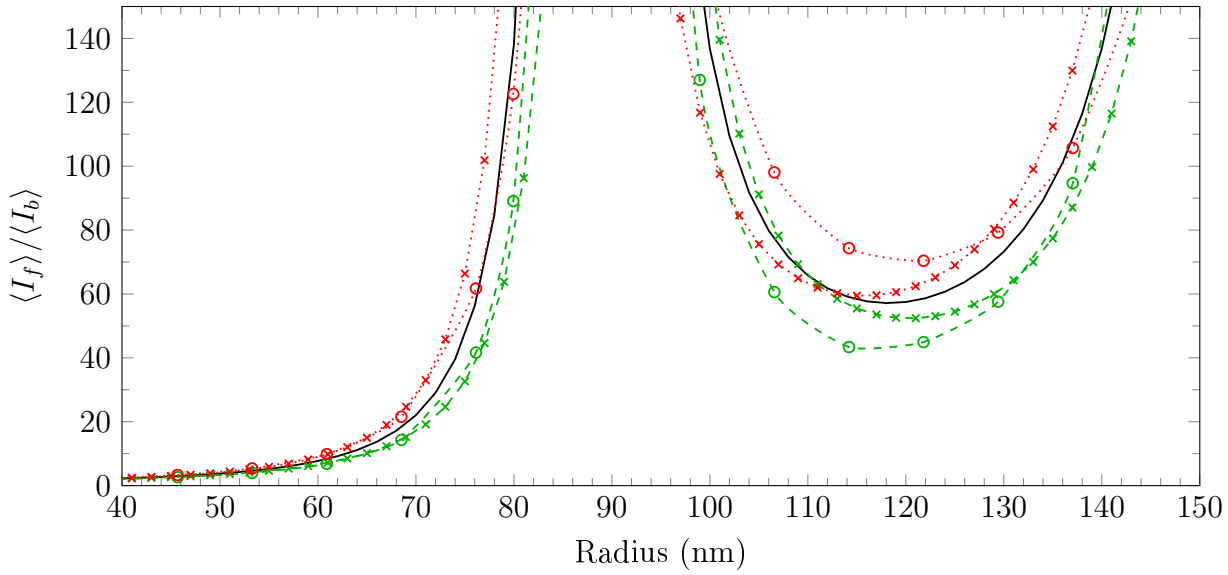

Figure 31: The F/B ratio versus cylinder radius in a $n = 1.33$ (green dashed) and $n = 1.47$ (red dotted) background medium. The black solid line is the analytical model where the cylinder has the same refractive index as the background medium. For the Mie/Green's function approach (crosses) and the FDTD approach (circles), the cylinder always has a refractive index of $n = 1.4$.

I now consider the case when the fibril cylinder is index-mismatched to its surrounding dielectric environment. I keep the refractive index of the cylinder fixed at $n = 1.40$ while varying the index of refraction of the background medium, corresponding to studying the fibrils in-vivo ($n = 1.33$) or fixated ($n = 1.47$). I calculate the near-fields using the cylindrical Mie solution for cylinders as described in section 2.3, obtain the induced nonlinear polarization with in the cylinder ($P \propto E^2$), then from this calculate the far-field SHG signal using a free-space (at $n = 1.40$) Green's function approach as described in section 2.2. The free-space Green's function is at $n = 1.40$ because the nonlinear optical process happens inside the fibril where the input beam experiences a $n = 1.40$ medium. This approach takes into account only the effect of near-field enhancements on the far-field SHG signals and does not account for scattering effects of the SHG radiation due to refractive index mismatch between the fibril and the background medium. However, FDTD as described in section 2.1 does account for these effects. By utilizing both Mie/Green's function as well as FDTD, I am able to study the effect of near-field enhancements of the input beam separately from scattering effects on the SHG radiation.

In figure 31, I show the F/B ratio as a function of radius for a cylinder illuminated

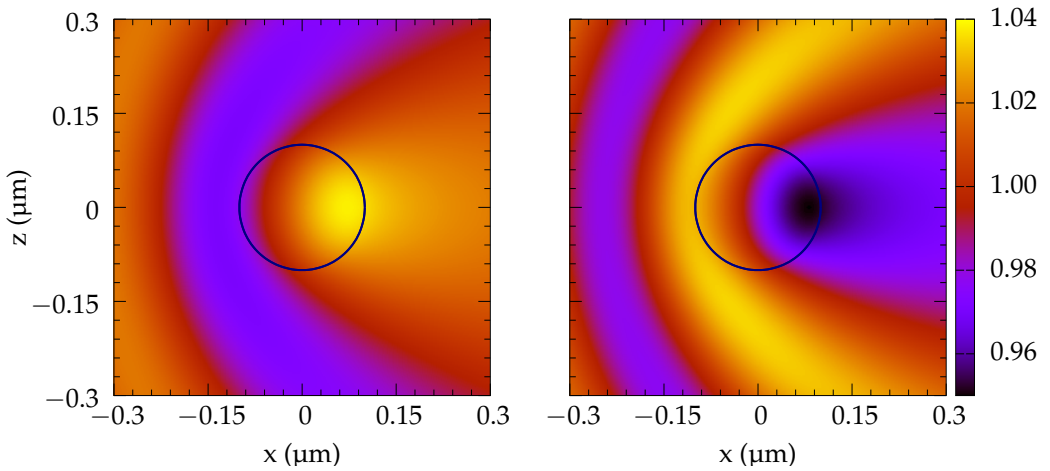

Figure 32: The near-fields of an incident plane wave interacting with a cylinder ($n = 1.4$, $r = 100\,\text{nm}$) as calculated by Mie theory. The cylinder is indicated by the blue circle. From left to right, the cylinder was placed in a background medium with $n = 1.33$ and $n = 1.47$. The plane wave propagates from left to right.

by a plane wave with a wavelength of $\lambda = 810\,\text{nm}$ for the three different methods (*i.e.*, equation (132) assuming index matching, cylindrical Mie/Greens approach, and FDTD) with a background medium of $n = 1.33$ (green) and $n = 1.47$ (red). For very small radii, the F/B ratio tends to one because in that domain the cylinders act as ideal dipole sources with the same far-field signals in the forward as in the backward direction.

Figure 31 indicates that refractive index mismatch affects the measured F/B ratio, though the effects are only noticeable for the larger cylinders. For example, a cylinder in the $n = 1.33$ medium with a radius of 120 nm has a F/B ratio that is 8.7 % smaller compared to the analytical formula when taking into account only near field enhancements within the cylinder. That goes up to 22.5 % when taking into account the diffraction effects on the SHG signal using FDTD. Fibrils in biological tissues generally have a radius smaller than 100 nm, however in rat and mouse tail tendon larger ones do occur in small numbers [106, 152]; we will see that near-field effects from even a few larger fibrils will significantly affect F/B ratios in such tissues.

The reason the F/B ratio calculated with an index-mismatched background differs from the simple analytical formula for the index matched case, is due to the enhanced electric fields of the pump beam. This is visible in figure 32, where I plot the enhanced pump fields in and around a cylinder with a radius of $r = 100\,\text{nm}$ for two different back-

ground dielectric media. Regions of enhanced and decreased fields within the cylinder are clearly visible, even though the electric field of the input beam is only modified by 5 % at most. In the forward direction, the SHG signal is always phase-matched thus the far-field SHG fields emitted by each of the scatterers in the cylinder adds coherently. The sum of field strengths inside of a cylinder in a $n = 1.33$ medium only increases by 1.3 % whereas the average field inside of a cylinder in a $n = 1.47$ medium decreases by just 0.9 %. As the far-field SHG intensity in the forward direction depends on this sum, the contributions of the increase and decrease has little effect and the effect of the index mismatch is therefore small. In the backward direction however, SHG signals generated from different locations can destructively interfere because the backward emitted SHG fields are not phase matched. Thus, having an area within a fibril that contributes either more or less than other areas will change the destructive interference condition, and alter the backward signal, and this is what responsible for the distortion of the peaks in figure 31. Near the point where complete destructive interference takes place, *i.e.* when the denominator in the F/B ratio is close to zero, the effect is substantial. In fact, it will shift the location of this zero, so that a hot (or cold) spot within the fibril will make the fibril appear as if it had a larger (or smaller) effective radius, as compared to its geometric radius. It is therefore not the overall change in field strength that causes the F/B ratio to be affected; it is purely an altered destructive interference effect.

6.3 Effects on F/B ratio in fibrillar tissue

Fibrils in tissue are always part of a bigger collection of fibrils. When using a tightly focused input beam, hundreds of fibrils are illuminated by the pump field and thus generate SHG radiation. Here I will use rat tail tendon of 13–14 week old rats as this is a common model used for SHG imaging; it also contains the largest fibril diameters [153]. Mature mouse tail tendon was investigated experimentally by our collaborators, and will also be considered theoretically. The difference between the two tissues lies in the radii distribution. The one for rat tail is a single peak around 65 nm with a long tail up to radii of 200 nm, whereas for mouse tail tendon the distribution consists of three separate peaks with a Gaussian shape and radii up to 100 nm. I will focus on rat tail tendon for the theoretical part as that is what we used for our initial investigation, while the experimental work was done for mouse tail tendon at a later date.

6.3.1 Theoretical investigation for rat tail tendon

To get valid statistics for SHG far field signals from tendon, I generate numerically 100,000 random tendon samples by placing fibrils in a non-overlapping manner at random locations in a simulation domain. The diameter of each fibril is randomly selected from the size distribution of the tissue of interest; the details of the rat tail distribution I used can be found in reference [106]. I will apply the same Mie/Green's function approach as described in section 6.2, which gives faster results than FDTD, though is expected to underestimate the effect because the effect of the refractive index mismatch on the SHG radiation is not accounted for.

In experiments one would use a tightly focused beam, but for a reasonable computational time, I instead consider plane wave excitation, but with a simulation domain that is restricted to a square box with a size equivalent to the laser spot size. Here I model a focused laser beam with a waist of 0.55 µm with a simulation domain of 1.1 µm × 4.5 µm. However, I assume infinitely long cylinders so that I can continue to use 2D simulations. This allows me to reduce the computational cost associated with running simulations for 100,000 samples. I have verified this approximation by comparing the F/B ratios from the 2D FDTD simulations to those from a small number of 3D simulations.

The distribution over fibril radii, P_r, is determined by the type of tissue. The sample is defined by P_r, the packing ratio ρ (the area occupied by the cylinders in the xz-plane divided by the total area of the simulation domain), and the positive-to-total fraction f (defined as the number of fibrils with a positive $\chi^{(2)}$ divided by the total number of fibrils). For the 13–14 week old rat tail tendon, P_r is given by [107]

$$P_r(r) = \frac{4r}{r_0^2} \exp\left(-\frac{2r}{r_0}\right), \tag{133}$$

where r_0 is the mean radius which for 13–14 weeks old rat tail tendon is $r_0 = 65\,\text{nm}$. This particular formula was obtained by fitting the distribution measured by electron microscopy [106]. Observations of rat tail tendon in nature show that it is tightly packed, thus usually $\rho \approx 0.70$ [106].

The tendon is numerically generated by placing fibrils randomly in a simulation domain and using the known size distribution for the fibril diameter. This process has been described in detail in section 2.4, but in brief: I randomly pick a radius according to P_r, and place the fibrils inside the simulation domain at random positions until the desired value of ρ is reached. Initially, the fibrils will overlap, thus I use a molecular dynamics simulation with reflecting boundaries to push the fibrils until they no longer

overlap. Inside of the simulated samples, all of the cylinders are aligned along the y-axis, which corresponds with fibrils found in tendon. They either point "up" or "down", which corresponds to a positive or negative second-order nonlinear susceptibility, $\chi^{(2)}$, respectively.

To obtain the F/B ratio for a collection of fibrils in experiments, one collects the average forward intensity $\langle I_f \rangle$ as well as the average backward intensity $\langle I_f \rangle$. The F/B ratio is then defined as $\langle I_f \rangle / \langle I_b \rangle$.

First I extend the analytical expression for the forward and backward field for the index-matched cylinder for multiple fibrils. The SHG electric field in the forward and backward direction of a single sample with multiple fibrils in the index-matched case is derived by summing the fields of the individual fibrils in the sample using equations (130) and (131). From this the ensemble average of many samples is derived using the relevant distribution $P_r(r)$. It is assumed that the coordinates of the fibrils are uniformly distributed and are uncorrelated to those of the other fibrils. The sign of $\chi^{(2)}$ is distributed such that there a chance of f for the $\chi^{(2)}$ of a fibril to be positive and $1-f$ for it to be negative. Under these conditions, the expectation value of the forward and backward SHG intensity signal is

$$\langle |E_f|^2 \rangle \propto k^4 r_0^4 \left(\frac{15}{2} N + \frac{9}{4} N(N-1)(2f-1)^2 \right) \tag{134}$$

$$\langle |E_b|^2 \rangle \propto N k^2 \int_0^\infty r^2 J_1^2(2kr) P_r(r)\, dr \tag{135}$$

where N is the number of fibrils in the simulation domain which is related to the packing fraction ρ as $\rho = N\pi\langle r^2 \rangle / A$, where A is the area of the simulation domain. The derivation can be found in appendix 6.B.

From this expression, it is clear that the SHG signal in the backward direction does not depend on the f ratio. The reason for this is that the phase of the SHG electric field in the far-field in the backward direction of a single fibril depends on the x-coordinate in the simulation domain. As the fibril position is random, the contributions of each fibril will have a random phase as well, thus the extra imparted phase due to the sign of $\chi^{(2)}$ will not have any effect when calculating the ensemble average. In the forward direction, the far-fields of each fibril add up coherently and the far-field SHG intensity is predicted to have a quadratic dependence on f. The $(2f-1)$ term is the expectation value of $\chi^{(2)}$ for a single fibril and the square represents the average interference between a fibril (of which there are N) and all of its neighbours (of which there are $N-1$).

Another observation is that the F/B ratio is independent of the number of fibrils N

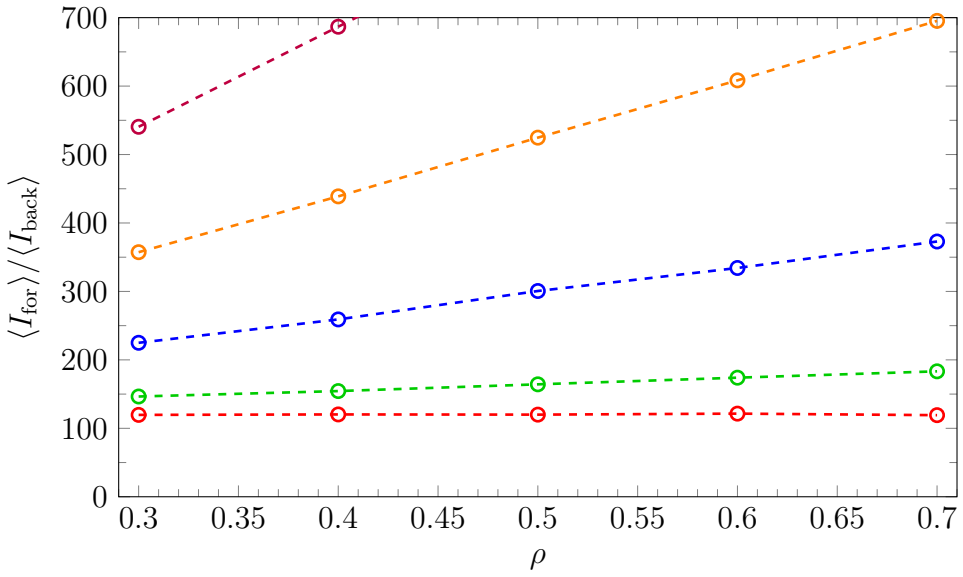

Figure 33: The F/B ratio as a function of ρ for simulated rat tail tendon samples in an index-matched background medium after 100,000 simulations. From top to bottom for $f = 0.30, 0.35, 0.40, 0.45, 0.50$. The error bars are too small to show.

and thus of the packing fraction ρ only if the ratio $f = 0.5$. In earlier work it was claimed that the F/B ratio is independent of ρ [1, 147]. In figure 33, I plot the F/B ratio as a function of ρ for various values of f. I find that the independence of the F/B ratio on ρ is approximately true in the range of $0.47 \leq f \leq 0.53$, which is within the range of f found in nature for mice [107], but not for instance for cartilage [2].

I now investigate the effect of a refractive index mismatch on SHG far-field F/B ratios in rat tail tendon by using the Mie/Green's function approach. As I require 100,000 samples per simulation I will only use this method since it is orders of magnitude faster than FDTD while still demonstrating the effect of a mismatch in the refractive index, though underestimated. However, for collections of fibrils the Mie/Green's function approach requires a correction to the far-field phase. Too see why, recall that I used the free-space Green's function at $n = 1.40$ to get the correct phase matching conditions inside of the cylinder. This leads to an incorrect phase in the far-field as the SHG radiation travels through a medium with $n \neq 1.40$, which is not a problem for the single fibril because I measure intensity, but it is for multiple fibrils because of the addition of the far-field electric fields of each individual fibril. To correct for that, I calculate the Mie/Green's function approach with each fibril placed at $x = 0\,\mu\text{m}$. In the forward direction, no correction is needed because all the signals are phase matched anyway. To

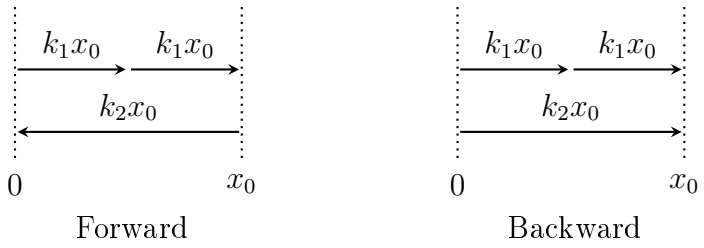

Figure 34: Diagram explaining the correction needed for Mie/Green's function simulations of samples with a distribution of fibrils. Left is the situation for the forward direction and right for the backward.

correct for the actual position of the fibril, x_0, in the backward direction I apply an extra factor of $\exp(-2ik_2x_0)$. Figure 34 shows that when translating a fibril from position 0 to x_0, the input beam travels for an additional distance x_0 to reach the new position, picking up an extra phase of k_1x_0. Since two photons are used in the SHG process, this is doubled to $2k_1x_0$. In the forward direction, the SHG radiation now has to travel a distance of x_0 less, which means an extra phase difference of k_2x_0. Since $k_2 = 2k_1$, this means there will be an extra phase of 0 in total when moving the fibril to the new position x_0 for the SHG signal in the forward direction. However, as shown in the right diagram in figure 34, the k_2 vector is now in the opposite direction, thus instead of $k_2x_0 - 2k_1x_0$ that we had in the forward direction, we now have $-k_2x_0 - 2k_1x_0$, which translates into an extra phase of $-2k_2x_0$.

Figure 35 shows the F/B ratio as a function of f for the index matched case, from equations (134) and (135) (solid black line) and is compared to Mie/Green's function simulations of an index-matched collection of fibrils (blue) using 100,000 samples with $\rho = 0.70$, which shows that the simulation results are consistent with the index-matched ensemble averaged formula. I also plot in figure 35 two index-mismatched cases, calculated via the Mie/Green's approach, with background media of $n = 1.33$ (green) and $n = 1.47$ (red). A significant drop in the F/B ratio is observed for $n = 1.33$ while a significant increase is observed for $n = 1.47$. The difference between the $n = 1.47$ case and the $n = 1.33$ case is $31.8 \pm 0.7\,\%$ for rat tail tendon over the range of $f = 0.4$ to $f = 0.5$.

6.3.2 Experimental results for mouse tail tendon

I now turn to discussing the experimental results. I discussed my theoretical findings from the previous section with our experimental collaborators, Stéphane Bancelin and

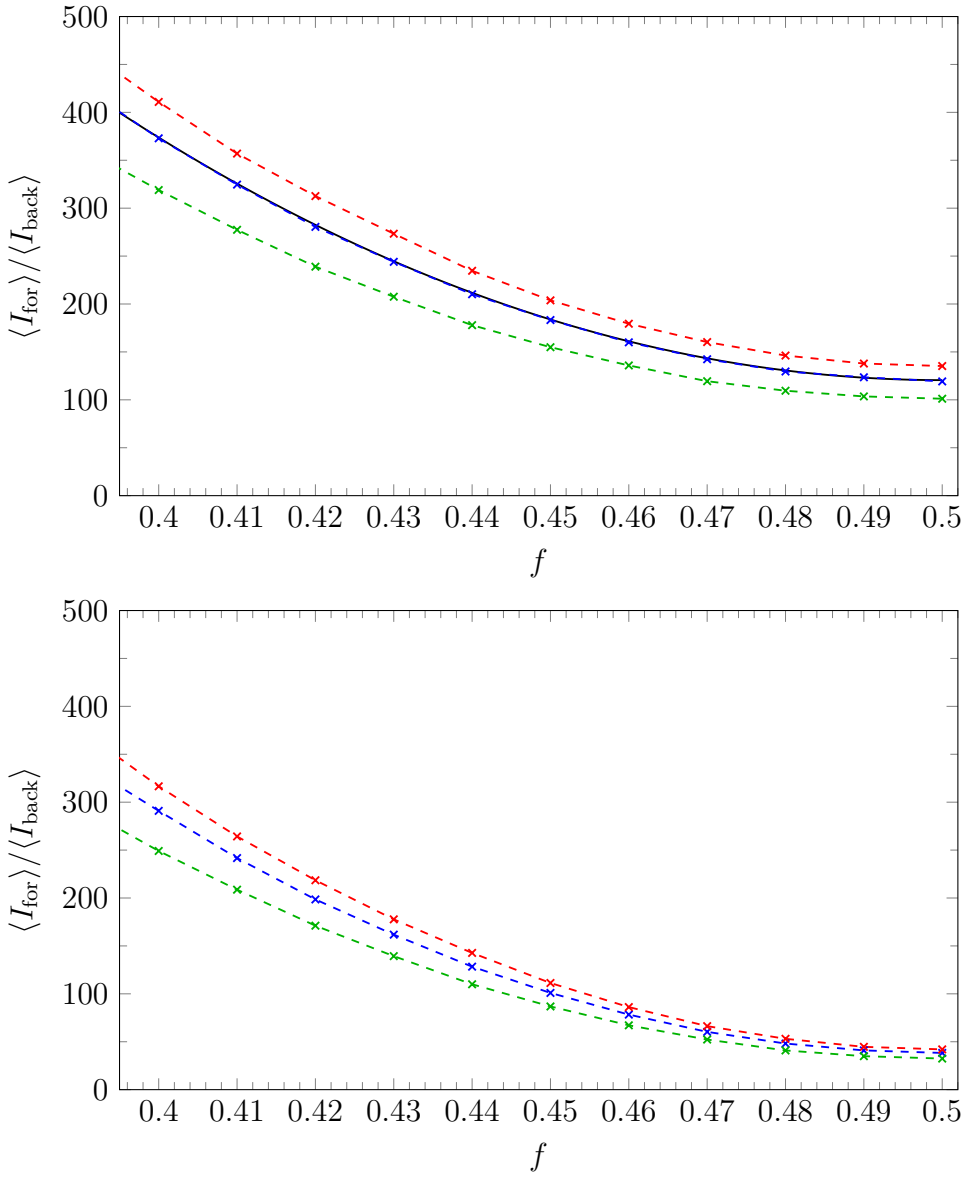

Figure 35: The F/B ratio versus the ratio of positive to total fibrils, f, for 13–14 week old rat tail tendon (top) and mature mouse tail tendon (bottom). All samples are tightly packed with $\rho = 0.70$. The cylinders always have $n = 1.40$. The plots are for the ensemble average (solid black) and Mie/Green's function simulations for $n = 1.33$ (green), $n = 1.40$ (blue), and $n = 1.47$ (red).

François Légaré. As the effect of refractive index mismatch on the F/B ratio was a previously unknown effect, they were intrigued and were able to perform the experiment. Mouse tail tendon was used instead of rat tail tendon, but the radii distribution is also known for that tissue, I was able to extend my theoretical work to mouse tail tendon as well. For mature mouse tail tendon a triple normal distribution was fitted to the measured fibril radii [152]:

$$P_r(r) = \sum_{i=1}^{3} c_i \exp\left(-\frac{(r-r_i)^2}{\sigma_i^2}\right), \tag{136}$$

where $c_1 = 15\,\%$, $c_2 = 63\,\%$, $c_3 = 12\,\%$, $r_1 = 18.3\,\text{nm}$, $r_1 = 63.9\,\text{nm}$, $r_1 = 93.65\,\text{nm}$, $\sigma_1 = 5.7\,\text{nm}$, $\sigma_2 = 14.6\,\text{nm}$, and $\sigma_3 = 5.7\,\text{nm}$. Like rat tail tendon, the mouse tail tissue is tightly packed, thus $\rho = 0.70$.

In the bottom plot in figure 35, the results of the simulations are shown for different refractive indexes of the background medium. I find that the increase of the F/B ratio from $n = 1.47$ background medium versus $n = 1.33$ is $28.1 \pm 0.6\,\%$ for mouse tail tendon within the range of $f = 0.4$ to $f = 0.5$; the individual percentages are shown in the right plot in figure 36. Stéphane Bancelin performed experimental measurements on mature mouse tail tendon using a focused input beam with a wavelength of 810 nm. The fibrils in the mouse tail tendon were immersed in either water ($n = 1.33$) or glycerol ($n = 1.47$) such that a refractive index mismatch exists between the fibrils and the background medium. The results after five measurements are shown in the left plot of figure 36. There is a significant increase in the measured F/B ratio of the fibrils in water, as compared to the fibrils in glycerol: $40 \pm 20\,\%$, which is consistent with the theoretical model for f in the range of 0.4 to 0.5. The error bar of the experimental measurements is large because this was a preliminary experiment and measurements were only taken at five positions.

6.4 Conclusion

To calculate far-field SHG signals from fibrils that are have a refractive index that is mismatched with their surrounding environment, I use both a Mie/Green's function approach as well as a computational electrodynamics method, FDTD. For the Mie/Green's function approach, I use cylindrical Mie theory to calculate the electric field of the pump input beam within a fibril. From these fields, the induced nonlinear polarization is calculated for SHG, which is then used to calculate the far-field SHG intensity signal in

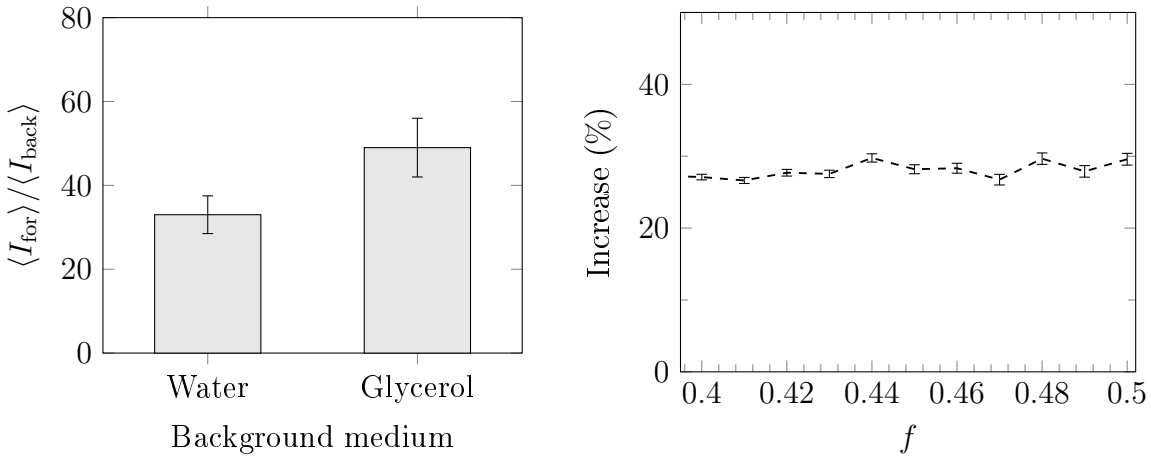

Figure 36: The left plot shows the experimental F/B measurements for mature mouse tail tendon in water and glycerol (courtesy of Stéphane Bancelin). Averages are from five measurements. The right plots shows the theoretically predicted increase of the F/B ratio as a function of f of 100,000 samples embedded in a $n = 1.47$ background medium with respect to $n = 1.33$.

the far-field using a free-space Green's function. FDTD automatically incorporates all effects of refractive index mismatch on the SHG radiation with the trade-off that it is orders of magnitude slower than the Mie/Green's function approach.

My findings show that for single fibrils a small mismatch with the background refractive index can have an impact on the F/B ratio, though only for fibrils with a radius larger than 100 nm which do occur with some frequency in certain collageneous tissues. Comparison between a Mie/Green's function approach and FDTD simulations shows two comparable effects of linear index mismatch at play: (1) field enhancements inside of the fibrils that lead to uneven SHG generation within the fibril and altered destructive interference of the backward radiated field, and (2) linear scattering of the SHG radiation from cylinders on its way to the far field.

In biological tissues, multiple fibrils exist in the focal area thus collections of fibrils need to be considered. In the case where there is perfect index matching between the fibrils and their environment, I derive an analytical formula for the ensemble average over rat tail tendon, and show that the F/B ratio depends on the packing ratio ρ and the positive-to-total ratio f. Using the Mie/Green's function approach on 100,000 simulated samples of rat tail tendon, I find that the effect of the index mismatch is significant due to the presence of large fibrils. Even though large fibrils do not occur that frequently,

they still contribute the most to the SHG signal and therefore significantly alter the measured F/B ratio of the samples. I found an increase of the F/B ratio of $31.8 \pm 0.7\,\%$ for rat tail tendon when comparing collection of fibrils embedded in $n = 1.47$ to those embedded in $n = 1.33$. These results are likely an underestimate as my methodology only accounts for the near-field enhancements inside of the cylinders and disregards the effect of the refractive index mismatch on the SHG radiation as it propagates through the sample as well as the possible near-field enhancements caused by neighbouring fibrils. The calculated results were experimentally confirmed for mouse tail tendon where an increase of $40 \pm 20\,\%$ was observed versus a theoretical prediction of $28.1 \pm 0.6\,\%$ for mouse tail tendon.

The near-field effects due to the refractive index mismatch as I have demonstrated here cannot be removed by any known experimental technique, aside from finding a perfectly index matched background; they are intrinsic to the SHG generation itself. Thus in general, experiments concerning the F/B ratio in tissues where the representative fibril diameter distribution allows for fibrils larger than 100 nm, need to correct for these effects, for example, by using the theory in this chapter, as even small refractive index mismatches can have a large effect on the F/B ratio. This may skew quantitative diameter measurements where the F/B ratio is correlated to fibril diameter through the analytical formula. However, qualitative measurements such as for example in [1] where fibril diameter was studied in human cartilage are still valid. There it was observed that fibrils close to the surface are smaller than those deeper down. Even though refractive index mismatch was not considered, the reported trends still hold.

6.A Derivation of analytical expression

An analytical expression for the far-field SHG signal in the forward and backward direction generated by a plane-wave illuminated cylinder with non-zero second-order nonlinear electric susceptibility, $\chi^{(2)}$, can be derived analytically. This was shown by Freund et al. [15]. As their paper does not clearly show the derivation, I will use this appendix to show my own derivation. It should be noted that Konstantin Popov, who is a former post-doc in my group, derived the same expression through a different method.

To calculate the expression for the SHG radiation I consider a y-polarized plane wave propagating in the x-direction as the input beam, which can be written in the form

$$\vec{E}_1(\vec{r}, \omega_1) = E_0 \exp(\mathrm{i}k_1 x)\hat{y}, \tag{137}$$

where $k_1 = n\omega_1/c$ is the wave number of the input beam, ω_1 is the frequency of the input beam, n is the refractive index of the entire medium, and E_0 is the field strength of the input beam. The induced nonlinear polarization for SHG is

$$\vec{P}(\vec{r},\omega_2) = \epsilon_0\chi^{(2)}(\vec{r},\omega_2 = \omega_1 + \omega_1)\vec{E}_1(\vec{r},\omega_1)\vec{E}_1(\vec{r},\omega_1), \tag{138}$$

where ω_2 is the frequency of the SHG radiation and ϵ_0 is the electric permittivity in vacuum. To calculate the electric field for the generated nonlinear where signal outside of the cylinder, I use Maxwell's equations to obtain the wave equation in the frequency domain

$$\nabla \times \nabla \times \vec{E}(\vec{r},\omega_2) = \frac{n^2\omega_2^2}{c^2}\vec{E}(\vec{r},\omega_2) + \mu_0\omega_2^2\vec{P}(\vec{r},\omega_2), \tag{139}$$

where c is the speed of light in vacuum and μ_0 is the magnetic permittivity in vacuum. By introducing the Hertz vector, $\vec{Z}$, which is defined by $\vec{E} = k^2\vec{Z} + \nabla(\nabla\cdot\vec{Z})$ [99, 102], where k is the wave number of the field to be calculated, this wave equation can be rewritten as a Helmholtz equation

$$\nabla^2\vec{Z}(\vec{r},\omega_2) + k_2^2\vec{Z}(\vec{r},\omega_2) = -\frac{1}{\epsilon_0 n^2}\vec{P}(\vec{r},\omega_2), \tag{140}$$

where $k_2 = n\omega_2/c$ is the wave number of the SHG radiation. Note that I assume the refractive index is the same at ω_1 and ω_2, *i.e.* a dispersionless medium. This is an acceptable approximation as I am assuming a confocal geometry, thus the forward fields from the input beam at ω_1 and the SHG radiation ω_2 are phase-matched. Furthermore, the second-order nonlinear susceptibility, $\chi^{(2)}$ is a rank-3 tensor, which means that the individual equations for the vector components in the equation above are coupled. However, as my input beam is only polarized in the y-direction, I only need to consider the tensor component $\chi^{(2)}_{xyy}$, $\chi^{(2)}_{yyy}$, $\chi^{(2)}_{zyy}$. Of these components, the $\chi^{(2)}_{yyy}$ component is by far the largest [100], thus I will ignore the other components, leaving me with just one. In that case I only need to consider Z_y and $\chi^{(2)}_{yyy}$, thus I drop the subscripts.

In free-space, the Helmholtz equation has a well-known Green's function solution, which is [99, 154]

$$G(\vec{r},\vec{r}',\omega_2) = \frac{\exp(\mathrm{i}k_2|\vec{r}-\vec{r}'|)}{4\pi|\vec{r}-\vec{r}'|}. \tag{141}$$

The Hertz field of the SHG radiation outside of the cylinder is then

$$Z(\vec{r},\omega_2) = \int_V P(\vec{r}',\omega_2)G(\vec{r},\vec{r}',\omega_2)\,d\vec{r}', \tag{142}$$

where the integral is over the entire volume V of the cylinder. In the far-field where $|x| \gg |x'|$, I approximate $|\vec{r} - \vec{r}'|$ as

$$|\vec{r} - \vec{r}'| = \sqrt{(x - x')^2 + (y - y')^2 + (z - z')^2} \tag{143}$$

$$\approx \sqrt{x^2 - 2xx' - 2yy' - 2zz'} \tag{144}$$

I want to know the on-axis signal, so that means that $y = z = 0$. Thus, the approximation becomes

$$|\vec{r} - \vec{r}'| \approx x\sqrt{1 - 2\frac{xx'}{x^2}} \tag{145}$$

$$\approx |x| \left|1 - \frac{1}{x}x'\right| \tag{146}$$

$$= |x - x'|. \tag{147}$$

So the far-field SHG electric field is then

$$Z_{\text{far}}(\vec{r}, \omega_2) = \frac{\epsilon_0 \chi^{(2)}}{4\pi|x|} \int_V \exp(2\mathrm{i}k_1 x') \exp(\mathrm{i}k_2|x - x'|)\, d\vec{r}', \tag{148}$$

where I have approximated $|x - x'| \approx |x|$ in the denominator because I am in the far-field. This cannot be done for the term in the exponential because the phase is sensitive to small changes due to its $\mod 2\pi$ nature. Using this expression, the SHG signal in the forward and backward direction is calculated. In the forward direction $x > x'$, so equation (148) becomes

$$Z_{\text{far}}(\vec{r}, \omega_2) = \frac{\epsilon_0 \chi^{(2)}}{4\pi|x|} \int_V \exp(2\mathrm{i}k_1 x') \exp(\mathrm{i}k_2(x - x'))\, d\vec{r}'. \tag{149}$$

Because I assumed a dispersionless medium, I use $k_2 = 2k_1$ to get

$$Z_{\text{far}}(\vec{r}, \omega_2) = \frac{\epsilon_0 \chi^{(2)} \exp(2\mathrm{i}k_1 x)}{4\pi|x|} \int_V d\vec{r}'. \tag{150}$$

The integral now just gives the volume of the cylinder, which is $\pi r^2 \ell$, where r is the radius of the cylinder and ℓ the length, giving

$$Z_{\text{far}}(\vec{r}, \omega_2) = \frac{\epsilon_0 \chi^{(2)} r^2 \ell \exp(2\mathrm{i}k_1 x)}{4|x|}. \tag{151}$$

This needs to be converted back from the Hertz field to the electric field. In the far-field the term $\nabla(\nabla \cdot \vec{Z})$ in the definition of the Hertz vector only contains terms that fall off

with distance faster than those in $\vec{Z}$, so this means the E-field is obtained by multiplying Z by a factor of k_2^2. Thus the electric field of the SHG signal in the forward direction is

$$E_{\text{far}}(\vec{r},\omega_2) = \frac{k_2^2\epsilon_0\chi^{(2)}r^2\ell\exp(2\mathrm{i}k_1x)}{4|x|}. \tag{152}$$

In the backward direction, $x < x'$, so equation (148) becomes

$$Z_{\text{far}}(\vec{r},\omega_2) = \frac{\epsilon_0\chi^{(2)}}{4\pi|x|}\int_V \exp(2\mathrm{i}k_1x')\exp(\mathrm{i}k_2(x'-x))\,d\vec{r}'. \tag{153}$$

Now I again use $k_2 = 2k_1$ to get

$$Z_{\text{far}}(\vec{r},\omega_2) = \frac{\epsilon_0\chi^{(2)}\exp(-\mathrm{i}k_2x)}{4\pi|x|}\int_V \exp(2\mathrm{i}k_2x')\,d\vec{r}'. \tag{154}$$

In cylindrical coordinates I have $z' = \rho'\cos\theta'$ and the integral becomes

$$Z_{\text{far}}(\vec{r},\omega_2) = \frac{\epsilon_0\chi^{(2)}e^{-\mathrm{i}k_2x}}{4\pi|x|}\int_{-\ell/2}^{\ell/2}\int_0^{2\pi}\int_0^r \rho'\exp(2\mathrm{i}k_2\rho'\cos\theta')\,dy'\,d\theta'\,d\rho'. \tag{155}$$

The integral over y' is easily done and results in a factor ℓ:

$$Z_{\text{far}}(\vec{r},\omega_2) = \frac{\epsilon_0\chi^{(2)}\ell e^{-\mathrm{i}k_2x}}{4\pi|x|}\int_0^{2\pi}\int_0^r \rho'\exp(2\mathrm{i}k_2\rho'\cos\theta')\,d\theta'\,d\rho'. \tag{156}$$

The integral over θ' is done using *Mathematica* and leaves

$$Z_{\text{far}}(\vec{r},\omega_2) = \frac{\epsilon_0\chi^{(2)}\ell e^{-\mathrm{i}k_2x}}{2|x|}\int_0^r \rho' J_0(2\mathrm{i}k_2\rho')\,d\rho', \tag{157}$$

where J_0 is the zeroth order Bessel function of the first kind. Finally, the integral over ρ' is also done by *Mathematica* to get

$$Z_{\text{far}}(\vec{r},\omega_2) = \frac{\epsilon_0\chi^{(2)}rJ_1(2k_2R)\ell e^{-4\mathrm{i}k_2x}}{4k_2|x|}. \tag{158}$$

Converting back to the electric field as before leads to

$$E_{\text{far}}(\vec{r},\omega_2) = \frac{k_2\epsilon_0\chi^{(2)}rJ_1(2k_2r)\ell e^{-4\mathrm{i}k_2x}}{4|x|}. \tag{159}$$

Together with the expression for the forward direction, I calculate the F/B ratio analytically by dividing the absolute values squared of equations (152) and (159), which is

$$\frac{I_f}{I_b} = \frac{k_2^2r^2}{J_1^2(2k_2r)}, \tag{160}$$

which is the expression I used in the previous section.

6.B Ensemble average

The ensemble average of the far-field SHG intensity signal is the average of the signal generated by many random many samples containing multiple fibrils. For a given sample, the total electric field (far-field) in the forward direction is found by applying the analytical expression from equation (152) and summing the far-field electric fields for each fibril in the sample. Likewise for the backward direction using (159). Each sample contains fibrils that have radii that are randomly generated from a given radii distribution such that the total area of all of the fibrils in the simulation domain conforms to a given packing ratio ρ. Furthermore, the positions of the fibrils are randomly generated using an uniform distribution. Finally, the value of the second-order nonlinear electric susceptibility, $\chi^{(2)}$ is taken as $+1$ with a probability of f and -1 otherwise. The properties of each fibril in the randomly generated sample are assumed to be uncorrelated with the others.

The ensemble average is then the expectation value for such randomly generated samples. Since the SHG far-field signals depend on the radius, the second-order nonlinear susceptibility and (in the case of the backward direction), on the position, I require the probability functions for all of those quantities. I use the distribution for rat tail tendon [106], which is

$$P_r(r) = \frac{4r}{{r_0}^2} \exp\left(-\frac{2r}{r_0}\right), \tag{161}$$

where r_0 is the mean fibril radius, which is $r_0 = 65\,\text{nm}$. This formula does not have a physical underpinning but was chosen because it fits the data [107]. Having an analytical form makes it possible to do an analytical calculation. The $\chi^{(2)}$ is either positive or negative depending on the ratio f and the sign corresponds to the fibril orientation; fibrils that are "up" have a positive sign and those that are "down" have a negative one. So the probability function is therefore

$$P_{\chi^{(2)}=1} = f \tag{162}$$

$$P_{\chi^{(2)}=-1} = 1 - f. \tag{163}$$

The last remaining probability function is that for the positions of the fibrils which are randomly placed in the xz-plane where the x-axis coincides with the direction of the laser propagation. The position of the fibril affects the phase of the input beam it "sees" because fibrils moved further from the source will experience a retarded phase. In the forward direction the SHG radiation will be phase-matched regardless of fibril position,

so position only affects the far-field SHG electric field in the backward direction. Since the input beam is a plane wave, only the distance along the laser propagation axis, *i.e.* the x-axis, matters. Thus the z-coordinate of the fibrils has no effect on the phase, only the x-coordinate does.

The position dependence can be generalized even further since the effect of the position is only on the phase, which means that instead of a random x-coordinate, I use a random phase instead. The range of this phase depends on the length of the sample along the laser-propagation axis, which in this case is several wavelengths long. Thus the phase ranges over the entire range of $[0, 2\pi)$ with uniform probability.

$$P_\phi = \frac{1}{2\pi}. \tag{164}$$

That is, the probability for each value of the phase ϕ is equally probable. Note that this assumes that all x-coordinates of the cylinder are equally probable as well, and thus that it may overlap with other cylinders. However, the z-coordinate can have any arbitrary value and can be chosen such that they do not overlap.

The ensemble averages for the forward and backward far-field SHG signal are now calculated by calculating the expectation value of a collection of N cylinders in a simulation domain. This expectation value is the same a the ensemble average over many samples.

6.B.1 Forward

The far-field SHG signal in the forward direction for a cylinder is given by equation (130), which is

$$E_f = \chi^{(2)} E_0^2 k^2 \pi r^2, \tag{165}$$

where $\chi^{(2)}$ is either $+1$ or -1. The fields add coherently, so for N cylinders, the field would be

$$E_{\text{for},N} = \sum_{i=1}^{N} \chi_i^{(2)} E_0^2 k^2 \pi r_i^2, \tag{166}$$

where $\chi_i^{(2)}$ is the sign and r_i the radius of the i-th cylinder. To calculate the expectation value for the far-field intensity of N cylinders, I assume that all of the radial probability distributions as well as the $\chi_i^{(2)}$ are not correlated to each other. The expectation value

is then

$$\langle |E_{\text{for},N}|^2 \rangle = \sum_{\chi_1^{(2)}} \cdots \sum_{\chi_N^{(2)}} \int_0^\infty \cdots \int_0^\infty \left(\sum_{i=1}^N \chi_i^{(2)} E_0^2 k^2 \pi r_i^2 \right)^2 \prod_{k=1}^N P_{\chi_k^{(2)}} P_r(r_k)\, dr_1 \ldots dr_N. \tag{167}$$

First I rewrite the squared term as

$$\left(\sum_{i=1}^N \chi_i^{(2)} E_0^2 k^2 \pi r_i^2 \right)^2 = E_0^4 k^4 \pi^2 \sum_{i=1}^N \sum_{j=1}^N \chi_i^{(2)} \chi_j^{(2)} r_i^2 r_j^2 \tag{168}$$

$$= E_0^4 k^4 \pi^2 \left(\sum_{i=1}^N \left(\chi_i^{(2)} r_i^2 \right)^2 + \sum_{i=1}^N \sum_{\substack{j=1 \\ j \neq i}}^N \chi_i^{(2)} \chi_j^{(2)} r_i^2 r_j^2 \right) \tag{169}$$

$$= E_0^4 k^4 \pi^2 \left(\sum_{i=1}^N r_i^4 + \sum_{i=1}^N \sum_{\substack{j=1 \\ j \neq i}}^N \chi_i^{(2)} \chi_j^{(2)} r_i^2 r_j^2 \right). \tag{170}$$

In the last step $\left(\chi_i^{(2)}\right)^2$ disappeared since the only two possible values are $(+1)^2$ and $(-1)^2$, which both are just 1. The two terms of equation (170) will be calculated separately. The first term is

$$\langle |E_{\text{for},N}|^2 \rangle^{(1)} = E_0^4 k^4 \pi^2 \sum_{\chi_1^{(2)}} \cdots \sum_{\chi_N^{(2)}} \int_0^\infty \cdots \int_0^\infty \sum_{i=1}^N r_i^4 \prod_{k=1}^N P_{\chi_k^{(2)}} P_r(r_k)\, dr_1 \ldots dr_N. \tag{171}$$

The sums over $P_{\chi_k^{(2)}}$ disappear since the probabilities always add up to 1. Similarly, the integrals over r_k disappear when $k \neq i$. So all that remains is

$$\langle |E_{\text{for},N}|^2 \rangle^{(1)} = E_0^4 k^4 \pi^2 \sum_{i=1}^N \int_0^\infty r_i^4 P_r(r_i)\, dr_i \tag{172}$$

$$= E_0^4 k^4 \pi^2 N \int_0^\infty r^4 P_r(r)\, dr, \tag{173}$$

where the last step makes use of the fact that all of the remain integrals are exactly the same.

The second term of equation (170) is only slightly more complicated.

$$\langle |E_{\text{for},N}|^2 \rangle^{(2)} = E_0^4 k^4 \pi^2 \sum^{\chi_1^{(2)}} \cdots \sum^{\chi_N^{(2)}} \int_0^\infty \cdots \int_0^\infty \sum_{i=1}^N \sum_{\substack{j=1 \\ j\neq i}}^N \chi_i^{(2)} \chi_j^{(2)} r_i^2 r_j^2 \times$$

$$\prod_{k=1}^N P_{\chi_k^{(2)}} P_r(r_k)\, dr_1 \ldots dr_N \tag{174}$$

$$= E_0^4 k^4 \pi^2 \sum^{\chi_1^{(2)}} \cdots \sum^{\chi_N^{(2)}} \int_0^\infty \cdots \int_0^\infty \sum_{i=1}^N \chi_i^{(2)} r_i^2 \sum_{\substack{j=1 \\ j\neq i}}^N \chi_j^{(2)} r_j^2 \times$$

$$\prod_{k=1}^N P_{\chi_k^{(2)}} P_r(r_k)\, dr_1 \ldots dr_N. \tag{175}$$

Now the terms where $k \neq i$ and $k \neq j$ reduce to 1, similar as before. So I am left with

$$\langle |E_{\text{for},N}|^2 \rangle^{(2)} = E_0^4 k^4 \pi^2 \sum^{\chi_i^{(2)}} \sum^{\chi_j^{(2)}} \int_0^\infty \int_0^\infty \sum_{i=1}^N \chi_i^{(2)} r_i^2 \sum_{\substack{j=1 \\ j\neq i}}^N \chi_j^{(2)} r_j^2 P_{\chi_i^{(2)}} P_r(r_i) \times$$

$$P_{\chi_j^{(2)}} P_r(r_j)\, dr_i dr_j. \tag{176}$$

The i and j are completely independent due to the condition that $i \neq j$, so I rearrange to

$$\langle |E_{\text{for},N}|^2 \rangle^{(2)} = E_0^4 k^4 \pi^2 \sum_{i=1}^N \sum^{\chi_i^{(2)}} \int_0^\infty \chi_i^{(2)} r_i^2 P_{\chi_i^{(2)}} P_r(r_i)\, dr_i \times$$

$$\sum_{\substack{j=1 \\ j\neq i}}^N \sum^{\chi_j^{(2)}} \int_0^\infty \chi_j^{(2)} r_j^2 P_{\chi_j^{(2)}} P_r(r_j)\, dr_j \tag{177}$$

$$= E_0^4 k^4 \pi^2 N(N-1) \left(\sum^{\chi^{(2)}} \int_0^\infty \chi^{(2)} r^2 P_{\chi^{(2)}} P_r(r)\, dr \right)^2 \tag{178}$$

$$= E_0^4 k^4 \pi^2 N(N-1)(2f-1)^2 \left(\int_0^\infty r^2 P_r(r)\, dr \right)^2. \tag{179}$$

The $N(N-1)$ term comes from the summation over i, which has N terms, and over j, which has $N-1$ terms. I then obtain the full expression for an arbitrary radial

distribution, $P_r(r)$, and obtain

$$\langle |E_{\text{for},N}|^2 \rangle = E_0^4 k^4 \pi^2 \left(N \int_0^\infty r^4 P_r(r)\, dr + N(N-1)(2f-1)^2 \times \left(\int_0^\infty r^2 P_r(r)\, dr \right)^2 \right). \tag{180}$$

For rat tail tendon I evaluate the two integrals:

$$\int_0^\infty r^2 P_r(r)\, dr = \frac{3}{2} r_0^2 \tag{181}$$

$$\int_0^\infty r^4 P_r(r)\, dr = \frac{15}{2} r_0^4. \tag{182}$$

Thus the expectation value of forward SHG signal intensity is

$$\langle |E_{\text{for},N}|^2 \rangle = E_0^4 k^4 \pi^2 r_0^4 \left(\frac{15}{2} N + \frac{9}{4} N(N-1)(2f-1)^2 \right). \tag{183}$$

Since the expectation value is the same as the ensemble average over many fibrils, I now have the ensemble average in the forward direction.

6.B.2 Backward

In the backward direction, the field for a single cylinder is given by equation (131):

$$E_{\text{back}} = E_0^2 k \chi^{(2)} \pi r J_1(2kr) e^{-2\mathrm{i}\, k x_0}. \tag{184}$$

There is now a dependence on the position of the fibril, x_0, which I need to take into account. As explained at the beginning of this appendix, the random position of the fibril adds a random phase when the simulation domain is longer than several wavelengths. Thus I substitute $e^{-2\mathrm{i}\, k x_0}$ with $e^{-\mathrm{i}\phi}$ and use the $P_\phi(\phi)$ probability distribution. Therefore the expectation value for the intensity in the backwards direction is calculated as

$$\langle |E_{\text{back},N}|^2 \rangle = \sum^{\chi_1^{(2)}} \cdots \sum^{\chi_N^{(2)}} \int_0^\infty \cdots \int_0^\infty \int_0^{2\pi} \cdots \int_0^{2\pi} \left| \sum_{i=1}^N \chi_i^{(2)} E_0^2 k \pi r_i J_1(2kr_i) e^{-\mathrm{i}\,\phi_i} \right|^2 \times \prod_{k=1}^N P_{\chi_k^{(2)}} P_r(r_k) P_\phi(\phi_k)\, dr_1 \ldots dr_N\, d\phi_1 \ldots d\phi_N \tag{185}$$

$$= E_0^2 k \pi \sum^{\chi_1^{(2)}} \cdots \sum^{\chi_N^{(2)}} \int_0^\infty \cdots \int_0^\infty \int_0^{2\pi} \cdots \int_0^{2\pi} \left| \sum_{i=1}^N \chi_i^{(2)} r_i J_1(2kr_i) e^{-\mathrm{i}\,\phi_i} \right|^2 \times \prod_{k=1}^N P_{\chi_k^{(2)}} P_r(r_k) P_\phi(\phi_k)\, dr_1 \ldots dr_N\, d\phi_1 \ldots d\phi_N. \tag{186}$$

I again work out the term inside the integrals, though now using the absolute value squared as I have complex numbers now:

$$\left|\sum_{i=1}^{N}\chi_i^{(2)}r_iJ_1(2kr_i)e^{-\mathrm{i}\,\phi_i}\right|^2 = \sum_{i=1}^{N}\sum_{j=1}^{N}\chi_i^{(2)}r_iJ_1(2kr_i)e^{-\mathrm{i}\,\phi_i}\chi_j^{(2)}r_jJ_1(2kr_j)e^{\mathrm{i}\,\phi_j} \tag{187}$$

$$= \sum_{i=1}^{N} r_i^2J_1^2(2kr_i) + \sum_{i=1}^{N}\sum_{\substack{j=1\\j\neq i}}^{N}\chi_i^{(2)}r_iJ_1(2kr_i)e^{-\mathrm{i}\,\phi_i}\times \chi_j^{(2)}r_jJ_1(2kr_j)e^{\mathrm{i}\,\phi_j}. \tag{188}$$

The first term has no dependence on the phase, thus the integrals and summations are similar to those in the forward direction. The only difference is that I have $r^2J_1(2kr)$ instead of r^4 in equation (173). Thus the first contribution to equation (186) is

$$\langle|E_{\mathrm{back},N}|^2\rangle^{(1)} = E_0^4k^2\pi^2N\int_0^\infty r^2J_1^2(2kr)P_r(r)\,dr. \tag{189}$$

This integral has no analytical solution, but is well-behaved and thus is calculated numerically quite easily.

The second term has two phase terms, thus the integrals over ϕ_i need to be considered. I can however still split the double summation as I did before and just need to solve the integral

$$\langle|E_{\mathrm{back},N}|^2\rangle^{(2)} = E_0^4k^2\pi^2\sum_{i=1}^{N}\sum^{\chi_i^{(2)}}\int_0^\infty \chi_i^{(2)}r_iJ_1(2kr_i)e^{-\mathrm{i}\,\phi_i}P_{\chi_i^{(2)}}P_r(r_i)P_\phi(\phi_i)\,dr_i\,d\phi_i\times$$
$$\sum_{\substack{j=1\\j\neq i}}^{N}\sum^{\chi_j^{(2)}}\int_0^\infty \chi_j^{(2)}r_jJ_1(2kr_j)e^{\mathrm{i}\,\phi_j}P_{\chi_j^{(2)}}P_r(r_j)P_\phi(\phi_j)\,dr_j\,d\phi_j. \tag{190}$$

However, the integrals over the phases evaluate to:

$$\int_0^{2\pi}e^{-\mathrm{i}\phi}\,d\phi = \int_0^{2\pi}e^{\mathrm{i}\phi}\,d\phi = 0. \tag{191}$$

Therefore the second term disappears completely and the backward intensity signal is independent of f, which leaves me with

$$\langle|E_{\mathrm{back},N}|^2\rangle = E_0^4k^2\pi^2N\int_0^\infty r^2J_1^2(2kr)P_r(r)\,dr. \tag{192}$$

This expression is independent on f due to the random phases that are introduced, which can be understood by looking at the phase of a single fibril. A fibril is assigned either

a $\chi^{(2)}$ of $+1$ or -1, which results in an extra phase either 0 or π in the far-field electric SHG field. However, each fibril also obtains a random phase due to its position in the backward far-field electric SHG field. Adding 0 or π to a random quantity still results in a random quantity, thus the far-field phase due to the sign of $\chi^{(2)}$ is irrelevant, and hence the expression does not depend on f which dictates the signs of $\chi^{(2)}$.

7

Conclusion

In this work, I have shown that the theoretical study of electromagnetic phenomena provides insight in the image formation process of nonlinear optical microscopes. It is clear, both through literature and my own investigations, that imaging using nonlinear optical microscopy provides additional information about samples beyond what linear optical microscopy can accomplish. Because microscopes provide deep insights in medical research and are used for diagnostic tools, I have concentrated on biological materials in this thesis. There is also a long history of using nonlinear microscopy with such material. In fact, the first SHG microscope was used on rat tail tendon. Of course, nonlinear optical microscopy is used in other fields such as for instance geology and material science and some of the findings in this thesis apply to those fields as well.

Even though nonlinear optical microscopes have been in development for almost forty years, I show in this work that there is still much to study about the image formation process. Using computational tools such as FDTD, cylindrical Mie theory, and the free-space Green's function, I was able to study near-field interactions at the nanoscale inside of the sample which cannot easily be done experimentally. These computational tools really form the underlying basis of my thesis. With FDTD simulations I am able to simulate Maxwell's equations without any approximations other than those resulting

from the discretization of space and time. I am therefore capable of simulating most experiments with the added benefit of full control over the experimental parameters and sample composition. FDTD is however slow and requires a large amount of computational resources. More specialized simulations such as Mie theory and the Green's function approach allow orders-of-magnitude faster simulations, thus enabling me to simulate 100,000s of experimental measurements in order to get the best statistics. I have shown that even sample composition benefits from computational physics when I generated rat and mouse tail tendon as it would occur in nature using molecular dynamics simulations.

To be able to use immediately applicable examples of my theoretical investigations, I have limited myself to three different nonlinear optical imaging modalities. The first such modality is SHG microscopy because it is a technique that is often used for the label-free imaging of collagen which in turn is a material that exists in nearly all biological matter. It plays a role in many biological processes and there still remains a lot to be understood. As such, improvements or deeper understanding of the image formation process are crucial for past and future experimental studies using SHG microscopy. The second and third modalities are SRS and CARS imaging. These are techniques that probe the vibrational spectrum of biological molecules and are thus often referred to as vibrational spectroscopic imaging. The ability to do video-rate label-free non-destructive imaging makes them an ideal candidate for studying biological processes in real-time without the need to alter the samples beforehand to apply fluorescent labels. Despite the fact that I limited myself to these three modalities, the results presented in this thesis are general and may apply to other nonlinear optical imaging techniques as well.

For SRS and CARS imaging I was able to use FDTD simulations to prove that small inhomogeneities in the refractive index can have large effects depending on size and shape of the sample. Objects act as internal microlenses and due to the third-order nature of the nonlinear SRS and CARS processes, these field enhancements are cubed in the polarization term, which causes large distortions in the far-field. Even though the inhomogeneities in the refractive index were only in the order of $\Delta n/n \approx 0.1$ — consistent with those occurring in biological material — far-field signal enhancements of an order of magnitude can occur and objects can appear shifted on the order of micrometers. Furthermore, these results break the assumption that far-field intensity scales linearly with the number of scatterers for SRS or quadratically for CARS (or linearly, depending on the concentration). Even techniques such as frequency modulation cannot reduce the aforementioned effects; it is inherent to the image formation process.

Further, I was able to show that linear index mismatch on its own can cause significant non-uniform off-resonant CARS and AM-SRS signals. The latter is especially noteworthy as AM-SRS should be background-free. These off-resonant signals were greatly reduced in FM-CARS and FM-SRS, indicating the importance of using frequency-based filtering methods, such as hyperspectral analysis or FM techniques. However, no currently known filtering techniques can reduce the signal enhancements and perceived position shifts due to microlensing. Though in future work, I will endeavour to develop techniques that would be able to detect such distortions.

I find that inhomogeneities in the refractive index also have an effect in SHG imaging of collagen fibrils, despite the fact that SHG is only a second-order process and collagen fibrils are usually too small to have an appreciable near-field enhancement effect. By using a combination of Mie theory with free-space Green's functions as well as through FDTD simulations, I show that significant changes in the backward far-field SHG signals occur due to the altering of the phase-matching conditions inside of the fibril. This in turn affects the ratio of the forward far-field intensity to the backward one, *i.e.* the F/B ratio, which is a characteristic that is often used when investigating collagen samples such as rat and mouse tail tendon. These effects predominantly become noticeable when fibrils are larger than $r = 100\,\mathrm{nm}$. These sizes occur infrequently in biological tissue. However, in typical experiments the laser focal spot contains hundreds of fibrils and thus large fibrils will be present. I generated simulated rat and mouse tail tendon samples and found that even though large fibrils were not present often, the F/B ratio for a collection of fibrils was still significantly affected by a refractive index mismatch between the fibrils and the background medium. This makes it difficult to do quantitative measurements.

These effects of the refractive index on SRS and CARS images as well as on F/B ratio measurements on collagen fibrils using SHG show that care must be taken when interpreting images from nonlinear optical microscopes. Their often coherent nature leads to destructive interference, as I showed for SHG imaging, or to near-field enhancements for which the effects are amplified because of the third-order nonlinear processes in SRS and CARS images. These results are likely not limited to the three modalities I chose to study in this work. Additionally, the objects studied with SRS and CARS were simplified to spherical particles. In real samples, the geometry will be more complicated, thus the investigations in SRS and CARS imaging in this thesis will only provide a qualitative example of the range of distortions one might encounter, whereas the investigations of fibrils and SHG imaging is more quantitative. In general one must be aware of the range

of the inhomogeneity of the refractive index in the sample as even small mismatches can has significant impact on the nonlinear far-field signals.

Computational tools do not only allow deeper insight in the image formation process to find possible sources of image distortion, but can also be used to enhance image formation. With our experimental collaborators, I have shown how computational modelling of SHG imaging of fibrillar tissue can discern subresolution features of collagen in samples of human cartilage and bone by demonstrating a clear link between the F/B ratio of the SHG signal and collagen fibril size. The fibrils of the human cartilage were small enough so that a refractive index mismatch would not cause any significant effects. By imaging equine cartilage with the interferometric SHG microscopy, which is able to discern phase information, we are also able to show the preferred fibril orientation by modelling using the standard deviation of the phase information. Finally, our model was also able to show why a speckle pattern appears in the backward direction when imaging human cornea with SHG microscopy, but not in the forward direction. The phase of the forward signal is clearly defined, leading to an overall coherent addition of signal, despite the fact that internally the collagen fibrils have either a positive or negative $\chi^{(2)}$, whereas in the backward direction the phase is random, thus destructive interference also occurs randomly and hence the speckle pattern in the SHG image in the backward direction.

Clearly phase information is important in nonlinear optical imaging, which highlights the importance of ptychography for nonlinear optical microscopy which I developed based on linear ptychography. The proposed experimental set-up is much simpler than that for interferometric nonlinear optical imaging as no reference beam is required, nor are multiple measurements at the same position needed to determine the phase of $\chi^{(n)}$ from the interference pattern; all that is needed is a CCD camera instead of a photo-multiplier tube for a raster scanning microscope. The ePIE algorithm I used is an iterative computational reconstructive algorithm that is able to reconstruct both the magnitude and phase of the nonlinear susceptibility of a sample and it does so with a resolution that approaches the diffraction limit. Furthermore, the algorithm corrects for static distortions in the input beams as the probe, which is the product of the input beams, is also reconstructed. Thus the algorithm takes these distortions in the probe into account when reconstructing the object.

I demonstrate this functionality by imaging simulated rat tail tendon using SHG and find that I can indeed approach the diffraction limit despite using a distorted input beam. Not only the magnitude of the $\chi^{(2)}$ is reconstructed, but also its phase. The

phase information allows me to determine the orientation of the simulated collagen as fibrils pointing "up" have a positive $\chi^{(2)}$ while those pointing "down" have a negative one. The reconstructed magnitude allows direct comparison with a normal SHG raster-scanning microscope with an input beam that has a radius that is a fourth of that used with ptychography. I find that my ptychographic algorithm is able to obtain higher resolution while simultaneously required an order-of-magnitude less measurements. In comparison with an interferometric SHG microscope, which additionally require roughly ten measurements per pixel to determine the phase information, the efficiency of my ptychography algorithm is two orders-of-magnitude.

In CARS imaging, the signal-to-noise ratio is always lowered due to the nonresonant background radiation, which is caused by nonresonant nonlinear processes that emit at the same frequency as the resonant CARS signal. Since a nonresonant signal is always associated with a real-valued $\chi^{(3)}$ and a resonant signal with an imaginary one, this nonresonant contribution can be reduced by using interferometric CARS. I show that I can also use the ptychographic algorithm to reduce the nonresonant background by using the reconstructed phase of $\chi^{(3)}$ to split the resonant and nonresonant components. Simultaneously I keep the two other advantages which are increased resolution and distorted input beam corrections.

As far as I am aware ptychography has not been implemented for nonlinear optical imaging before. It could have large benefits, as it provides access to the phase information of the nonlinear susceptibility, increased resolution, input beam correction, and requires less measurements than normal raster-scanning microscopes. The technique I have shown is also not limited to the two examples of SHG and CARS imaging I showed; it can easily be applied to other nonlinear optical processes by splitting the induced nonlinear polarization in the appropriate nonlinear electric susceptibility and product of input beams.

The next step would be to seek experimental verification of the theoretical work on nonlinear ptychography. We are in talks with two experimental groups that are interested in doing so. The change to the experimental set-up should be relatively straightforward as all that needs to be changed is substituting the photomultiplier tube with a CCD camera.

In future work, I would also like to extend the ptychography algorithm to 3D. Already such work exists for linear ptychography that is based on virtually dividing the sample in slices and calculating the propagation from one slice to the next until the last slice is

reached at which point the propagation to the far-field is calculated. Since that operation is reversible, guesses for each slide are updated iteratively to form a 3D reconstruction of the sample. However, this method is not directly applicable here due to the difference in how the far-field signal is generated from the sample. In linear ptychography, a transmission function is what is reconstructed, whereas in nonlinear ptychography, the input beam causes the sample to radiate. Thus each slice radiates toward the far-field, independent of the other slices. That is, the operation is not reversible. Other techniques from linear ptychography may be applicable such as tomography where the sample is rotated. However, rotating a sample while keeping track of its exact location is hard to implement experimentally. My feeling is that 3D might be possible by changing the depth of focus of the input beam, but this is still work-in-progress.

Finally, ptychography is diffraction limited because it relies on the far-field diffraction patterns. Thus higher frequency components are lost. Depending on the NA of the collecting lens or the size of the CCD, as substantial portion of the frequency domain may be captured, but full recovery is not possible. However, by using structured illumination where the input beam is encoded with an oscillating pattern in space, the missing frequency components can be captured and thus a larger diffraction pattern is created that contains the higher frequency components. This will allow me to break the diffraction limit to obtain an even higher resolution than ptychography is already capable of. This would also be applicable to linear ptychography.

Another future work will involve the newly developed Green's function approach for imaging rotated fibrils. All of the work I have presented so far has been with fibrils that are all oriented in the same direction. However this is only an approximation as in nature the fibrils will have at least some deviation from the general alignment of the collagen tissue. It will therefore be interesting to see how well this approximation holds up and if it can possibly be utilized to discover further subresolution features. As I have shown, I have already implemented the code for these types of simulations. The vectorial Green's function approach also opens up the study of polarization second harmonic generation (P-SHG), which is a technique that is often used when studying collagen tissue because it is sensitive to the dominant fibril orientation. Parameters such as disorder can be simulated to reveal their effects on far-field P-SHG signals. Diseases such as osteoarthritis for example display disorder as one of the earliest signs [155].

Of course, the effects of refractive index mismatches continues to be of interest as I have already shown that this affects SRS, CARS, and SHG imaging. Nonlinear optical

microscopes based on third harmonic generation or other nonlinear processes are probably also be affected by this. Thus it will be interesting to investigate these as well. Likewise, non-biological matter can have much larger refractive index mismatches. For example, geological samples consisting of rock and gas has been studied with CARS [156] and there may be enhancement effects there.

In conclusion, nonlinear optical microscopy is a field in which there is ample room for numerical simulation techniques to study the image formation process. The ability to control all of the parameters of the experimental set-up independently allows for fine-grained control of the nonlinear optical processes and simulations provide access to the near-fields inside of the sample at theoretically unlimited spatial and time resolution, which is only limited by the available computational resources. Those available to me are substantial as I have access to our group's own supercomputer and through the Compute Canada Consortium I also have access to those spread around Canada, such as BlueGene/Q provided by SOSCIP and the clusters at SHARCNET. Thus the computational power I was able to leverage during my Ph.D. is at a level that was unimaginable just a decade ago. However, as computational power continues to increase rapidly, a decade from now even larger simulations can be done. For this reason, I think that the field of computational nanophotonics will continue to grow in importance though it will obviously not replace experimental work. Rather it will augment it as I showed when I demonstrated the ability to obtain subresolution features by combining simulations and SHG imaging or by using algorithms such as ptychography to obtain phase information and increase resolution.

References

[1] Houle, M.A. *et al.* *Analysis of forward and backward Second Harmonic Generation images to probe the nanoscale structure of collagen within bone and cartilage.* Journal of Biophotonics, **8**(11-12):993–1001 (2015). ISSN 1864063X. http://dx.doi.org/10.1002/jbio.201500150. (Cited on pages xii, xiii, 18, 51, 52, 53, 55, 100, 107, and 112.)

[2] Couture, C.A. *et al.* *The Impact of Collagen Fibril Polarity on Second Harmonic Generation Microscopy.* Biophysical Journal, **109**(12):2501–2510 (2015). ISSN 00063495. http://dx.doi.org/10.1016/j.bpj.2015.10.040. (Cited on pages xiii, 19, 51, 56, 57, 58, 59, 86, 89, and 107.)

[3] Hook, R. *An Account of Micrographia,or the Physiological Descriptions of Minute Bodies, Made by Magnifying Glasses.* Philosophical Transactions of the Royal Society of London, **1**(1-22):27–32 (1665). ISSN 0261-0523. http://dx.doi.org/10.1098/rstl.1665.0018. (Cited on page 1.)

[4] van Leewenhoeck, A. *Observations, Communicated to the Publisher by Mr. Antony van Leewenhoeck, in a Dutch Letter of the 9th of Octob. 1676. Here English'd: concerning Little Animals by Him Observed in Rain-Well-Sea. and Snow Water; as Also in Water Wherein Pepper Had Lain Infused.* Philosophical Transactions of the Royal Society of London, **12**(133-142):821–831 (1677). ISSN 0261-0523. http://dx.doi.org/10.1098/rstl.1677.0003. (Cited on page 1.)

[5] Lister, J.J. *On Some Properties in Achromatic Object-Glasses Applicable to the Improvement of the Microscope.* Philosophical Transactions of the Royal Society of London, **120**(0):187–200 (1830). ISSN 0261-0523. http://dx.doi.org/10.1098/rstl.1830.0015. (Cited on page 2.)

[6] Zernike, v.F. *Beugungstheorie des schneidenver-fahrens und seiner verbesserten form, der phasenkontrastmethode.* Physica, **1**(7-12):689–704 (1934). ISSN 00318914. http://dx.doi.org/10.1016/S0031-8914(34)80259-5. (Cited on pages 2 and 65.)

[7] Kiernan, J.A. *Histological and histochemical methods: theory and practice*. Scion, Bloxham, 4. ed., reprinted edition (2010). ISBN 978-1-904842-42-2. OCLC: 844954638. (Cited on page 2.)

[8] Hell, S.W. and Wichmann, J. *Breaking the diffraction resolution limit by stimulated emission: stimulated-emission-depletion fluorescence microscopy*. Optics Letters, **19**(11):780 (1994). ISSN 0146-9592, 1539-4794. http://dx.doi.org/10.1364/OL.19.000780. (Cited on page 3.)

[9] Carvell, M. *et al. The influence of labelling mechanisms on the fluorescence behaviour of polymers bearing fluorescein labels*. Polymer, **39**(2):393–398 (1998). ISSN 00323861. http://dx.doi.org/10.1016/S0032-3861(97)00283-8. (Cited on page 3.)

[10] Mučibabić, M. *et al. The effect of fluorescent labeling on α-synuclein fibril morphology*. Biochimica et Biophysica Acta (BBA) - Proteins and Proteomics, **1864**(10):1419–1427 (2016). ISSN 15709639. http://dx.doi.org/10.1016/j.bbapap.2016.07.007. (Cited on page 3.)

[11] Chen, X. *et al. Second harmonic generation microscopy for quantitative analysis of collagen fibrillar structure*. Nature Protocols, **7**(4):654–669 (2012). ISSN 1754-2189, 1750-2799. http://dx.doi.org/10.1038/nprot.2012.009. (Cited on pages 4 and 6.)

[12] Pawley, J.B., editor. *Handbook of biological confocal microscopy*. Springer, New York, NY, 3rd ed edition (2006). ISBN 978-0-387-25921-5. (Cited on page 4.)

[13] Franken, P.A. *et al. Generation of Optical Harmonics*. Physical Review Letters, **7**(4):118–119 (1961). ISSN 0031-9007. http://dx.doi.org/10.1103/PhysRevLett.7.118. (Cited on page 4.)

[14] Boyd, R.W. *Nonlinear optics*. Academic Press, Amsterdam ; Boston, 3rd ed edition (2008). ISBN 978-0-12-369470-6. (Cited on pages 4, 6, 9, 11, 41, 56, and 67.)

[15] Freund, I. *et al. Connective tissue polarity. Optical second-harmonic microscopy, crossed-beam summation, and small-angle scattering in rat-tail tendon*. Biophysical Journal, **50**(4):693–712 (1986). ISSN 00063495. http://dx.doi.org/10.1016/S0006-3495(86)83510-X. (Cited on pages 4, 6, 7, 18, 99, 101, and 112.)

[16] Barad, Y. *et al. Nonlinear scanning laser microscopy by third harmonic generation.* Applied Physics Letters, **70**(8):922 (1997). ISSN 00036951. http://dx.doi.org/10.1063/1.118442. (Cited on pages 4 and 6.)

[17] Cheng, J.X. and Xie, X.S., editors. *Coherent Raman scattering microscopy.* Series in cellular and clinical imaging. CRC Press, Taylor & Francis Group, Boca Raton (2013). ISBN 978-1-4398-6765-5. (Cited on pages 4, 11, and 13.)

[18] Freudiger, C.W. *et al. Label-Free Biomedical Imaging with High Sensitivity by Stimulated Raman Scattering Microscopy.* Science, **322**(5909):1857–1861 (2008). ISSN 0036-8075, 1095-9203. http://dx.doi.org/10.1126/science.1165758. (Cited on page 4.)

[19] Denk, W. *et al. Two-photon laser scanning fluorescence microscopy.* Science, **248**(4951):73–76 (1990). ISSN 0036-8075, 1095-9203. http://dx.doi.org/10.1126/science.2321027. (Cited on page 4.)

[20] Campagnola, P.J. and Loew, L.M. *Second-harmonic imaging microscopy for visualizing biomolecular arrays in cells, tissues and organisms.* Nature Biotechnology, **21**(11):1356–1360 (2003). ISSN 1087-0156. http://dx.doi.org/10.1038/nbt894. (Cited on page 5.)

[21] Sacconi, L. *et al. Overcoming photodamage in second-harmonic generation microscopy: Real-time optical recording of neuronal action potentials.* Proceedings of the National Academy of Sciences, **103**(9):3124–3129 (2006). ISSN 0027-8424, 1091-6490. http://dx.doi.org/10.1073/pnas.0511338103. (Cited on page 5.)

[22] Armstrong, J.A. *et al. Interactions between Light Waves in a Nonlinear Dielectric.* Physical Review, **127**(6):1918–1939 (1962). ISSN 0031-899X. http://dx.doi.org/10.1103/PhysRev.127.1918. (Cited on page 6.)

[23] Shen, Y.R. *Surface properties probed by second-harmonic and sum-frequency generation.* Nature, **337**(6207):519–525 (1989). ISSN 0028-0836. http://dx.doi.org/10.1038/337519a0. (Cited on page 6.)

[24] Helmchen, F. and Denk, W. *Deep tissue two-photon microscopy.* Nature Methods, **2**(12):932–940 (2005). ISSN 1548-7091, 1548-7105. http://dx.doi.org/10.1038/nmeth818. (Cited on page 6.)

[25] Provenzano, P.P. *et al.* *Collagen reorganization at the tumor-stromal interface facilitates local invasion.* BMC Medicine, **4**(1) (2006). ISSN 1741-7015. http://dx.doi.org/10.1186/1741-7015-4-38. (Cited on page 6.)

[26] Szu-Yu Chen *et al.* *In Vivo Virtual Biopsy of Human Skin by Using Noninvasive Higher Harmonic Generation Microscopy.* IEEE Journal of Selected Topics in Quantum Electronics, **16**(3):478–492 (2010). ISSN 1077-260X, 1558-4542. http://dx.doi.org/10.1109/JSTQE.2009.2031987. (Cited on page 7.)

[27] Vuillemin, N. *et al.* *Efficient second-harmonic imaging of collagen in histological slides using Bessel beam excitation.* Scientific Reports, **6**:29863 (2016). ISSN 2045-2322. http://dx.doi.org/10.1038/srep29863. (Cited on page 7.)

[28] Morishige, N. *et al.* *Three-Dimensional Analysis of Collagen Lamellae in the Anterior Stroma of the Human Cornea Visualized by Second Harmonic Generation Imaging Microscopy.* Investigative Opthalmology & Visual Science, **52**(2):911 (2011). ISSN 1552-5783. http://dx.doi.org/10.1167/iovs.10-5657. (Cited on page 7.)

[29] Latour, G. *et al.* *In vivo structural imaging of the cornea by polarization-resolved second harmonic microscopy.* Biomedical Optics Express, **3**(1):1 (2012). ISSN 2156-7085, 2156-7085. http://dx.doi.org/10.1364/BOE.3.000001. (Cited on pages 7 and 61.)

[30] Petroll, W.M. *et al.* *Corneal Fibroblast Migration Patterns During Intrastromal Wound Healing Correlate With ECM Structure and Alignment.* Investigative Opthalmology & Visual Science, **56**(12):7352 (2015). ISSN 1552-5783. http://dx.doi.org/10.1167/iovs.15-17978. (Cited on page 7.)

[31] Bersohn, R. *et al.* *Double-Quantum Light Scattering by Molecules.* The Journal of Chemical Physics, **45**(9):3184–3198 (1966). ISSN 0021-9606, 1089-7690. http://dx.doi.org/10.1063/1.1728092. (Cited on page 7.)

[32] Mertz, J. and Moreaux, L. *Second-harmonic generation by focused excitation of inhomogeneously distributed scatterers.* Optics Communications, **196**(1–6):325 – 330 (2001). ISSN 0030-4018. http://dx.doi.org/10.1016/S0030-4018(01)01403-1. (Cited on pages 7 and 100.)

[33] Teulon, C. *et al.* *Theoretical, numerical and experimental study of geometrical parameters that affect anisotropy measurements in polarization-resolved SHG microscopy.* Optics Express, **23**(7):9313 (2015). ISSN 1094-4087. http://dx.doi.org/10.1364/OE.23.009313. (Cited on page 7.)

[34] Gusachenko, I. *et al.* *Polarization-resolved Second Harmonic microscopy in anisotropic thick tissues.* Optics Express, **18**(18):19339 (2010). ISSN 1094-4087. http://dx.doi.org/10.1364/OE.18.019339. (Cited on page 7.)

[35] Wasik, V. *et al.* *Precision of polarization-resolved second harmonic generation microscopy limited by photon noise for samples with cylindrical symmetry.* Journal of the Optical Society of America A, **32**(8):1437 (2015). ISSN 1084-7529, 1520-8532. http://dx.doi.org/10.1364/JOSAA.32.001437. (Cited on page 7.)

[36] Wasik, V. *et al.* *Detection of imprecise estimations for polarization-resolved second-harmonic generation microscopy.* Journal of the Optical Society of America A, **33**(7):1353 (2016). ISSN 1084-7529, 1520-8532. http://dx.doi.org/10.1364/JOSAA.33.001353. (Cited on page 7.)

[37] Lodish, H.F., editor. *Molecular cell biology.* W.H. Freeman, New York, 4th ed edition (2000). ISBN 978-0-7167-3136-8. (Cited on pages 7, 8, 52, and 61.)

[38] Gautieri, A. *et al.* *Hierarchical Structure and Nanomechanics of Collagen Microfibrils from the Atomistic Scale Up.* Nano Letters, **11**(2):757–766 (2011). ISSN 1530-6984, 1530-6992. http://dx.doi.org/10.1021/nl103943u. (Cited on pages 8, 86, and 99.)

[39] Meyers, M.A. *et al.* *Structural Biological Materials: Critical Mechanics-Materials Connections.* Science, **339**(6121):773–779 (2013). ISSN 0036-8075, 1095-9203. http://dx.doi.org/10.1126/science.1220854. (Cited on page 8.)

[40] Yang, W. *et al.* *On the tear resistance of skin.* Nature Communications, **6**:6649 (2015). ISSN 2041-1723. http://dx.doi.org/10.1038/ncomms7649. (Cited on page 8.)

[41] Wang, Y. *et al.* *The predominant role of collagen in the nucleation, growth, structure and orientation of bone apatite.* Nature Materials, **11**(8):724–733 (2012). ISSN 1476-1122, 1476-4660. http://dx.doi.org/10.1038/nmat3362. (Cited on page 8.)

[42] Nair, A.K. *et al. Molecular mechanics of mineralized collagen fibrils in bone*. Nature Communications, **4**:1724 (2013). ISSN 2041-1723. http://dx.doi.org/10.1038/ncomms2720. (Cited on page 8.)

[43] Trappmann, B. *et al. Extracellular-matrix tethering regulates stem-cell fate*. Nature Materials, **11**(7):642–649 (2012). ISSN 1476-1122, 1476-4660. http://dx.doi.org/10.1038/nmat3339. (Cited on page 8.)

[44] Daxer, A. *et al. Collagen fibrils in the human corneal stroma: structure and aging*. Investigative Ophthalmology & Visual Science, **39**(3):644–648 (1998). ISSN 1552-5783. (Cited on page 8.)

[45] Bloembergen, N. and Pershan, P.S. *Light Waves at the Boundary of Nonlinear Media*. Physical Review, **128**(2):606–622 (1962). ISSN 0031-899X. http://dx.doi.org/10.1103/PhysRev.128.606. (Cited on page 10.)

[46] Raman, C.V. and Krishnan, K.S. *Molecular Spectra in the Extreme Infra-Red*. Nature, **122**(3069):278–278 (1928). ISSN 0028-0836. http://dx.doi.org/10.1038/122278a0. (Cited on page 10.)

[47] Szymanski, H.A. *Raman Spectroscopy: Theory and Practice*. Springer US, Boston, MA (1967). ISBN 978-1-4684-3024-0 978-1-4684-3026-4. http://dx.doi.org/10.1007/978-1-4684-3024-0. OCLC: 840288093. (Cited on page 10.)

[48] Camp Jr, C.H. *et al. High-speed coherent Raman fingerprint imaging of biological tissues*. Nature Photonics, **8**(8):627–634 (2014). ISSN 1749-4885, 1749-4893. http://dx.doi.org/10.1038/nphoton.2014.145. (Cited on pages 10 and 64.)

[49] Maker, P.D. and Terhune, R.W. *Study of Optical Effects Due to an Induced Polarization Third Order in the Electric Field Strength*. Physical Review, **137**(3A):A801–A818 (1965). ISSN 0031-899X. http://dx.doi.org/10.1103/PhysRev.137.A801. (Cited on page 11.)

[50] Duncan, M.D. *et al. Scanning coherent anti-Stokes Raman microscope*. Optics Letters, **7**(8):350 (1982). ISSN 0146-9592, 1539-4794. http://dx.doi.org/10.1364/OL.7.000350. (Cited on page 11.)

[51] Evans, C.L. *et al. Chemical imaging of tissue in vivo with video-rate coherent anti-Stokes Raman scattering microscopy*. Proceedings of the National Academy of

Sciences, **102**(46):16807–16812 (2005). ISSN 0027-8424, 1091-6490. http://dx.doi.org/10.1073/pnas.0508282102. (Cited on pages 11, 64, and 90.)

[52] Ploetz, E. *et al.* *Femtosecond stimulated Raman microscopy.* Applied Physics B, **87**(3):389–393 (2007). ISSN 0946-2171, 1432-0649. http://dx.doi.org/10.1007/s00340-007-2630-x. (Cited on page 11.)

[53] Bloembergen, N. *The Stimulated Raman Effect.* American Journal of Physics, **35**(11):989–1023 (1967). ISSN 0002-9505, 1943-2909. http://dx.doi.org/10.1119/1.1973774. (Cited on page 11.)

[54] Saar, B.G. *et al.* *Video-Rate Molecular Imaging in Vivo with Stimulated Raman Scattering.* Science, **330**(6009):1368–1370 (2010). ISSN 0036-8075, 1095-9203. http://dx.doi.org/10.1126/science.1197236. (Cited on pages 11, 64, and 90.)

[55] Ozeki, Y. *et al.* *High-speed molecular spectral imaging of tissue with stimulated Raman scattering.* Nature Photonics, **6**(12):845–851 (2012). ISSN 1749-4885, 1749-4893. http://dx.doi.org/10.1038/nphoton.2012.263. (Cited on pages 11, 64, 65, and 90.)

[56] Lyn, R.K. *et al.* *Direct imaging of the disruption of hepatitis C virus replication complexes by inhibitors of lipid metabolism.* Virology, **394**(1):130–142 (2009). ISSN 00426822. http://dx.doi.org/10.1016/j.virol.2009.08.022. (Cited on page 11.)

[57] Huff, T. and Cheng, J.X. *In vivo coherent anti-Stokes Raman scattering imaging of sciatic nerve tissue.* Journal of Microscopy, **225**(2):175–182 (2007). ISSN 0022-2720, 1365-2818. http://dx.doi.org/10.1111/j.1365-2818.2007.01729.x. (Cited on page 11.)

[58] Fu, Y. *et al.* *Coherent anti-stokes Raman scattering imaging of myelin degradation reveals a calcium-dependent pathway in lyso-PtdCho-induced demyelination.* Journal of Neuroscience Research, **85**(13):2870–2881 (2007). ISSN 03604012, 10974547. http://dx.doi.org/10.1002/jnr.21403. (Cited on page 11.)

[59] Evans, C.L. *et al.* *Chemically-selective imaging of brain structures with CARS microscopy.* Optics Express, **15**(19):12076 (2007). ISSN 1094-4087. http://dx.doi.org/10.1364/OE.15.012076. (Cited on page 11.)

[60] Wang, H.W. *et al.* *Label-free imaging of arterial cells and extracellular matrix using a multimodal CARS microscope.* Optics Communications, **281**(7):1813–1822 (2008). ISSN 00304018. http://dx.doi.org/10.1016/j.optcom.2007.07.067. (Cited on page 11.)

[61] Meyer, T. *et al.* *Three-Dimensional Molecular Mapping of a Multiple Emulsion by Means of CARS Microscopy.* The Journal of Physical Chemistry B, **112**(5):1420–1426 (2008). ISSN 1520-6106, 1520-5207. http://dx.doi.org/10.1021/jp709643h. (Cited on page 11.)

[62] Wei, L. *et al.* *Live-cell imaging of alkyne-tagged small biomolecules by stimulated Raman scattering.* Nature Methods, **11**(4):410–412 (2014). ISSN 1548-7091, 1548-7105. http://dx.doi.org/10.1038/nmeth.2878. (Cited on pages 11 and 65.)

[63] Fu, D. *et al.* *Imaging the intracellular distribution of tyrosine kinase inhibitors in living cells with quantitative hyperspectral stimulated Raman scattering.* Nature Chemistry, **6**(7):614–622 (2014). ISSN 1755-4330, 1755-4349. http://dx.doi.org/10.1038/nchem.1961. (Cited on pages 11 and 65.)

[64] Ji, M. *et al.* *Rapid, Label-Free Detection of Brain Tumors with Stimulated Raman Scattering Microscopy.* Science Translational Medicine, **5**(201):201ra119–201ra119 (2013). ISSN 1946-6234, 1946-6242. http://dx.doi.org/10.1126/scitranslmed.3005954. (Cited on pages 11 and 65.)

[65] Wei, L. *et al.* *Vibrational imaging of newly synthesized proteins in live cells by stimulated Raman scattering microscopy.* Proceedings of the National Academy of Sciences, **110**(28):11226–11231 (2013). ISSN 0027-8424, 1091-6490. http://dx.doi.org/10.1073/pnas.1303768110. (Cited on pages 11 and 65.)

[66] Cheng, J.X. *et al.* *Theoretical and experimental characterization of coherent anti-Stokes Raman scattering microscopy.* Journal of the Optical Society of America B, **19**(6):1363 (2002). ISSN 0740-3224, 1520-8540. http://dx.doi.org/10.1364/JOSAB.19.001363. (Cited on page 11.)

[67] Penzkofer, A. *et al.* *High intensity Raman interactions.* Progress in Quantum Electronics, **6**(2):55–140 (1979). ISSN 00796727. http://dx.doi.org/10.1016/0079-6727(79)90011-9. (Cited on page 12.)

[68] Mostowski, J. and Raymer, M. *The buildup of stimulated Raman scattering from spontaneous Raman scattering.* Optics Communications, **36**(3):237–240 (1981). ISSN 00304018. http://dx.doi.org/10.1016/0030-4018(81)90366-7. (Cited on page 12.)

[69] Popov, K.I. *et al. Image formation in CARS microscopy: effect of the Gouy phase shift.* Optics Express, **19**(7):5902 (2011). ISSN 1094-4087. http://dx.doi.org/10.1364/OE.19.005902. (Cited on pages 12, 65, 66, 67, 69, and 73.)

[70] Popov, K.I. *et al. Image formation in CARS and SRS: effect of an inhomogeneous nonresonant background medium.* Optics Letters, **37**(4):473 (2012). ISSN 0146-9592, 1539-4794. http://dx.doi.org/10.1364/OL.37.000473. (Cited on pages 12, 65, 68, and 73.)

[71] Weinigel, M. *et al. Impact of refractive index mismatches on coherent anti-Stokes Raman scattering and multiphoton autofluorescence tomography of human skin in vivo.* Physics in Medicine and Biology, **60**(17):6881–6899 (2015). ISSN 0031-9155, 1361-6560. http://dx.doi.org/10.1088/0031-9155/60/17/6881. (Cited on pages 12 and 65.)

[72] Liu, C. *et al. Near-field effects on coherent anti-Stokes Raman scattering microscopy imaging.* Optics Express, **15**(7):4118 (2007). ISSN 1094-4087. http://dx.doi.org/10.1364/OE.15.004118. (Cited on pages 12 and 65.)

[73] Lin, J. *et al. Numerical study of effects of light polarization, scatterer sizes and orientations on near-field coherent anti-Stokes Raman scattering microscopy.* Optics Express, **17**(4):2423 (2009). ISSN 1094-4087. http://dx.doi.org/10.1364/OE.17.002423. (Cited on pages 12 and 65.)

[74] Xie, X.S. *et al. Coherent Anti-Stokes Raman Scattering Microscopy.* In J.B. Pawley, editor, *Handbook Of Biological Confocal Microscopy*, pages 595–606. Springer US, Boston, MA (2006). ISBN 978-0-387-25921-5 978-0-387-45524-2. http://link.springer.com/10.1007/978-0-387-45524-2_33. DOI: 10.1007/978-0-387-45524-2_33. (Cited on page 13.)

[75] Liu, Y. *et al. Broadband CARS spectral phase retrieval using a time-domain Kramers–Kronig transform.* Optics Letters, **34**(9):1363 (2009). ISSN 0146-9592,

1539-4794. http://dx.doi.org/10.1364/OL.34.001363. (Cited on pages 14 and 15.)

[76] Barlow, A.M. *et al.* *Spatial-spectral coupling in coherent anti-Stokes Raman scattering microscopy.* Optics Express, **21**(13):15298 (2013). ISSN 1094-4087. http://dx.doi.org/10.1364/OE.21.015298. (Cited on pages 14 and 65.)

[77] Pegoraro, A.F. *et al.* *Hyperspectral multimodal CARS microscopy in the fingerprint region: Hyperspectral multimodal CARS microscopy in the fingerprint region.* Journal of Biophotonics, **7**(1-2):49–58 (2014). ISSN 1864063X. http://dx.doi.org/10.1002/jbio.201200171. (Cited on pages 14, 15, 64, and 90.)

[78] Cheng, J.X. and Xie, X.S. *Vibrational spectroscopic imaging of living systems: An emerging platform for biology and medicine.* Science, **350**(6264):aaa8870–aaa8870 (2015). ISSN 0036-8075, 1095-9203. http://dx.doi.org/10.1126/science.aaa8870. (Cited on pages 14, 64, and 90.)

[79] Lu, F.K. *et al.* *Label-free DNA imaging in vivo with stimulated Raman scattering microscopy.* Proceedings of the National Academy of Sciences, **112**(37):11624–11629 (2015). ISSN 0027-8424, 1091-6490. http://dx.doi.org/10.1073/pnas.1515121112. (Cited on page 14.)

[80] Potma, E.O. *et al.* *Heterodyne coherent anti-Stokes Raman scattering (CARS) imaging.* Optics Letters, **31**(2):241 (2006). ISSN 0146-9592, 1539-4794. http://dx.doi.org/10.1364/OL.31.000241. (Cited on pages 14, 90, and 91.)

[81] Cheng, J.x. *et al.* *An Epi-Detected Coherent Anti-Stokes Raman Scattering (E-CARS) Microscope with High Spectral Resolution and High Sensitivity.* The Journal of Physical Chemistry B, **105**(7):1277–1280 (2001). ISSN 1520-6106, 1520-5207. http://dx.doi.org/10.1021/jp003774a. (Cited on page 15.)

[82] Légaré, F. *et al.* *Towards CARS Endoscopy.* Optics Express, **14**(10):4427 (2006). ISSN 1094-4087. http://dx.doi.org/10.1364/OE.14.004427. (Cited on page 15.)

[83] Ganikhanov, F. *et al.* *High-sensitivity vibrational imaging with frequency modulation coherent anti-Stokes Raman scattering (FM CARS) microscopy.* Optics Letters, **31**(12):1872 (2006). ISSN 0146-9592, 1539-4794. http://dx.doi.org/10.1364/OL.31.001872. (Cited on pages 15, 90, and 92.)

[84] Cheng, J.X. *et al. Polarization coherent anti-Stokes Raman scattering microscopy.* Optics Letters, **26**(17):1341 (2001). ISSN 0146-9592, 1539-4794. http://dx.doi.org/10.1364/OL.26.001341. (Cited on page 15.)

[85] Taflove, A. *Computational electrodynamics: the finite-difference time-domain method.* Artech House, Boston (1995). ISBN 978-0-89006-792-5. (Cited on pages 17 and 33.)

[86] Kane Yee. *Numerical solution of initial boundary value problems involving maxwell's equations in isotropic media.* IEEE Transactions on Antennas and Propagation, **14**(3):302–307 (1966). ISSN 0018-926X. http://dx.doi.org/10.1109/TAP.1966.1138693. (Cited on pages 17 and 25.)

[87] Mur, G. *Absorbing Boundary Conditions for the Finite-Difference Approximation of the Time-Domain Electromagnetic-Field Equations.* IEEE Transactions on Electromagnetic Compatibility, **EMC-23**(4):377–382 (1981). ISSN 0018-9375. http://dx.doi.org/10.1109/TEMC.1981.303970. (Cited on pages 17, 25, 33, and 35.)

[88] Taflove, A. *et al.*, editors. *Advances in FDTD computational electrodynamics: photonics and nanotechnology.* Artech House, Boston (2013). ISBN 978-1-60807-170-8. OCLC: 811964793. (Cited on page 17.)

[89] Hellwarth, R. *Third-order optical susceptibilities of liquids and solids.* Progress in Quantum Electronics, **5**:1–68 (1977). ISSN 00796727. http://dx.doi.org/10.1016/0079-6727(79)90002-8. (Cited on pages 17 and 30.)

[90] van der Kolk, J. *et al. Effects of refractive index mismatch on SRS and CARS microscopy.* Optics Express, **24**(22):25752 (2016). ISSN 1094-4087. http://dx.doi.org/10.1364/OE.24.025752. (Cited on pages 18 and 64.)

[91] Rodenburg, J. *Ptychography and Related Diffractive Imaging Methods.* In *Advances in Imaging and Electron Physics*, volume 150, pages 87–184. Elsevier (2008). ISBN 978-0-12-374217-9. http://linkinghub.elsevier.com/retrieve/pii/S1076567007000031. (Cited on pages 19, 84, and 92.)

[92] Maiden, A.M. *et al. Superresolution imaging via ptychography.* Journal of the Optical Society of America A, **28**(4):604 (2011). ISSN 1084-7529, 1520-8532. http://dx.doi.org/10.1364/JOSAA.28.000604. (Cited on page 19.)

[93] Moore, G.E. *Cramming more components onto integrated circuits.* Electronics, **38**(8) (1965). (Cited on page 23.)

[94] Taflove, A. *Application of the Finite-Difference Time-Domain Method to Sinusoidal Steady-State Electromagnetic-Penetration Problems.* IEEE Transactions on Electromagnetic Compatibility, **EMC-22**(3):191–202 (1980). ISSN 0018-9375. http://dx.doi.org/10.1109/TEMC.1980.303879. (Cited on page 25.)

[95] Berenger, J.P. *A perfectly matched layer for the absorption of electromagnetic waves.* Journal of Computational Physics, **114**(2):185–200 (1994). ISSN 00219991. http://dx.doi.org/10.1006/jcph.1994.1159. (Cited on page 25.)

[96] Griffiths, D.J. *Introduction to electrodynamics.* Prentice Hall, Upper Saddle River, N.J, 3rd ed edition (1999). ISBN 978-0-13-805326-0. (Cited on page 26.)

[97] Fujii, M. *et al. High-Order FDTD and Auxiliary Differential Equation Formulation of Optical Pulse Propagation in 2-D Kerr and Raman Nonlinear Dispersive Media.* IEEE Journal of Quantum Electronics, **40**(2):175–182 (2004). ISSN 0018-9197. http://dx.doi.org/10.1109/JQE.2003.821881. (Cited on pages 31 and 67.)

[98] Andrew, W. *et al. A comparison of the Berenger perfectly matched layer and the Lindman higher-order ABC's for the FDTD method.* IEEE Microwave and Guided Wave Letters, **5**(6):192–194 (1995). ISSN 10518207. http://dx.doi.org/10.1109/75.386128. (Cited on page 36.)

[99] Jackson, J.D. *Classical electrodynamics.* Wiley, New York, 3rd ed edition (1999). ISBN 978-0-471-30932-1. (Cited on pages 38 and 113.)

[100] Erikson, A. *et al. Quantification of the second-order nonlinear susceptibility of collagen I using a laser scanning microscope.* Journal of Biomedical Optics, **12**(4):044002 (2007). ISSN 10833668. http://dx.doi.org/10.1117/1.2772311. (Cited on pages 41 and 113.)

[101] Mie, G. *Beiträge zur Optik trüber Medien, speziell kolloidaler Metallösungen.* Annalen der Physik, **330**(3):377–445 (1908). ISSN 00033804, 15213889. http://dx.doi.org/10.1002/andp.19083300302. (Cited on page 44.)

[102] Stratton, J.A. *Electromagnetic theory.* McGraw-Hill Book Company, New York and London (1941). ISBN 978-0-470-13153-4. (Cited on pages 44 and 113.)

[103] Hulst, H.C.v.d. *Light scattering by small particles*. Dover Publications, New York (1981). ISBN 978-0-486-13975-3. http://www.freading.com/ebooks/details/r:download/ZnJlYWQ6OTc4MDQ4NjEzOTc1Mzpl. OCLC: 829166958. (Cited on pages 44 and 45.)

[104] Bohren, C.F. and Huffman, D.R., editors. *Absorption and Scattering of Light by Small Particles*. Wiley-VCH Verlag GmbH, Weinheim, Germany (1998). ISBN 978-3-527-61815-6 978-0-471-29340-8. http://doi.wiley.com/10.1002/9783527618156. (Cited on page 44.)

[105] Duffy, D.G. *Green's functions with applications*. Advances in applied mathematics. CRC Press, Taylor & Francis Group, Boca Raton, second edition edition (2015). ISBN 978-1-4822-5102-9. (Cited on page 46.)

[106] Parry, D.A.D. and Craig, A.S. *Quantitative electron microscope observations of the collagen fibrils in rat-tail tendon*. Biopolymers, **16**(5):1015–1031 (1977). ISSN 0006-3525, 1097-0282. http://dx.doi.org/10.1002/bip.1977.360160506. (Cited on pages 47, 48, 86, 103, 105, and 116.)

[107] Rivard, M. *et al. Imaging the noncentrosymmetric structural organization of tendon with Interferometric Second Harmonic Generation microscopy: Tissue imaging with Interferometric Second Harmonic Generation microscopy*. Journal of Biophotonics, **7**(8):638–646 (2014). ISSN 1864063X. http://dx.doi.org/10.1002/jbio.201300036. (Cited on pages 47, 48, 86, 87, 105, 107, and 116.)

[108] Harnagea, C. *et al. Two-Dimensional Nanoscale Structural and Functional Imaging in Individual Collagen Type I Fibrils*. Biophysical Journal, **98**(12):3070–3077 (2010). ISSN 00063495. http://dx.doi.org/10.1016/j.bpj.2010.02.047. (Cited on pages 47 and 56.)

[109] Frenkel, D. and Smit, B. *Understanding molecular simulation: from algorithms to applications*. Number 1 in Computational science series. Academic Press, San Diego, 2nd ed edition (2002). ISBN 978-0-12-267351-1. (Cited on page 49.)

[110] Hughes, L. *et al. The ultrastructure of mouse articular cartilage: Collagen orientation and implications for tissue functionality. A polarised light and scanning electron microscope study and review*. European Cells and Materials, **9**:68–84 (2005). http://dx.doi.org/10.22203/eCM.v009a09. (Cited on page 55.)

[111] Minns, R.J. and Steven, F.S. *The collagen fibril organization in human articular cartilage.* Journal of Anatomy, **123**(Pt 2):437–457 (1977). ISSN 0021-8782. (Cited on page 55.)

[112] Stoller, P. *et al. Quantitative second-harmonic generation microscopy in collagen.* Applied Optics, **42**(25):5209 (2003). ISSN 0003-6935, 1539-4522. http://dx.doi.org/10.1364/AO.42.005209. (Cited on pages 56 and 86.)

[113] Rabinowitz, Y.S. *Keratoconus.* Survey of Ophthalmology, **42**(4):297–319 (1998). ISSN 0039-6257. (Cited on page 61.)

[114] Hassell, J.R. and Birk, D.E. *The molecular basis of corneal transparency.* Experimental Eye Research, **91**(3):326–335 (2010). ISSN 00144835. http://dx.doi.org/10.1016/j.exer.2010.06.021. (Cited on page 61.)

[115] Tuft, S.J. *et al. Photorefractive keratectomy: implications of corneal wound healing.* British Journal of Ophthalmology, **77**(4):243–247 (1993). ISSN 0007-1161. http://dx.doi.org/10.1136/bjo.77.4.243. (Cited on page 61.)

[116] Morishige, N. *et al. Second-Harmonic Imaging Microscopy of Normal Human and Keratoconus Cornea.* Investigative Opthalmology & Visual Science, **48**(3):1087 (2007). ISSN 1552-5783. http://dx.doi.org/10.1167/iovs.06-1177. (Cited on page 61.)

[117] Plamann, K. *et al. Ultrashort pulse laser surgery of the cornea and the sclera.* Journal of Optics, **12**(8):084002 (2010). ISSN 2040-8978, 2040-8986. http://dx.doi.org/10.1088/2040-8978/12/8/084002. (Cited on page 61.)

[118] Cicchi, R. *et al. From molecular structure to tissue architecture: collagen organization probed by SHG microscopy.* Journal of Biophotonics, **6**(2):129–142 (2013). ISSN 1864063X. http://dx.doi.org/10.1002/jbio.201200092. (Cited on page 61.)

[119] Min, W. *et al. Coherent Nonlinear Optical Imaging: Beyond Fluorescence Microscopy.* Annual Review of Physical Chemistry, **62**(1):507–530 (2011). ISSN 0066-426X, 1545-1593. http://dx.doi.org/10.1146/annurev.physchem.012809.103512. (Cited on pages 64 and 90.)

[120] Zhang, X. *et al. Label-Free Live-Cell Imaging of Nucleic Acids Using Stimulated Raman Scattering Microscopy.* ChemPhysChem, **13**(4):1054–1059 (2012). ISSN 14394235. http://dx.doi.org/10.1002/cphc.201100890. (Cited on page 65.)

[121] Djaker, N. *et al. Refractive effects in coherent anti-Stokes Raman scattering microscopy.* Applied Optics, **45**(27):7005 (2006). ISSN 0003-6935, 1539-4522. http://dx.doi.org/10.1364/AO.45.007005. (Cited on page 65.)

[122] Ferrand, P. *et al. Direct imaging of photonic nanojets.* Optics Express, **16**(10):6930 (2008). ISSN 1094-4087. http://dx.doi.org/10.1364/OE.16.006930. (Cited on pages 65 and 69.)

[123] Upputuri, P.K. *et al. Super-resolution coherent anti-Stokes Raman scattering microscopy with photonic nanojets.* Optics Express, **22**(11):12890 (2014). ISSN 1094-4087. http://dx.doi.org/10.1364/OE.22.012890. (Cited on page 66.)

[124] Rodenburg, J. *et al. Transmission microscopy without lenses for objects of unlimited size.* Ultramicroscopy, **107**(2-3):227–231 (2007). ISSN 03043991. http://dx.doi.org/10.1016/j.ultramic.2006.07.007. (Cited on page 84.)

[125] Maiden, A.M. and Rodenburg, J.M. *An improved ptychographical phase retrieval algorithm for diffractive imaging.* Ultramicroscopy, **109**(10):1256–1262 (2009). ISSN 03043991. http://dx.doi.org/10.1016/j.ultramic.2009.05.012. (Cited on pages 84 and 92.)

[126] Hoppe, W. *Beugung im inhomogenen Primärstrahlwellenfeld. III. Amplituden- und Phasenbestimmung bei unperiodischen Objekten.* Acta Crystallographica Section A, **25**(4):508–514 (1969). ISSN 0567-7394. http://dx.doi.org/10.1107/S0567739469001069. (Cited on page 84.)

[127] Hegerl, R. and Hoppe, W. *Dynamische Theorie der Kristallstrukturanalyse durch Elektronenbeugung im inhomogenen Primärstrahlwellenfeld.* Berichte der Bunsengesellschaft für physikalische Chemie, **74**(11):1148–1154 (1970). ISSN 00059021. http://dx.doi.org/10.1002/bbpc.19700741112. (Cited on page 84.)

[128] Nellist, P. and Rodenburg, J. *Beyond the conventional information limit: the relevant coherence function.* Ultramicroscopy, **54**(1):61–74 (1994). ISSN 03043991. http://dx.doi.org/10.1016/0304-3991(94)90092-2. (Cited on page 84.)

[129] Rodenburg, J.M. and Faulkner, H.M.L. *A phase retrieval algorithm for shifting illumination*. Applied Physics Letters, **85**(20):4795–4797 (2004). ISSN 0003-6951, 1077-3118. http://dx.doi.org/10.1063/1.1823034. (Cited on page 84.)

[130] Marrison, J. *et al. Ptychography – a label free, high-contrast imaging technique for live cells using quantitative phase information*. Scientific Reports, **3** (2013). ISSN 2045-2322. http://dx.doi.org/10.1038/srep02369. (Cited on page 84.)

[131] Giewekemeyer, K. *et al. Quantitative biological imaging by ptychographic x-ray diffraction microscopy*. Proceedings of the National Academy of Sciences, **107**(2):529–534 (2010). ISSN 0027-8424, 1091-6490. http://dx.doi.org/10.1073/pnas.0905846107. (Cited on page 84.)

[132] Dierolf, M. *et al. Ptychographic X-ray computed tomography at the nanoscale*. Nature, **467**(7314):436–439 (2010). ISSN 0028-0836, 1476-4687. http://dx.doi.org/10.1038/nature09419. (Cited on page 84.)

[133] Deng, J. *et al. Simultaneous cryo X-ray ptychographic and fluorescence microscopy of green algae*. Proceedings of the National Academy of Sciences, **112**(8):2314–2319 (2015). ISSN 0027-8424, 1091-6490. http://dx.doi.org/10.1073/pnas.1413003112. (Cited on page 84.)

[134] Holler, M. *et al. X-ray ptychographic computed tomography at 16 nm isotropic 3D resolution*. Scientific Reports, **4** (2014). ISSN 2045-2322. http://dx.doi.org/10.1038/srep03857. (Cited on page 84.)

[135] Shapiro, D.A. *et al. Chemical composition mapping with nanometre resolution by soft X-ray microscopy*. Nature Photonics, **8**(10):765–769 (2014). ISSN 1749-4885, 1749-4893. http://dx.doi.org/10.1038/nphoton.2014.207. (Cited on page 84.)

[136] Humphry, M. *et al. Ptychographic electron microscopy using high-angle dark-field scattering for sub-nanometre resolution imaging*. Nature Communications, **3**:730 (2012). ISSN 2041-1723. http://dx.doi.org/10.1038/ncomms1733. (Cited on page 84.)

[137] Putkunz, C.T. *et al. Atom-Scale Ptychographic Electron Diffractive Imaging of Boron Nitride Cones*. Physical Review Letters, **108**(7) (2012). ISSN 0031-9007, 1079-7114. http://dx.doi.org/10.1103/PhysRevLett.108.073901. (Cited on page 84.)

[138] Troeberg, L. and Nagase, H. *Proteases involved in cartilage matrix degradation in osteoarthritis.* Biochimica et Biophysica Acta (BBA) - Proteins and Proteomics, **1824**(1):133–145 (2012). ISSN 15709639. http://dx.doi.org/10.1016/j.bbapap.2011.06.020. (Cited on pages 86 and 99.)

[139] Nan, X. *et al. Vibrational imaging of lipid droplets in live fibroblast cells with coherent anti-Stokes Raman scattering microscopy.* The Journal of Lipid Research, **44**(11):2202–2208 (2003). ISSN 0022-2275. http://dx.doi.org/10.1194/jlr.D300022-JLR200. (Cited on page 91.)

[140] Jones, G.W. *et al. High-spectral-resolution coherent anti-Stokes Raman scattering with interferometrically detected broadband chirped pulses.* Optics Letters, **31**(10):1543 (2006). ISSN 0146-9592, 1539-4794. http://dx.doi.org/10.1364/OL.31.001543. (Cited on page 92.)

[141] Lesina, A.C. *et al. On the convergence and accuracy of the FDTD method for nanoplasmonics.* Optics Express, **23**(8):10481 (2015). ISSN 1094-4087. http://dx.doi.org/10.1364/OE.23.010481. (Cited on page 98.)

[142] Brownlee, M. *et al. Aminoguanidine prevents diabetes-induced arterial wall protein cross-linking.* Science, **232**(4758):1629–1632 (1986). ISSN 0036-8075, 1095-9203. http://dx.doi.org/10.1126/science.3487117. (Cited on page 99.)

[143] Zoumi, A. *et al. Imaging cells and extracellular matrix in vivo by using second-harmonic generation and two-photon excited fluorescence.* Proceedings of the National Academy of Sciences, **99**(17):11014–11019 (2002). ISSN 0027-8424, 1091-6490. http://dx.doi.org/10.1073/pnas.172368799. (Cited on page 99.)

[144] Nadiarnykh, O. *et al. Coherent and incoherent SHG in fibrillar cellulose matrices.* Optics Express, **15**(6):3348 (2007). ISSN 1094-4087. http://dx.doi.org/10.1364/OE.15.003348. (Cited on page 100.)

[145] Akins, M.L. *et al. Second harmonic generation imaging as a potential tool for staging pregnancy and predicting preterm birth.* Journal of Biomedical Optics, **15**(2):026020 (2010). ISSN 10833668. http://dx.doi.org/10.1117/1.3381184. (Cited on page 100.)

[146] Burke, K. *et al. Second harmonic generation reveals matrix alterations during breast tumor progression.* Journal of Biomedical Optics, **18**(3):031106 (2012). ISSN 1083-3668. http://dx.doi.org/10.1117/1.JBO.18.3.031106. (Cited on page 100.)

[147] Brown, C.P. *et al. Imaging and modeling collagen architecture from the nano to micro scale.* Biomedical Optics Express, **5**(1):233 (2014). ISSN 2156-7085, 2156-7085. http://dx.doi.org/10.1364/BOE.5.000233. (Cited on pages 100 and 107.)

[148] Williams, R.M. *et al. Interpreting Second-Harmonic Generation Images of Collagen I Fibrils.* Biophysical Journal, **88**(2):1377–1386 (2005). ISSN 00063495. http://dx.doi.org/10.1529/biophysj.104.047308. (Cited on page 100.)

[149] Chu, S.W. *et al. Thickness dependence of optical second harmonic generation in collagen fibrils.* Optics Express, **15**(19):12005 (2007). ISSN 1094-4087. http://dx.doi.org/10.1364/OE.15.012005. (Cited on page 100.)

[150] Vargas, G. *et al. Use of an agent to reduce scattering in skin.* Lasers in Surgery and Medicine, **24**(2):133–141 (1999). ISSN 0196-8092, 1096-9101. http://dx.doi.org/10.1002/(SICI)1096-9101(1999)24:2<133::AID-LSM9>3.0.CO;2-X. (Cited on page 100.)

[151] Xiang-Hui, W. *et al. Analysis of second-harmonic generation microscopy under refractive index mismatch.* Chinese Physics, **16**(11):3285–3289 (2007). ISSN 1009-1963, 1741-4199. http://dx.doi.org/10.1088/1009-1963/16/11/023. (Cited on page 100.)

[152] Zhang, G. *et al. Decorin regulates assembly of collagen fibrils and acquisition of biomechanical properties during tendon development.* Journal of Cellular Biochemistry, **98**(6):1436–1449 (2006). ISSN 0730-2312, 1097-4644. http://dx.doi.org/10.1002/jcb.20776. (Cited on pages 103 and 110.)

[153] Parry, D.A.D. and Craig, A.S. *Growth and development of collagen fibrils in connective tissue.* In A. Ruggeri and P.M. Motta, editors, *Ultrastructure of the Connective Tissue Matrix*, pages 34–64. Springer US, Boston, MA (1984). ISBN 978-1-4613-2831-5. http://dx.doi.org/10.1007/978-1-4613-2831-5_2. (Cited on page 104.)

[154] Novotny, L. and Hecht, B. *Principles of nano-optics.* Cambridge University Press, Cambridge, 2nd ed edition (2012). ISBN 978-1-107-00546-4. (Cited on page 113.)

[155] Mansfield, J.C. *et al.* *Collagen fiber arrangement in normal and diseased cartilage studied by polarization sensitive nonlinear microscopy.* Journal of Biomedical Optics, **13**(4):044020 (2008). ISSN 10833668. http://dx.doi.org/10.1117/1.2950318. (Cited on page 128.)

[156] Burruss, R.C. *et al.* *Unraveling the complexity of deep gas accumulations with three-dimensional multimodal CARS microscopy.* Geology, **40**(12):1063–1066 (2012). ISSN 0091-7613, 1943-2682. http://dx.doi.org/10.1130/G33321.1. (Cited on page 129.)